Plasmonic Nanoparticles for Optofluidic Applications

Thesis by

James R. Adleman

In Partial Fulfillment of the Requirements

for the Degree of

Doctor of Philosophy

California Institute of Technology

Pasadena, California

2009

(Submitted May 10, 2009)

Acknowledgements

First, I need to thank my advisor, Dr. Psaltis, whose insight, good humor, and confidence inspired me when I felt I had little of my own. I was very lucky to be in Dr. Psaltis' Lab, which in addition to being an exciting intellectual environment, was made up some of the best colleagues anyone could ask for. I am indebted to the advice and example of Dr. Martin Centurion, Dr. Hung-Te Hsieh, Dr. Zhenyu Li, who helped me with problems great and small. I was privileged to also work alongside Dr. David Erickson, who was a great role model as a researcher, Troy Rockwood and Baiyang Li, Dr. Ye Pu, and Jae-woo Choi. Dr. Mankei Tsang and Chia-Lung Hsieh were always available for challenging and interesting discussion. Dave McKeen was instrumental in helping me understand and simulate nanoparticle scattering. Thanks to Dr. Allen Pu, Dr. Iouri Solamatine and Dr. Shaw Wang for help with experiments and Dr. John Hong and Dr. Fai Mok for their instruction. Yayun Liu kept the labs running, and helped me dig up even the most obscure pieces of equipment. Lucinda Acosta was unbelievably supportive, and I thank her for her friendship and conversation as well as her administrative skills. I also want to acknowledge: Dr. Mattias Dietzel, Ted Dikaliaotis, Christos Santis, Shai Barak, Costis Sideris, Phil Munoz, Hua Long, and Michael Koesters.

During my time at Caltech, Dr. Psaltis' research group made the transition to the EPFL in Lausanne, Switzerland. I had a great time living in Switzerland, and am thankful for the hospitality of Dr. Psaltis and his family, Carole Berthet, Dr. Andreas Vasdekis, Dr. Rachel Grange, Hang Xu, Wuzho Song, Dr. Kostis Makris and Alexandre Goy. I am sure that le Laboratoire Optic is destined for great things.

Apart from our research group, I had the good fortune to be involved with the Center for Optofluidic Integration, which was a very fertile ground for new ideas. I want to thank Dr. Changhuei Yang, not only for the advice and help he gave to me in my work, but a also for his great efforts as Assistant Director of the center. It was a pleasure to interact with Changhuei and his students, especially Dr. Xin Heng, Xiquan Cui, and Lap Man Lee. Thanks also to Dr. George Whitesides, Dr. Byron

Gates, and Dr. Brian Meyers at Harvard for their work on plasmonic halfshells.

I also want to thank my collaborators outside of the center. First and foremost, Dr. Karsten Buse of the University of Bonn. Karsten and his group hosted me for my first trip to Europe, which I enjoyed immesurably. Special thanks go to my friend Dr. Helge Eggert, and to Felix Kuhnert and Judith Schweisig for all their work on our papers together. I also benefited from a great collaboration with Dr. David Goodwin and Dr. David Boyd at Caltech. In addition to being the driving force in our studies of nanoparticle arrays, Dave Boyd has taught me a lot about diverse subjects, from music to catalysis.

It isn't possible to acknowledge all the people whose support and friendship have enriched my stay at Caltech. Nonetheless I have to mention: Joyce Poon, John Choi, Melanie Yen, Raviv Perahia, Andrea Armani, Nadine Dabby, Jim Buckwalter, Florian Bohn, Ali Ghafari and the staff of the Watson Micro-Nano lab, Linda Dozsa and the EE department staff, the students of EE 134, members of Prufrock House, Barley Legal, the Ballistic Photons, and the Redheaded Stepkids. My roomates, Bob Pelayo, Mike Delormier, and Scott Miserendino. My good friends Chris Walker, Zuleikha Kurji, Johnny and Jennie Green, and Eric and Fernanda Ostby.

Finally, I want to thank my family: My parents whose love and support made all this possible. My big sister Nancy, who always listens. And Teresa, who is my joy.

Abstract

This thesis discusses the application of colloidal particles to optofluidic systems. Colloidal particles can be added as a "dopant" to the liquids in these devices to provide functionality that cannot be obtained with homogenous fluids. We examine electrooptic effects in liquid suspensions asymmetric metallic nanoparticles. The theoretical optical properties of gold nanorods and noble metal nanohalfshells are computed and compared with those of actual colloidal dispersions. We discuss the design and fabrication of electro-optic waveguides utilizing these suspensions as the active material. We also study the dynamics of photothermal holograms recorded by nanosecond laser pulses in suspensions of silver nanospheres. Unexpected transients in the grating diffraction efficiency correspond to the nanoscale inhomgeneity of the colloid. Longer timescale decay can be used to measure the thermal conductivity of the liquid as predicted by the established theory of heat conduction. This technique is extended to perform spatial imaging of the thermal diffusivity of immiscible binary liquids. Gold nanosphere coated substrates for microfluidic devices are employed to enable optical actuation of fluids. Nanoparticle absorption of continuous wave laser light was used to trap air bubbles inside partially filled microfluidic channels. Light focused on the array near one side of the trapped bubble will drive a mass flow across the bubble. This evaporative bubble assisted mass transport mechanism can be operated as a pump powered by a stationary laser beam. In addition, the process efficiently separates volatile and non-volatile materials and can concentrate and purify specimens in solution.

Finally, several schemes for storing and extracting data from subwavelength volumes using spectral multiplexing of semiconductor quantum dots are explored. We demonstrate microfluidic composition and delivery of cocktails of several colors of quantum dots to act as information packets for optical storage. In addition we analyze imaging at the subwavelength level using a patterned surface of quantum dots. The theoretical performance of such a surface is compared to imaging through nanoapertures as is currently implemented in optofluidic microscopy.

Contents

List of Figures

Chapter 1

Introduction

In this thesis, we will discuss the use of colloidal dispersions to provide novel functionality to so called optofluidic systems. Although the properties of fluids have been studied and used to perform imaging and other optical functions for centuries [1, 2], it is only in the last few decades that there has been a concerted effort to leverage the unique properties of liquid state to create truly integrated and functional optical devices.

Optofluidics refers broadly to using liquids to perform as optical systems, and conversely, using light to control liquid motion. The goal of such a design is to allow all optical systems that combine optical and fluidic function at the microscale and nanoscale in a complementary manner. Growth in this area has been driven by the impressive progress in the modeling and handling of fluid systems at the micron to nanometer scale which leverage the fabrication techniques originally developed for integrated circuits and micro-electromechanical systems. Microfluidic systems have been demonstrated in a variety materials, including silicon[3, 4], glass[5, 6, 7], parylene[8], and elastomers or so called soft lithographic materials [9, 10].

Several recent reviews of optofluidics emphasize the advantages of liquids as optical materials[11, 12]. For instance, the cohesive property of liquids causes them to form molecularly smooth interfaces with other imiscible fluids. These interfaces can be manipulated by changing their surface energy[13, 14]. Fluidity, that is the ability

to flow, allows liquids to exactly conform to their surroundings, and be simply and dynamically removed and replaced to repare damage or adapt to changes in the container volume. Fluidity allows tuning of optical circuits by replacement of a liquid optical component with a certain refractive index, n, with another material with a distinct index, simply by pumping the the new liquid into the region. Thus it is a intriguing approach to use liquids to designin adpative and reconfigurableoptical systems. Since the index contrast available between different types of liquids is on the order of 1, allowing liquid based devices to have a large degree of tunability compared to the small Δn available in conventional electro-optic, thermo-optic, and photo-refractive devices.

Another major advantage of a liquid medium is that its properties can be easily modified by mixing. Thus a pure liquid can be 'doped' with another liquid, or a finely divided solid material, to change its optical response. Miscible liquids can be combined to form fully homogenous media with optical properties that are an average of the constituent liquids. Soluable materials, such as dyes and salts can be dissolved to change the modify the linear refractive index and introduce gain or absorption at optical frequencies. Liquids can also be combined with materials that are not fully miscible to form suspensions of colloidal materials.

A colloidal dispersion is made up of distinct particles mixed into a homogenous fluids. The particles are small enough that they remain suspended in the liquid due the random thermal buffeting of Brownian motion, and are very slow to form a sediment and drop out of suspension[15]. The main distinction between a colloidal dispersion and a solution is that colloidal particles remain chemically and physically distinct on the scale of the particle, that is the material is heterogenous. We should note here that the terminology 'particle' does not necessarily imply that the suspended material must be solid. In fact, emulsions of oils in aqueous solutions can be considered colloidal suspensions, as can suspensions of small liquid droplets in air. However,

for most optofluidic purposes, the colloids utilized are solid particles, with sizes from around one nanometer to several microns.

Colloids are a powerful tool with wide application in optofluidic systems. They have several advantages over more traditional homogenous materials. The first is that they can be specifically engineered at the particle level to modify the optical properties of the liquid they are suspended in. For small particles, where scattering losses are not too high, a medium composed of high refractive index particles randomly dispersed in a liquid can be treated as an effective homgenous medium with index related to the volume concentration of colloidal particles. The effective medium theories of Maxwell-Garnett and Bruggman are used to predict the refractive index as a function of the volume concentration of particles[16]. By controlling the spatial concentration of particles, a spatial variation in refractive index can be created. This type of suspension has ben used to perform waveguiding in microfluidic liquid waveguides [17]. Microfluidic devices have also been used to create self organized two and three dimensional arrays of colloids that can serve as photonic band gaps and diffraction gratings [18].

Colloidal particles themselves can be manipulated by applied fields, either individually or in aggregate. At the optical frequencies, colloidal particles are subject to forces due to gradients in light intensity. The technique of optical tweezing is a form of dielectrophoretic force where a particle with refractive index higher than its surroundings is confined by a tightly focused beam. Trapped colloidal particles have been manipulated to create 3 dimensional structures, modify optical transmission[19], and act as rotors or paddles to drive fluid flow in microfluidic systems [20, 21]. In addition to the tweezing effect, colloids can be pushed by by radiation pressure, which is caused by momentum transfer from scattered photons to the particles. This technique has create and control the flow of particles through waveguides and along waveguides [22, 23], and also to seperate particles into groups based on size and diffusivity [24].

The changes in colloid density created by optical forces is a form of slow third order optical nonlinearity [25]. Large nonlinearity in such systems has been observed, as well as the demonstration of χ_3 processes such as phase conjugation [26], self focusing[27], and modulation instability [28].

Both absorption and gain can be introduced by carefully tailoring the material and structure of the colloidal particles. Of particular interest is the research into the properties of metallic nanoparticles. The conduction band electrons of silver and gold nanoparticles can be strongly polarized at optical frequencies, creating large resonances in the visible. These resonances can be tuned by changes in size or shape, or by incorperating other materials that modify the polarization of the particle. In the last two decades, major advances in the physical and chemical synthesis of nanoparticles have allowed a great deal of control over the shape, regularity, andcomposition of nanoparticles. Notably, groups such as those of Murphy, Halas, and Alivasatos have demonstrated directed growth of nanorods[29, 30], branching structures[31, 32], and core-shell particles with multiple resonances that can be placed throughout the visible and IR spectrum[33, 34, 35]. Due to large surface charge resonances excited in these particles, the local field around them can be enhanced by orders of magnitude. SERS, or Surface Enhanced Raman Scattering, relies on this effect to amplfy the unique Raman signature of chemicals for very sensitive detection and indentification. The strong interaction of metallic particles with the optical field also allows for energy delivery by optical absorption. The Lee group at UC Berkeley has demonstrated that liquids can be manipulated by heating of suspensions of mettalic shells on dielectric core particles. Focusing a laser beam near the leading edge of a liquid column cayses it to wet forward by a combination of liquid evaporation and condensation. The path of liquid through a microfluidic circuit can then be directed by scanning the laser beam[36].

This thesis describes a series of experiments regarding the optical properties of

nanoparticle suspensions and their use in optofludic systems. Chapter 2 we will discusses the both the optical properties of suspensions of metallic particles, and investigate potential as the active media in integrated electroptic devices. Chapter 3 describes a series of time resolved holographic experiments in colloidal suspensions that can be used to recover information about their micro and macroscale thermal properties. Chapter 4 details a method of microfluidic optical pumping we developed that is based on evaporation driven by photothermal energy absorbed by a two dimensional array of nanoparticles in a microchannel. This system is advantageous in that it utilizes a stationary laser beam to drive fluid motion, and can also be used seperate and collect components of a mixture, and perform distillation. In the fifth and last chapter we will outline several methods of information coding and storage based on photoluminescence.

References

[1] R. W. Wood. The mercury paraboloid as a reflecting telescope. *Astrophys. J.*, 29:827–829, 1909.

[2] Jeff Hect. *City Of Light: The Story of Fiber Optics*. Oxford University Press, Oxford, 1999.

[3] D.F. Moore and R.R.A. Syms. Recent developments in micromachined silicon. *Electronics & Communication Engineering Journal*, 11(6):261–270, DEC 1999.

[4] D.F. Weston, T. Smekal, D.B. Rhine, and J. Blackwell. Fabrication of microfluidic devices in silicon and plastic using plasma etching. *Journal OF Vacuum Science & Technology B*, 19(6):2846–2851, NOV-DEC 2001.

[5] I Rodriguez, P Spicar-Mihalic, CL Kuyper, GS Fiorini, and DT Chiu. Rapid prototyping of glass microchannels. *ANALYTICA CHIMICA ACTA*, 496(1-2):205–215, OCT 31 2003.

[6] KB Lee and LW Lin. Surface micromachined glass and polysilicon microchannels using mumps for biomems applications. *Sensors and Actuators A-Physical*, 111(1):44–50, MAR 1 2004.

[7] Ciprian Iliescu. Microfluidics in glass: Technologies and applications. *Informacije Midem-Journal of Microelectroncs Electronic Components and Materials*, 36(4):204–211, DEC 2006.

[8] Dominik Ziegler, Takafumi Suzuki, and Shoji Takeuchi. Fabrication of flexible neural probes with built-in microfluidic channels by thermal bonding of parylene. *Journal of Microelectromechanical Systems*, 15(6):1477–1482, DEC 2006.

[9] A. Folch, A Ayon, O Hurtado, MA Schmidt, and M Toner. Molding of deep polydimethylsiloxane microstructures for microfluidics and biological applications. *Journal of Biomechanical Engineering - Transactions of the ASME*, 121(1):28–34, FEB 1999.

[10] JC McDonald, DC Duffy, JR Anderson, DT Chiu, HK Wu, OJA Schueller, and GM Whitesides. Fabrication of microfluidic systems in poly(dimethylsiloxane). *Electrophoresis*, 21(1):27–40, JAN 2000.

[11] D. Psaltis, S. R. Quake, and C. H. Yang. Developing optofluidic technology through the fusion of microfluidics and optics. *Nature*, 442(7101):381–386, 2006.

[12] C. Monat, P. Domachuk, and B. J. Eggleton. Integrated optofluidics: A new river of light. *Nature Photonics*, 1(2):106–114, 2007.

[13] S. Kuiper and B. H. W. Hendriks. Variable-focus liquid lens for miniature cameras. *Appl. Phys. Lett.*, 85(7):1128–1130, 2004.

[14] F. Mugele and J. C. Baret. Electrowetting: From basics to applications. *J. Phys.: Condens. Matter*, 17(28):R705R774, 2005.

[15] W. B. Russel, D. A. Saville, and W. R. Schowalter. *Colloidal Dispersions*. Cambridge Univeristy Press, Cambridge, 1989.

[16] R. J. Gehr and R. W. Boyd. Optical properties of nanostructured optical materials. *Chemistry of Materials*, 8(8):1808–1819, 1996.

[17] R. S. Conroy, B. T. Mayers, D. V. Vezenov, D. B. Wolfe, M. G. Prentiss, and G. M. Whitesides. Optical waveguiding in suspensions of dielectric particles. *Appl. Optics*, 44(36):7853–7857, 2005.

[18] S.K. Lee, G.R. Yi, and S.M. Yang. High-speed fabrication of patterned colloidal photonic structures in centrifugal microfluidic chips. *Lab on a Chip*, 6(9):1171–1177, 2006.

[19] P. Domachuk, M. Cronin-Golomb, B. J. Eggleton, S. Mutzenich, G. Rosengarten, and A. Mitchell. Application of optical trapping to beam manipulation in optofluidics. *Optics Express*, 13(19):7265–7275, 2005.

[20] K. Ladavac and D. G. Grier. Microoptomechanical pumps assembled and driven by holographic optical vortex arrays. *Optics Express*, 12(6):1144–1149, 2004.

[21] J. E. Curtis and D. G. Grier. Modulated optical vortices. *Optics Letters*, 28(11):872–874, 2003.

[22] S. Mandal and D. Erickson. Optofluidic transport in liquid core waveguiding structures. *Appl. Phys. Lett.*, 90(18), 2007.

[23] B. S. Schmidt, A. H. J. Yang, D. Erickson, and M. Lipson. Optofluidic trapping and transport on solid core waveguides within a microfluidic device. *Optics Express*, 15(22):14322–14334, 2007.

[24] S. J. Hart, A. V. Terray, and J. Arnold. Particle separation and collection using an optical chromatographic filter. *Appl. Phys. Lett.*, 91, 2007.

[25] R. El-Ganainy, D. N. Chritodoulides, C. Rotschild, and M. Segev. Soliton dynamics and self-induced transparency in nonlinear nanosuspensions. *Optics Express*, 15(16), 2007.

[26] D. Rogovin and S.O. Sari. Phase conjugation in liquid suspensions of microspheres in the diffusive limit. *Phys. Rev. A*, 31:2379–2389, 1985.

[27] A. Ashkin, J.M. Dziedzic, and P.W. Smith. Continuous-wave self-focusing and self-trapping of light in artificial kerr media. *Opt. Lett.*, 7:276–278, 1982.

[28] P. J. Reece, E. M. Wright, and K. Dholakia. Experimental observation of modulation instability and optical spatial soliton arrays in soft condensed matter. *Phys. Rev. Letters*, 98, 2007.

[29] N. R. Jana, L. Gearheart, and C. J. Murphy. Seed-mediated growth approach for shape-controlled synthesis of spheroidal and rod-like gold nanoparticles using a surfactant template. *Adv. Materials*, 13(18):1389–1393, 2001.

[30] T. K. Sau and C. J. Murphy. Seeded high yield synthesis of short Au nanorods in aqueous solution. *Langmuir*, 20(15):6414–6420, 2004.

[31] A. G. Kanaras, C. Sonnichsen, H. T. Liu, and A. P. Alivisatos. Controlled synthesis of hyperbranched inorganic nanocrystals with rich three-dimensional structures. *Nano Lett.*, 5(11):2164–2167, 2005.

[32] D. J. Milliron, S. M. Hughes, Y. Cui, L. Manna, J. B. Li, L. W. Wang, and A. P. Alivisatos. Colloidal nanocrystal heterostructures with linear and branched topology. *Nature*, 430(6996):190–195, 2004.

[33] E. Prodan, C. Radloff, N. J. Halas, and P. Nordlander. A hybridization model for the plasmon response of complex nanostructures. *Science*, 302(5644):419–422, 2003.

[34] H. Wang, D. W. Brandl, F. Le, P. Nordlander, and N. J. Halas. Nanorice: A hybrid plasmonic nanostructure. *Nano Lett.*, 6(4):827–832, 2006.

[35] H. Wang, Y. P. Wu, B. Lassiter, C. L. Nehl, J. H. Hafner, P. Nordlander, and N. J. Halas. Symmetry breaking in individual plasmonic nanoparticles. *Proc. National Acad. Sciences United States Am.*, 103(29):10856–10860, 2006.

[36] G. L. Liu, J. Kim, Y. Lu, and L. P. Lee. Optofluidic control using photothermal nanoparticles. *Nature Materials*, 5:27–32, Jan 2006.

Chapter 2

Asymmetric Colloids for Optofluidic Waveguides

In this chapter we will describe the methods and tools needed to analyze the optical properties of suspensions of nanosized particles in a liquid medium. We will concentrate on the scattering from noble metal particles such as silver and gold, deferring the discussion of semiconductor particles to chapter 5. First we will outline the basic physics of optical properties in homogeneous materials. Then we will discuss scattering from a single particle and the optical properties of a suspension of particles in a homogeneous host material.

The second part of this chapter details our experimental efforts to create electric-optic fluidic waveguides using suspensions of either nanorods or composite silica and metal nanoparticles. These particles are promising materials for optofluidics, because they can be designed with their resonances tuned to the wavelengths of interest in the optical system. Since a polled suspension of asymmetric nanoparticles is both birefringent and dichroic, these materials have the potential to serve as both polarization rotation elements and absorptive filters or polarizers. We will describe progress toward the implementation of electrically contacted fluid waveguides that can be used to study the polling of asymmetric nanoparticle suspensions, and their integration integrate with broader optofluidic systems.

2.1 Physical Framework

At a fundamental level, the electromagnetic (EM) properties of a substance are determined by the charges it contains, and the orientation and geometry of the substance at scales both smaller and larger than the wavelength of the radiation. In the optical regime, we normally deal with free space wavelengths from around 300 nm to several microns. These scales are much larger than the average separation between molecules in a usual crystalline or amorphous material; For instance, the unit cell length of a crystal of gold is around 4 angstroms, and the length of the hydrogen bond between water molecules at 25 °C is around 2 angstroms [1]. In practice it is customary to treat the interaction of the electric field through condensed matter by averaging the contribution of individual molecules in a volume into a macroscopic electric permitivity, ϵ, and magnetic permeability, μ, which represent the response of the material to EM fields as a continuum.

The EM fields are described using the famous Maxwell's equations:

$$\nabla \times \vec{E} = -\mu \frac{\partial \vec{H}}{\partial t} \tag{2.1}$$

$$\nabla \times \vec{H} = \frac{\partial \epsilon \vec{E}}{\partial t} + \vec{J} \tag{2.2}$$

$$\nabla \cdot \epsilon \vec{E} = \rho \tag{2.3}$$

$$\nabla \cdot \vec{H} = 0 \tag{2.4}$$

The macroscopic properties of the medium (i.e. ϵ,μ) are determined from its susceptibility to polarization and magnetization (i.e. χ_e,χ_m) by the constitutive re-

lations:

$$\vec{D} = \epsilon_0 \vec{E} + \vec{P} = \epsilon_0 \vec{E} + \epsilon_0 \chi_e \vec{E} \tag{2.5}$$

$$\vec{B} = \mu_0 \vec{H} + \vec{M} = \mu_0 \vec{H} + \chi_m \vec{H} \tag{2.6}$$

Here $\vec{P}$ and $\vec{M}$ are the polarization and magnetization vectors which are due to the motion of charge within the medium driven by the electric and magnetic fields. In the work presented in this thesis, the effects of magnetization are negligible, and unless otherwise noted, we assume that $\mu = \mu_0$. Thus $\chi_m = 0$; the symbol χ will be used to unambiguously represent the electric susceptibility. Since the electric and magnetic fields are vectors, which can be polarized in any three-space direction, the quantities χ and ϵ are in general tensors of the second rank. Also, these quantities vary with frequency are generally complex, which reflects that the material responds out of phase to a time varying driving field.

Waves in infinite homogeneous media can be described by the Helmholtz wave equation

$$\nabla^2 \vec{E} = -\mu\epsilon\omega^2 \vec{E} \tag{2.7}$$

which is derived from Maxwell's equations for a time harmonic field with angular frequency ω. The plane wave solution to the wave equation can be written

$$\vec{E} = E_0 e^{i\vec{k}\cdot\vec{r} - i\omega t} \tag{2.8}$$

This is a solution to equation 2.7 when the wave vector $\vec{k}$ has a magnitude $|k| = \sqrt{\mu\epsilon}\omega$. The magnitude of $|k|$ can also be written in terms of the refractive index and the vacuum wavelength $|k| = \frac{2\pi n}{\lambda_0}$. Common dielectric materials often have refractive indices with a positive real component, but there has been strong interest recently

in materials with a negative refractive index, which exhibit the interesting property that the phase of the wave moves opposite to the direction of energy flow. [2, 3]

2.1.1 Free Plasma

The permit from the equation of motion of a particle in a harmonic field [4]. In the case of a plasma of N electrons per unit volume with charge $-q$ and mass m_e the susceptibility is negative,

$$\chi = -\frac{Nq^2}{\epsilon_0 m_e \omega^2}. \tag{2.9}$$

$$\epsilon = \epsilon_0(1 - \frac{\omega_p^2}{\omega^2}) \tag{2.10}$$

where ω_p is the plasma frequency, defined as $\omega_p \equiv \sqrt{\frac{Nq^2}{\epsilon_0 m_e}}$.

2.1.1.1 Conduction Electrons

The conduction band electrons in many metals behave in a similar manner to a free plasma. These electrons, which are de-localized throughout the atomic lattice rather than bound to a single atom can be considered an ideal gas of electrons with an effective mass m_e. This model of conduction electrons is known as the Drude model [1]. The addition of a damping term in the denominator of equation 2.10 accounts for the scattering of the electrons from the atomic cores of the metal.

$$\epsilon = \epsilon_0 \left(1 - \frac{\omega_p^2}{\omega^2 + i\gamma\omega}\right) \tag{2.11}$$

The damping coefficient γ is related determined by the mean free path of the metal, and its Fermi velocity, and is taken to be v_f/λ_{fp}.

2.1.2 Bound Charges

In materials that have few conduction band electrons, such as insulators and semiconductors away from their band edges, the permitivitty is dominated by bound charges. Additionally, the electrons in the valence bands of metals contribute non-negligibly to the permittivity, so that the Drude model is not an accurate approximation for many metals [1]. The Lorenz model is used to determine the optical properties of a bound oscillator. In this case, the electron feels a Coulombic attraction to the core that acts as a restoring force with a spring constant K. This results in a natural resonance frequency $\omega_0 = \sqrt{K/m_e}$.

$$\epsilon = \epsilon_0 \left(1 + \frac{\omega_p}{\omega_0^2 - \omega^2 - i\gamma\omega}\right) \tag{2.12}$$

2.1.3 Claussius-Mossoti Relation

The relationship between the macroscopic permit given by the Claussius-Mossoti relation. It can be derived by considering a regular cubic lattice of identical molecules with molecular polarizability α, and a concentration of N (note: the symbol α will be used to denote microscopic polarizabilities, whether they are of individual molecules, nanoclusters, or discrete subunits of a larger polarizable volume). The relation can be written to determine the susceptibility of a medium if the microscopic polarizability is known:

$$\chi = \frac{N\alpha}{1 - N\alpha/3}. \tag{2.13}$$

Conversely, if the permittivity is measured and the concentration of molecules is known, we can determine the microscopic polarizability

$$\alpha = \frac{3}{N}\frac{\epsilon - \epsilon_0}{\epsilon + 2\epsilon_0}. \tag{2.14}$$

The equations 2.14 and 2.13 are rigorously derived by Jackson [], and are strictly valid only when the fields from neighboring molecules are cancelled due to symmetry of the material. However, he notes that for most materials the internal fields are negligible, and the relation is a good approximation. The ratio of dielectric constants in equation 2.14 is referred to as the Claussius-Mossoti factor, and it often appears in the mathematical expressions that govern the physics of electromagnetism in small particles.

2.2 Scattering from Nanoparticles

The scattering of light from particles has been extensively studied for more than a century. When an incident plane wave interacts with a scatterer, energy can be scattered from the incident wave, or absorbed by the scatterer. The strength of these interactions is measured by the scattering and absorption cross sections, c_{sca} and c_{abs}, with units of area. The extinction cross section, c_{ext} is equal to the sum of the scattering and absorption cross sections. The product of the incident intensity with the extinction cross section gives the power removed (extincted) from the incident wave in the far field by both scattering and absorption.

The exact vectorial solution to the scattering of an incident plane wave from a spherical volume was developed by Mie in his 1908 paper [5, 6]. Due to the spherical geometry, the waves both inside and outside the sphere are expressed in infinite series of spherical harmonics, and the problem is solved by ensuring that for each term of the series the incident, scattered and internal fields and their derivatives match at the boundary of the scattering sphere.

Bohren and Huffman have published FORTRAN codes, entitled BHMIE and BHCOAT, to compute the cross sections for homogeneous and multilayered spherical particles, and for spherical particles composed of a core and a shell with different

permit implemented these codes in Matlab for ease of use (see appendix A). These routines can be used to to simulate spheres with a wide range of permit wavelengths.

However, in the case of spheres small compared to the wavelength of light its not necessary to apply the full Mie solution. The scattering cross sections can be solved for in the quasi-static approximation. Since the phase of the electric field is approximately constant across the sphere, we can calculate the polarizability of the sphere in a uniform field.

$$\alpha = 4\pi a^3 \frac{\epsilon_1 - \epsilon_m}{2\epsilon_m + \epsilon_1} \tag{2.15}$$

The extinction due to a vanishingly small sphere can be calculated by treating it as a ideal dipole with an equivalent polarizability. The cross sections of a dipole can be determined from the optical theorem [7]. Derivation of the absorption and extinction cross section section gives:

$$c_{abs} = kIm(\alpha) \tag{2.16}$$

$$c_{sca} = \frac{k^4}{6\pi}|\alpha|^2 \tag{2.17}$$

2.2.1 Plasmonic Resonance

The strong resonances of the noble metal nanoparticles are a consequence of large coherent oscillations of their conduction band electrons. Intuitively, we can think of the conduction band electrons of a metal nanosphere as a rigid sphere of negative charge that is driven by the electric field, and feels a restoring force due to Coulombic attraction of the sphere of positive ions of the metal lattice. Because the displacement of the two spheres of charge is small, the polarization creates a surface charge density where the two spheres no longer exactly overlap. The magnitude of polarization due to the electric field becomes very large when the frequency of the incident radiation

matches the resonance frequency of this charge oscillation. As is apparent from the equation 2.15, resonance occurs when the permittivity of the material that makes up the sphere has a real value of $-2\epsilon_m$, so that the the denominator of the expression is small and imaginary. Solving equation 2.11 for this value, we obtain the theoretical resonance frequency of a small spherical nanoparticle:

$$\omega = \frac{\omega_p \sqrt{\epsilon_0}}{\sqrt{3\epsilon_m}} \tag{2.18}$$

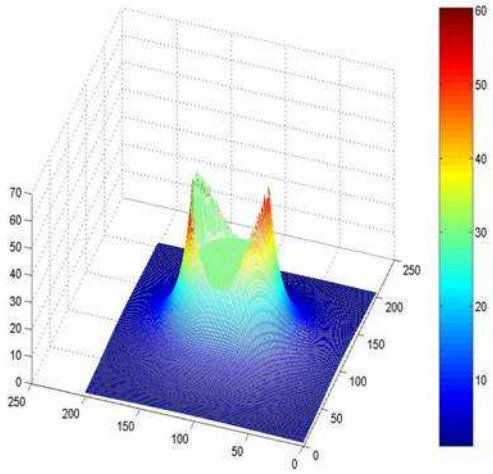

Figure 2.1: A plot of the magnitude of the electric field inside and outside a silver nanosphere of diameter 50 nm in an incident field with $\lambda_0 = 390nm$.

Thus the frequency resonant peak of a nanosphere should vary with the medium it is surrounded by. Figure 2.2 illustrates the change in extinction of a solution of 50 nm diameter gold nanoparticles suspended in mixtures with increasing refractive index. The solid lines are the computed theoretical extinction for $n = 1.33, 1.40, 1.45$. The discrete data points are the measured extinction for suspensions of gold nanoparticles (Ted Pella co.) suspended in water (n=1.33) and in a mixture of 85% glycerol in deionized water by weight, which has a refractive index $n \approx 1.45$. Extinction was measured with a UV-VIS spectrophotometer. Samples were contained in disposable

plastic cuvettes (VWR Inc.) with a path length of 10 mm. The extinction of each suspension was measured relative to a blank sample filled with a water-glycerol mixture identical to the suspending medium of the sample.

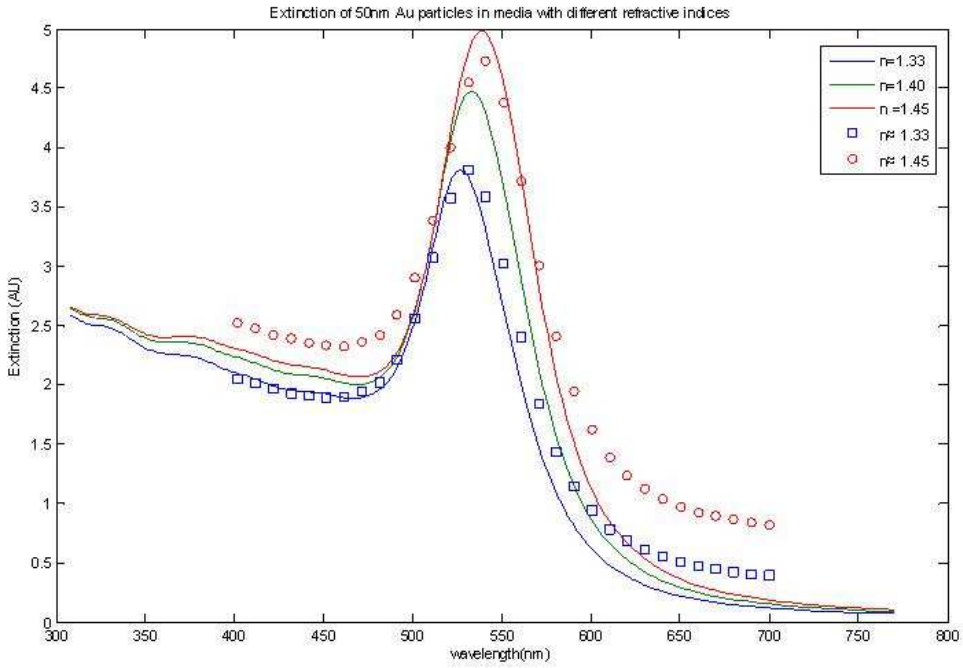

Figure 2.2: Variation of Plasmon Scattering with refractive index of liquid medium

2.2.1.1 Size Effects

For vanishingly small nanoparticles, the absorption and scattering correspond to the dipole polarizability. This is equivalent to keeping only the first order term of the Mie series solution. However, as particles become larger compared to the wavelength of light, we must consider higher order terms, corresponding to the electrical and magnetic multipoles. Classically, the resonance wavelength shifts to lower frequencies for larger particles, since the Coulombic coupling of the regions of positive and negative surface charge is relaxed as the diameter of the particle increases. The shift in the maximum extinction frequency is a rather weak function of size for noble metal particles between 10-100 nm, as is shown by figure 2.3. However, a consequence of the

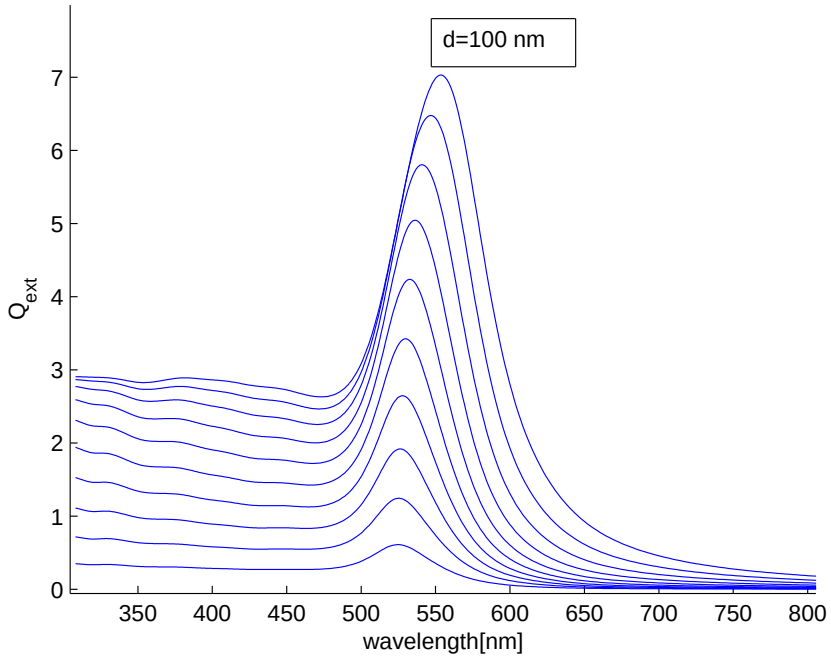

Figure 2.3: The classical redshift of the plasma resonance of gold NPs with increasing size. The curves show extinction of Au particles of sizes 10 nm to 100nm in 10 nm increments

different size dependence of the scattering and absorption efficiency (i.e. equations 2.17,2.16) is that the extinction of very small particles is dominated by absorption.

In the realm of very small particles, there are several deviations from classical behavior. The first of these is a redshift in the resonant wavelength with decreasing size, due to the the spill out of the electron cloud as compared to the ionic radius. This phenomenon has been observed experimentally and is analyzed by C.P. Collier his Ph.D. thesis [8].

The second deviation from classical behavior is incoherent scattering of electrons that collide with the surface of the particle. Boundary scattering has been invoked by many researchers to explain the homogeneous broadening of nanoparticle suspensions with small sizes. This scattering is accounted for by modifying the damping parameter

γ in the Drude model so that

$$\gamma = v_f \left[\frac{1}{\lambda_{fp}} + A\frac{1}{r} \right] \tag{2.19}$$

Here A is fit parameter that takes into account the properties of the surrounding material, as well as any passivating layer on the nanoparticle that may impact surface scattering. $A = 4/3$ is a common starting point for the value of this parameter, corresponding to observations of silver nanospheres in an aqueous suspension [9]. Recent experiments measuring the absorption of single nanoparticles using microscopic techniques have yielded conflicting results on whether or not the surface scattering process impacts the the measured line width [10]. These single nanoparticle experiments indicate that the broadening of the line width measured in suspensions containing metal nanoparticles is due to inhomogeneous broadening. If this is the case, the resonances of each particle are relatively narrow (i.e. the A parameter in equation 2.19 is 0), but variations of size and shape between the particles in suspension cause their resonances to peak at different energies, creating a broader observed peak for the whole suspension.

2.2.2 Shape Effects

While the peak extinction frequency is not strongly dependent on size for all but the smallest nanoparticles, it is *heavily* impacted by variation in particle shape. Many striking experiments have been performed that measure the frequency variation of metallic nanoparticles based on changes in shape [11, 12, 13, 14]. We can understand these effects qualitatively in much the same way as the weak size dependence. Changing the shape of the particle modifies the coupling strength between the electron cloud and the ionic core of the particle, altering the plasmon resonance energies of the particle. For non-spherical particles, multiple resonances will appear under un-

polarized light, due to the difference in the size of allowed surface modes in different directions.

Ellipsoidal particles are the simplest example of this type of polarization dependent scatterer. A nanoellipsoid with 3 distinct axes $a1, a2, a3$ has a polarizability along the ith axis ($i = 1, 2, 3$) given by

$$\alpha_i = 4\pi a_1 a_2 a_3 \frac{\epsilon_1 - \epsilon_m}{3\epsilon_m + 3L_i(\epsilon_1 - \epsilon_m)} \tag{2.20}$$

where L is the shape factor, determined by the eccentricity and symmetry of the ellipsoid [15]. In the case of a sphere, the shape factor L_i is 1/3 for all axes, and the expression is equivalent to equation 2.15. Distinct resonances for each axis will be apparent in the extinction spectra. For gold and silver nanoellipsoids, increasing the eccentricity causes red shifting of the largest peaks. The optical properties of ellipsoidal particles are qualitatively very similar to those of the nanorods we will consider below.

2.2.3 Core Shell Structures

Multiple resonance energies can also be observed from spherical particles, by changing their internal composition. a spherical dielectric core surrounded by a concentric sphere of metal, are often synthesized to provide a tunable plasmonic resonance. These so called nanoshells exhibit two distinct plasmon resonances. The resonances can be calculated using a generalization of the Mie expansion, due to the spherical symmetry of the particle [15]. Figure 2.4 shows the scattering associated with a gold nanoshell, made up of a silica core of radius 50 nm, and a gold shell 5 nm thick. The higher energy resonance is corresponds to an antisymmetric surface polarization of both the inner and outer surfaces of the metallic shell. The lower energy resonance corresponds to symmetric surface polarization of the outer and inner surfaces[16].

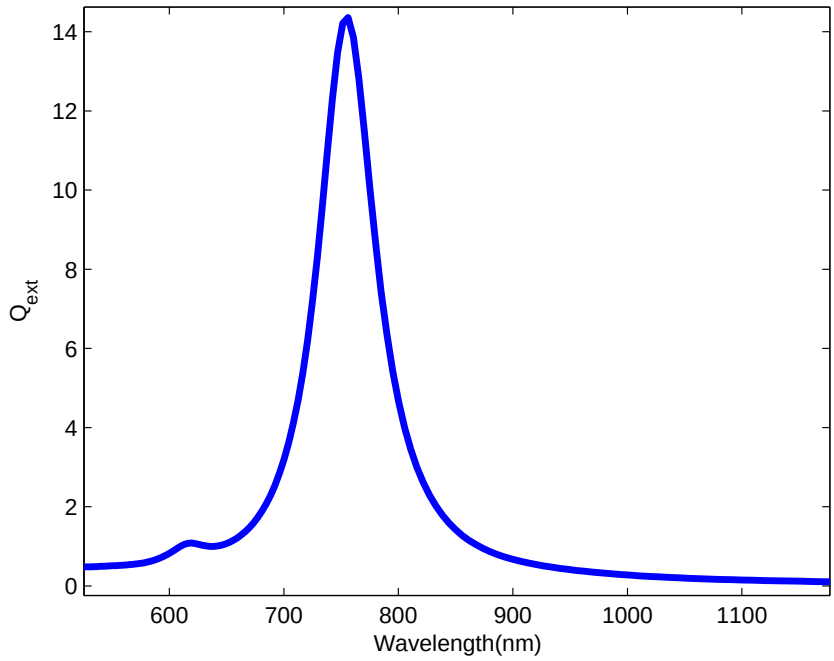

Figure 2.4: The extinction efficiency of a silica-gold core-shell (inner diameter 100nm, 5 nm Au), as calculated by Mie theory.

The strength of the Coulombic coupling is controlled by the ratio of inner to outer diameters. Shells that are thin in comparison to the core radius will have strongly red shifted symmetric resonances. Well controlled chemical growth of gold shells on silica nanospheres allows for much finer tuning of resonance position over a much broader range than is possible with rodlike particles [17]. However, the overall spherical symmetry of these particles means that the two optical resonances display no polarization dependence, in contrast to nanorods or ellipsoids.

2.2.4 Scattering From Arbitrarily Shaped Particles

Closed form solutions for the electromagnetic fields inside and outside of nanoparticles only exist for shapes that are highly symmetric (e.g. spheres, ellipsoids, cylinders). In general there are no straightforward analytical techniques to solve for the extinction spectrum for a small particle of arbitrary shape. However, many computational

approaches have been developed to solve for scattering from a single particle with arbitrary shape and composition. As with any numerical simulation care has to be taken that the limitations and assumptions implicit in the chosen simulation method are a good fit for the geometric and material parameters of the particle to be simulated. One family of techniques based on numerically matching analytical expressions for electric fields expanded as multipoles at the boundaries between regions. Of these point matching techniques, the generalized multipole technique (also known as the multiple multipole method) has been recently exploited to calculate the electric field of many subwavelength metal structures [18]. Also popular among computational techniques are finite difference approaches, which divide the space into small volume elements and solve the differential form of Maxwell's equations starting from fields defined at a boundary [19, 20].

A conceptually simple method to simulate scattering from a particle is to determine its polarizability by summing the contribution of the microscopic dipoles that make up the volume of the particle. This is the basic approach used in the Discrete Dipole Approximation, developed by Draine and Flaatau [21]. The scattering volume is discretized onto a regular lattice of N points. The simulation solves for the polarizability the assembly of dipoles by formulating a matrix equation for the microscopic polarization of each lattice point in an applied incident field. A single dipole with microscopic polarizability α_j is acted upon by the superposition of the incident electric field and the dipole fields of all other dipoles, so that the dipole polarization is given by the expression:

$$p_j = \alpha_j \vec{E}_{j,inc} - \alpha_j \sum \tilde{A}_{jk} p_k \tag{2.21}$$

where $\tilde{A}_{jk}$ is a matrix that gives the strength of the dipole field at position $\vec{r}_j$ from a dipole with polarization p_k at position k. This matrix is constructed so that the diagonal is zero, thus the lattice point j is not influenced by its own dipole field. Rearranging the equation to place the polarizability terms on one side gives a linear

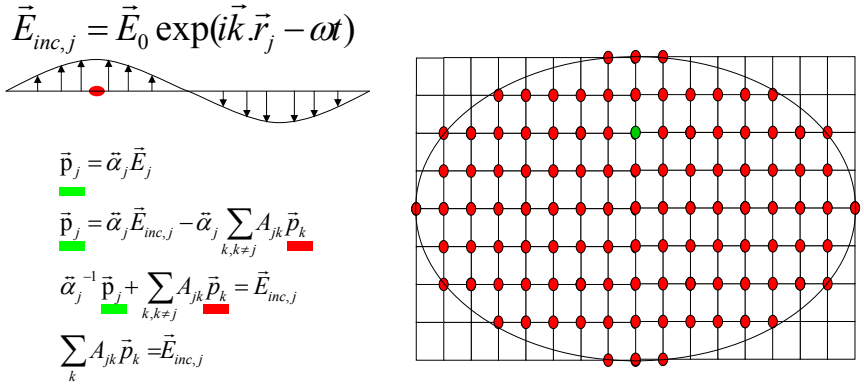

Figure 2.5: The discrete dipole method applied to an arbitrary particle

relationship equating the polarization of the dipoles with to the incident field.

$$\sum A_{jk} p_j = \vec{E}_{j,inc} \tag{2.22}$$

The matrix A_{jk} is the sum of of $\tilde{A}_{jk}$ and the inverse of the microscopic polarizability, α_j^{-1}.

We use DDSCAT 6.0, an implementation of the DDA coded in Fortran by Draine and Flaatau to model the scattering from single particles that lack spherical symmetry [22]. The software allows for the discretization of user defined geometries and computes the microscopic polarizability of the lattice points from the specified dielectric constants of materials. The linear equation 2.22 is solved using the iterative complex conjugate grating method. The accuracy of the simulation is controlled by the size of the scattering volume. Ideally, the phase of the incident wave should be constant across the scattering volume, that us $\lambda_0/n_1 > a$, where a is the dimension of the scatterer. The simulation of metallic nanoparticles is complicated by the fact that the refractive index may change rapidly across the frequencies of interest. In practice, the simulated scattering converges as the number of discrete dipoles is increased.

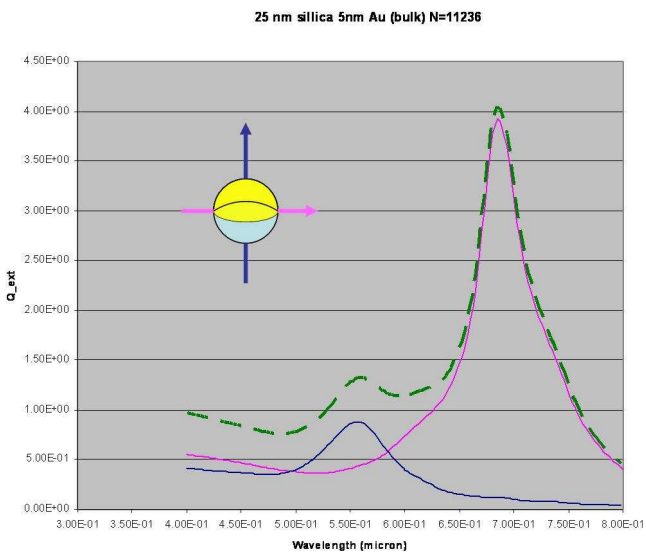

Figure 2.6: Computed scattering from a gold halfshell with a core radius of 25 nm and a shell thickness of 5 nm

2.2.5 Half Shell Structures

We would like to be able to engineer structures that possess the advantages of a metallic core shell structure, but to imbue them with a polarization dependence. One way to do this is to coat only one hemisphere of a silica nanosphere with metal. Partially coated particles (known as nano-halfshells, janus particles, or nanocrescents) have been created by first laying down a single layer of silica naospheres on a glass or silicon substrate, and then depositing a thin metallic layer from above by evaporation [23, 24, 25]. We calculate the optical properties of such a using the Discrete Dipole method as outlined above. Figure 2.6 shows the scattering from a gold halfshell particle as calculated by DDscat. This structure shows two resonance peaks, similar to those of the full core shell structure in Figure 2.4. However, when illuminated by light polarized along the particle symmetry axis (vertical orientation), only the low energy resonant mode is excited. Conversely, light polarized perpendicularly to the particle axis excites the only high energy mode.

2.3 Suspensions of Colloids

The optical response of a collection of nanoparticles can be assigned an effective dielectric constant as if it were a homogeneous material. The dielectric constant is an average of the dielectric constants of the particle material and the host material they are contained in. There are multiple theories that can be used to calculate the effective medium dielectric constant. The Maxwell-Garnett and Bruggman effective medium theories are two of the more popular choices. The Maxwell-Garnett theory is the natural choice for nanoparticle suspensions, as it was developed to treat this case, and considers particle inclusions with permittivity ϵ_1 within a homogeneous medium with permittivity ϵ_m[15].

$$\epsilon_{eff} = \frac{(1-f)\epsilon_m + f\beta\epsilon_1}{1-f+f\beta} \tag{2.23}$$

Here β is an average electric field across all the particle inclusions. For spherical inclusions, β is given by $3\epsilon_m/(2\epsilon_m + \epsilon_1)$. Because of the symmetry of the inclusions β will be the same for an electric field applied in any direction, thus the medium is isotropic. We can represent this as a diagonal tensor, where each of the diagonal elements is given by ϵ_{eff}.

for a medium composed of asymmetric particles, we can still apply the Maxwell-Garnett theory by using ellipsoidal inclusions. For any single ellipsoid, the degree of polarization depends on the alignment of the particles axis to the polarizing field. This means that for a medium of ellipsoids, β is given by an expression that once again incorporates the shape factor L_j. allowing for the average electric field of the ellipse to be different in each of the three polarization directions. In the case of randomly ellipses, averaging over all particles gives an equivalent β for all three polarizations, so the end result is a again an effective medium that homogeneous, a diagonal tensor with each of the three elements equal. However, if we can orient all the particles in

the same direction, we can write the effective medium tensor as a diagonal tensor with its unequal elements ϵ_i, ϵ_j, ϵ_k, representing an anisotropic medium [26]. Here the directions i,j,k correspond to the three axes of the ellipsoids.

The birefringence of an fully oriented medium is the difference between the refractive indicies of the two polarizations orthogonal to the direction of propagation:

$$\Delta n_\infty = \frac{N(\alpha_1 - \alpha_2)}{2\epsilon_0 n}. \tag{2.24}$$

N represents the number of inclusions per unit volume, and n refractive index of the unperturbed system [27]. The quantities α_1 and α_2 are the microscopic polarizabilities of the ellipsoid along the two polarizations of interest. However, equation 2.24 only describes a fully polled medium, in which every inclusion points in exactly the same direction. In the case of colloidal particles in a liquid, thermal buffeting (i.e. Brownian motion) will prevent prefect alignment. O'konski et al. developed an expression for the degree of alignment of polled particles, $F(U/kT)$, such that $\Delta n = \Delta n_\infty F(U/kT)$ [28, 27]. For low applied electric field the degree of orientation increases linearly:

$$F(U/kT) = \frac{\alpha E^2}{15kT}. \tag{2.25}$$

For high applied fields the degree of orientation asymptotically approaches one,

$$F(U/kT) = 1 - \frac{3kT}{\alpha E^2}. \tag{2.26}$$

.

For small colloidal particles, this analysis is approximately valid no matter the actual shape of the particle. As long as one can compute the polarizabilities α_j, the Maxwell-Garnett approach can be used to provide an effective medium.

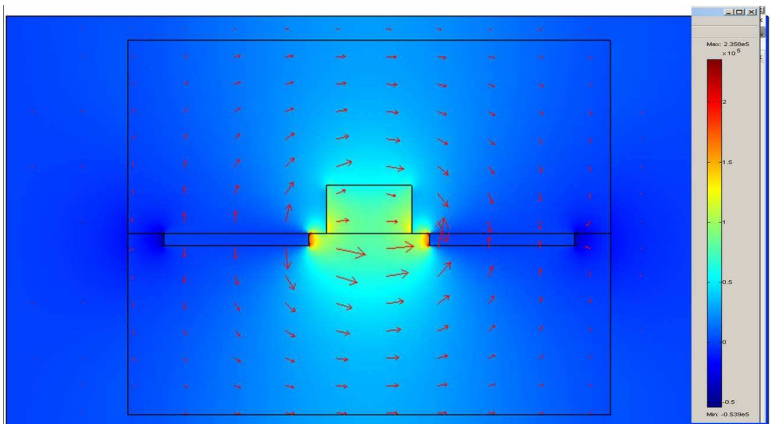

Figure 2.7: E-field magnitude across a 15 x 10 micron microchannel with 20 micron electrode spacing. D-field lines represented by arrows.

2.4 Electro-optic Waveguide

Now we turn to the application of suspensions of gold nano-halfshells and nanorods as electro-optic materials for liquid core waveguides. Our goal is to exploit the strong plasmonic resonances of metal particles to create colloidal suspensions that will strongly modify the transmission of polarized light. Like conventional electro-optic materials, a uniform electric field of a high magnitude (> 1 MV/m) needs to be applied across the liquid suspension to orient the particles. We can create this type of electric field distribution by integrating electrodes in close proximity to the microchannel containing the liquid suspension. Figure 2.7 shows a finite element simulation of the electric field across a microchannel created by a 1 volt potential applied across electrodes spaced by 20 microns.

The field across the rectangular channel is fairly uniform with a average magnitude of 0.1 MV/m. The voltage necessary to create a high degree of alignment was calculated determining the change in energy between a particle aligned with the electric field, and a particle aligned perpendicular to the field. This calculation was carried out by finite element analysis using the FEMLAB/COMSOL software package. The alignment energy ΔU for a single halfshell particle composed of a 50 nm

silica core and 5 nm gold shell is $6.22 \times 10^{-22} J/V^2$. Since the energy of the Brownian motion $kT = 4.11 \times 10^{-21}$, application of 10 Volts to the electrodes creates an alignment energy U that is greater than 10 times the thermal energy, which results in an alignment figure $F(U/Kt) > 0.7$ as determined by equation 2.26.

Our initial experiments were performed with suspensions of gold halfshells as the electro-optic medium. Halfshells with a 50nm core and 5 nm gold shell were supplied by Dr. Byron Gates and Dr. Brian Meyers of Dr. George Whitesides group at Harvard University, and suspended in a mixture of water and glycerol. However, the half shell particles did not demonstrate a high enough degree of uniformity to observe clear plasmonic resonances in the sample. Figure 2.9 shows an absorbance measurement taken using unpolarized light. There is a minimum in the absorption at the 500 nm wavelength, but no sign of the clear peaks at 550 nm and 700 nm predicted by the scattering simulation (Figure 2.6). We examined the nanoparticles with by SEM. The micrographs confirm that inhomogeneous broadening masks the plasmonic resonances. Figure 2.8 is characteristic of the SEM observations; the gold caps on the silica nanoparticles (bright regions) show ragged edges and variations in shape and thickness. This irregularity washes out any single plasmon resonances.

Clearly, a more uniform sample of nanoparticles is necessary to create electro-optic waveguides for optofluidics. While research is continuing into creation of uniform gold halfshells, we decided to switch our focus to gold nanorods. We synthesized gold nanorods using the chemical procedure developed by Sau et. al [29]. We chose this technique because of its high yield and ability to controllably create nanoparticles with aspect ratios of as small as 2:1. We created the nanorods with average dimensions of 40 nm by 15 nm (aspect ration of 2.667) which display resonant peaks at 540 nm nm and 750 nm. These parameters were chosen because the resonances can be easily accessed, using either a diode pumped solid state laser (emission wavelength 532 nm) or a near infrared laser diode (emission wavelength 785 nm). Unlike the halfshell

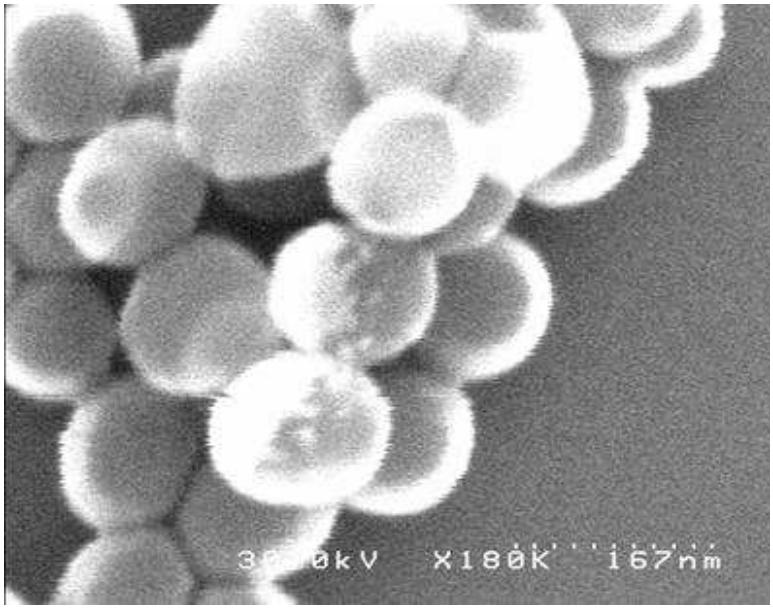

Figure 2.8: SEM micrograph of fabricated nano halfshells. Bright regions are the metal caps.

suspensions, suspensions of the gold nanorods show a high degree of uniformity, and clear plasmonic resonances in their absorbance spectrum (see Figure 2.10).

Because of the very large optical polarizabilities of single nanorods as compared to molecules such as liquid crystals, we might expect plasmonic suspensions to have superior performance to liquid crystal technology. However, inspecting equation 2.24, we see that the strength of the birefringence of a particle suspension is based on the concentration of particles. Since we are limited to relatively low concentrations to maintain the colloidal dispersion and prevent particle aggregation, a relatively long path length is needed. In order to guide light through the microchannel, the refractive index of the The experimental design is a waveguide with a liquid core of water and glycerol with refractive index greater than PDMS. Planar electrodes are incorporated along the sides of the channel to polarize the waveguiding medium. The basic design is shown in figure 2.11. The device is constructed from two thick PDMS layers (figs. 2.12 and 2.13) constructed by replica molding soft lithography. These layers are cast from complimentary molds created on silicon by photolithography. The fabrication

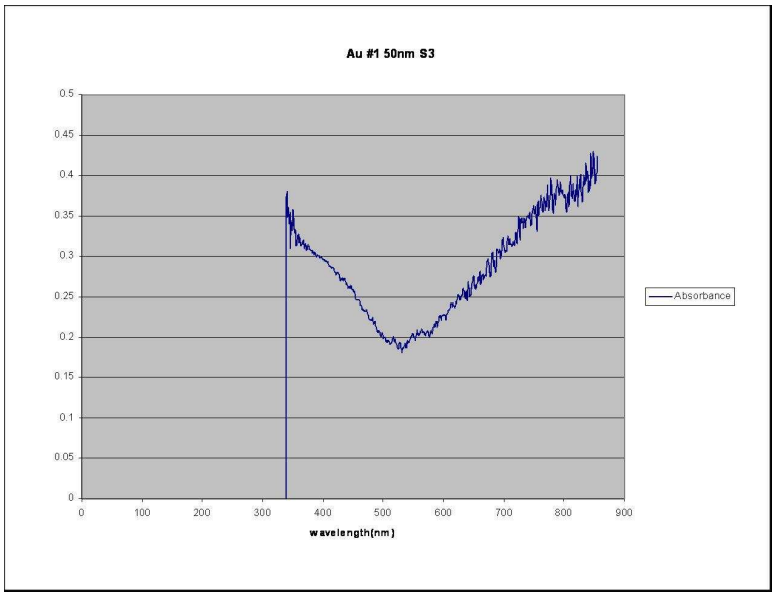

Figure 2.9: Absorption spectrum of gold halfshell suspension. Plasmonic resonances are obscured by inhomogeneous broadening.

of the device begins with the creation of the bottom layer mold. The bottom layer mold contains the features that produce the microchannel that acts as the liquid wave guide core.

The electrodes that are used to apply fields to the waveguide are fabricated in gold on the same substrate. Gold alignment marks are defined to enable registration of the photoresist features with the electrodes. The advantage defining the electrodes and the channel mold on the same substrate is that a channel and aligned electrodes can be created in a single casting step. The electrodes are embedded in the PDMS by utilizing an adhesion promoter between the gold and PDMS so that the electrodes are lifted off when the PDMS chip is removed from the mold surface[30].

The substrate wafer (76 mm 100 orientation test grade Si, Silicon Quest inc.) is first cleaned using a piranha etch (4:1 H_2SO_4:H_2O_2 15 min at 120 °C) in order to remove any impurities that might cause deposited gold to adhere to the wafer. A subsequent oxygen plasma treatment (15 minutes at 100 W and 250 mT) ashes any contamination that survives the piranha etch. 50 nm of gold is deposited on

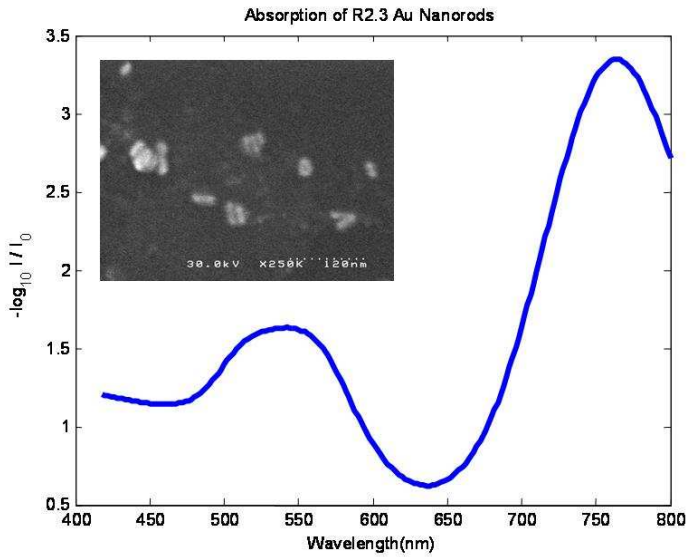

Figure 2.10: Absorption spectrum of a sample of gold nanorods with mean aspect ration 2.667. Inset micrograph of gold nanorods deposited on a Si substrate

the substrate via thermal evaporation, with no chrome or titanium adhesion layer. The gold coated wafer must be handled very carefully to avoid rubbing or scratching away the metal. We coat the wafer with a thin positive photoresist and define the electrodes and alignment marks by photolithography. The resist is developed, and the exposed gold etched away chemically (TFA gold etch). The resist is stripped away using a warm acetone bath followed by a rinse in fresh acetone. The gold layer will not survive immersion in strong acids such as nanostrip or piranha etch, so the remaining photoresist residue is ashed away with an oxygen plasma.

We use SU-8 2000 series negative photoresist to define the molds used to cast the waveguide structure. We use a two layer process to create both the liquid core waveguide, and the much larger fiber access port which can be used to end couple single mode optical fibers to the on chip waveguide. The SU-8 epoxy is a good material for this purpose because when properly exposed and developed, it becomes fully cross linked and can survive multiple processing steps. This allows the creation of multilevel structures defined layer by layer [30]. However, SU-8 is known for its

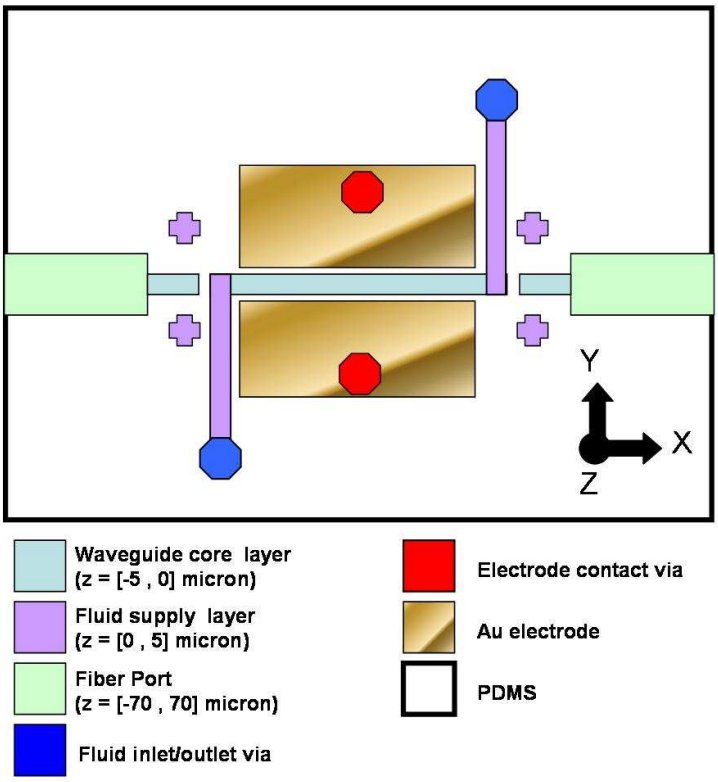

Figure 2.11: A schematic diagram of the pollable waveguide device

poor adhesion to many substrates [31], and must be processed carefully to ensure the channel molds do not warp or lift away from the wafer during development.

The freshly ashed wafer is baked on a hotplate at 180 °C for over an hour to drive off any adsorbed water that might interfere with adhesion of the resist. To minimize stress due to thermal expansion, the hotplate is switched off and allowed to cool to room temperature with the wafer still on it. We then spin on SU-8 2025 which has been thinned with cyclopentanone (3:2 Resist:Solvent ratio, results in roughly the same parameters as SU-8 2005) to create the waveguide core layer of the mold. The wave guide core layer is aligned to the electrode layer by observing the gold alignment marks on the mask aligner (MJB3). After post exposure bake, the features are clearly visible under an optical microscope, due to the refractive index contrast between the

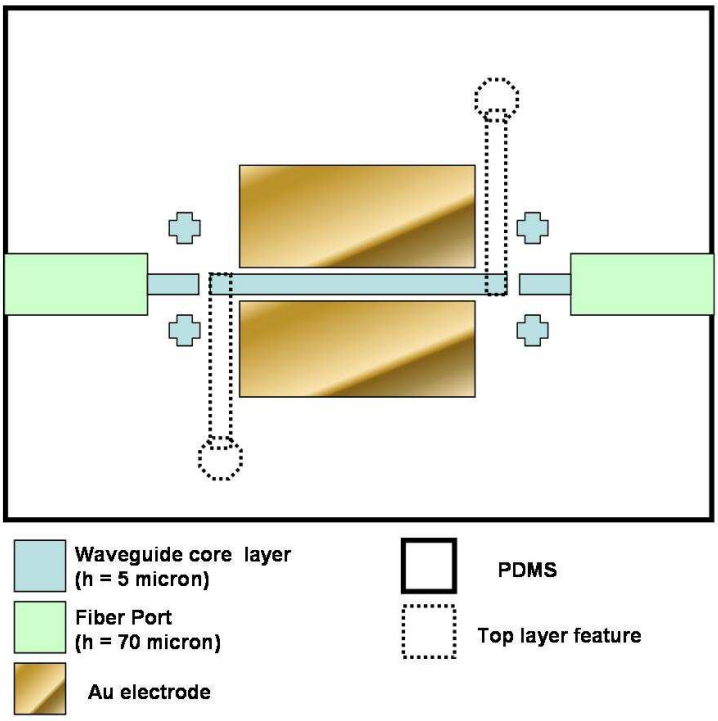

Figure 2.12: The elements of the pollable waveguide that are implemented in the bottom PDMS layer

crosslinked and uncrosslinked SU-8.

Following the definition of the waveguide core layer, the fiber access port is fabricated using SU-8 2100 The thick photoresist edge bead must be removed in order to accurately align the fiber port to the core layer. This is accomplished by wiping away the edge bead with an acetone soaked swab after the prebaking step. Because of the width of the feature is 150 microns, alignment errors of up to five microns are acceptable. The fiber port resist layer is exposed, and then the pattern is developed by immersion in SU-8 Developer (Propelyne Glycol Methyl Ether Acetate). During development, the agitation must be very gentle, to prevent the detachment of the features due to adhesion failure. The waveguide core features are most vulnerable to

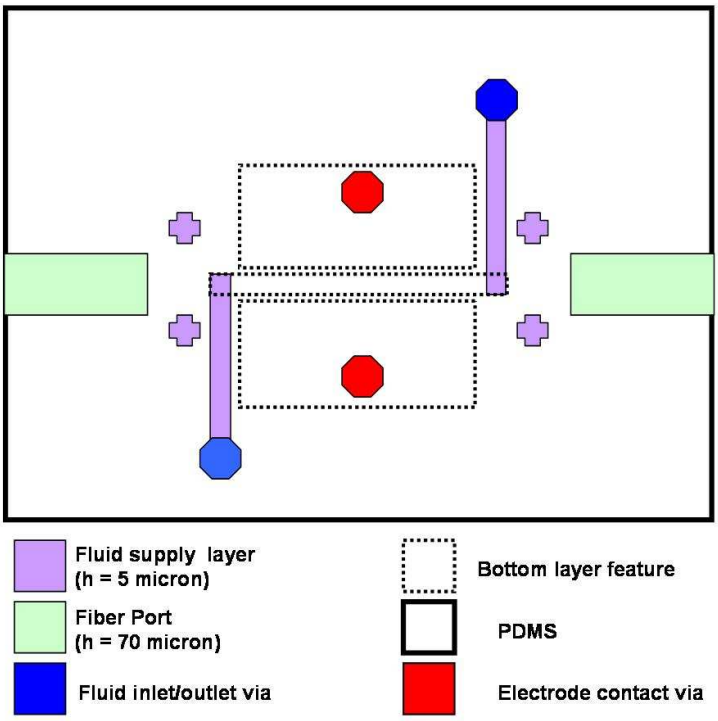

Figure 2.13: The elements of the pollable waveguide that are implemented in the top PDMS layer

adhesion failure, having a narrow cross section of 15 microns by 5 microns, and length over a centimeter. After developing, the pattern is gently rinsed with IPA and then baked for over an hour at 180 °C. This final hard bake step completes cross linking and makes the channel molds more resistant to damage during the casting process. A portion of a completed mold is shown in figure 2.14.

The mold is prepared for casting by exposing it to a vapor of 3-Mercapto-Silane (MPT) in a vacuum chamber for 4 hours. The MPT molecules form a monolayer on the gold surfaces. This monolayer will act as a bonding agent that will cause the gold to adhere to the PDMS during the casting process, enabling the transfer of the gold to the PDMS when the cured channel is removed from the mold. Next, the mold is

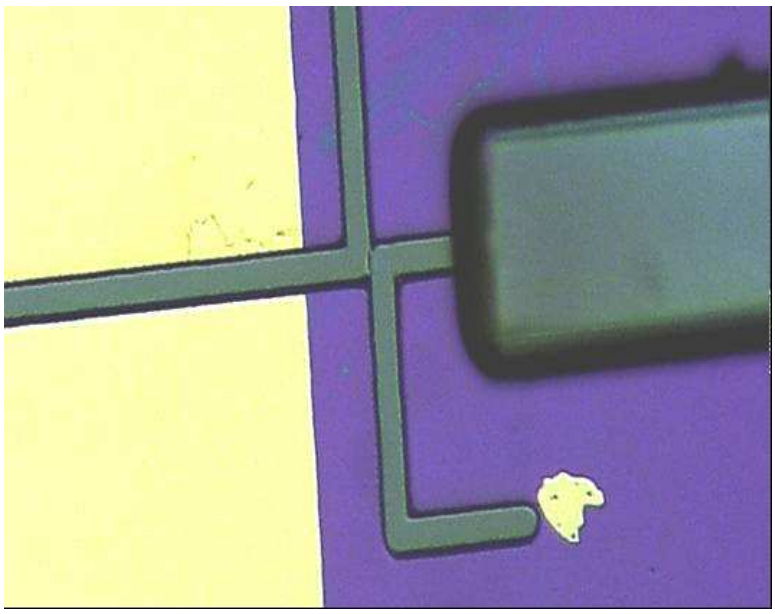

Figure 2.14: Detail of fabricated channel mold with gold electrodes in place

placed in a vapor of TMCS (at ambient pressure), which bonds to the silicon wafer and acts as a mold release agent for the cured PDMS. The PDMS is prepared from a mixture of GE RTV615 parts A and B; the mechanical properties of the PDMS chip are determined by the ratio of base (Part A) to the catalyst(part B). A 5:1 base to catalyst ratio produces stiffer PDMS, with an excess of free vinyl groups that allow for stronger reversible bonding between the chip and another PDMS surface. However, we found that a 10:1 ratio allows for better transfer of the gold from the mold to the PDMS. Since the most common fabrication failure in our process was incomplete embedding of the gold layer into the PDMS, the 10:1 formulation was used to create the bottom layer of the device.

The mold is placed in a foil lined petri dish. We pour the PDMS into the petri dish, and degas the mixture by placing it in a evacuated chamber for 1 hour. The dish is then baked in a convection oven at 80 °C to cure the PDMS. In order to cleanly transfer the gold layer from the mold with minimal cracking of the metal, Lee et al. suggest placing a glass slide on top of the PDMS when it is in a partially cured state [32] (i.e. after 15-20 minutes of baking). Once the PDMS has fully cured

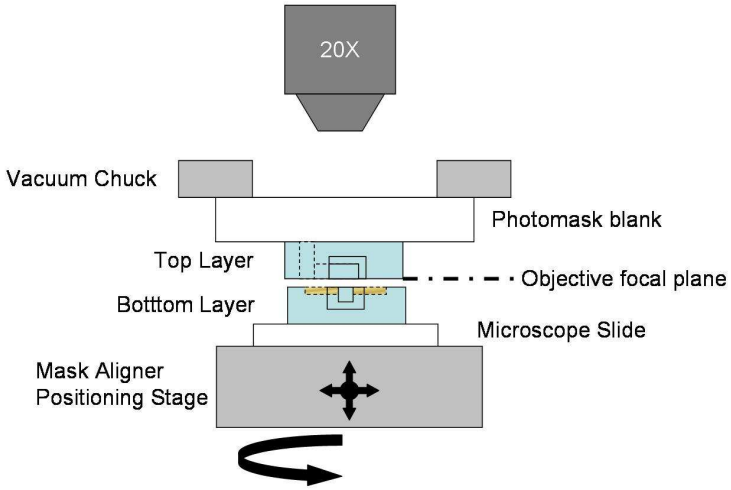

Figure 2.15: Alignment procedure for two layer chip.

(approximately 1 hour), this glass support is used to keep the PDMS layer flat as it is detached from the mold. In our experience, placing the glass substrate onto the partially cured PDMS surface is a delicate, highly time sensitive step. If the PDMS has not set enough to support the slide it may sink into the surface slightly, causing the support to be tilted with respect to the mold. This greatly complicates a clean removal of the gold with the PDMS, and also the subsequent alignment of the fabricated chip with the top layer casting. Conversely, if the PDMS is too well cured when the glass is introduced, the adhesion between the glass and PDMS is poor, causing the chip to detach from the support, cracking the gold pattern. We found it was easier to ensure good bonding between the PDMS and the glass support by fully curing the PDMS, and then exposing both the glass slide and the PDMS surface to a brief oxygen plasma treatment (10-15 seconds at 75 W, 250 mT. The plasma process facilitates irreversible bonding of the PDMS layer to the glass [33]. After the plasma treatment, the glass slide is placed on the PDMS surface and the device is baked at 80 °C for another hour, strengthening the bonding. The top layer mold is prepared in the much same manner. However, the fabrication is simpler because the top layer has no gold that must be transfered into the casting. We thermally evaporate a thin

adhesion layer of chrome (15 Å) before the gold evaporation, so that the alignment marks adhere well to the top layer mold. The wafer is processed using the same process flow as the bottom layer mold, with the addition of a wet chrome etch step (CR-7 chrome etch) immediately following the gold etch. The MPT treatment is omitted, since we do not want adhesion of PDMS to the metal. We cast the top layer PDMS chip from the mold using a 10:1 ratio. Using the same base to catalyst ratio has the advantage that the two layers have the same mechanical properties, thermal expansion, and refractive index. The disadvantage is that it is more challenging to successfully bond the top layer to the bottom layer. Again bonding is encouraged by plasma treatment of both device layers. Immediately after the plasma treatment, the two layers are aligned with each other using a modified mask aligner setup (see fig. 2.15 and then baked. The alignment must be performed within about 10 minutes of etching due to the quick relaxation of the plasma activated surfaces to their original state [34]. After baking overnight at 80 °C the device is ready for use.

2.4.1 Experiment

The finished chip is mounted so that it can be observed from above by stereoscope, and from below by a 10$\tilde{\text{X}}$ magnification microscope objective. The liquid core waveguide is filled with a glycerol-water mixture with a refractive index of 1.42. The same mixture is injected into the fiber port to allow coupling between the insertion region and the main waveguide. The waveguide is inspected using the microscope objective to ensure that the liquid core waveguide is completely filled, and there are no air bubbles or blockages that will interrupt to propagation of light.

The wave guide is end fire coupled by inserting a SMF-28 fiber, with its jacket removed, into the fiber port. SMF-28 has a cladding diameter of 125 microns, so there is room within the 140 x 140 micron fiber port to adjust the fiber's position and align the core of the fiber to the liquid core waveguide. The fiber is mounted

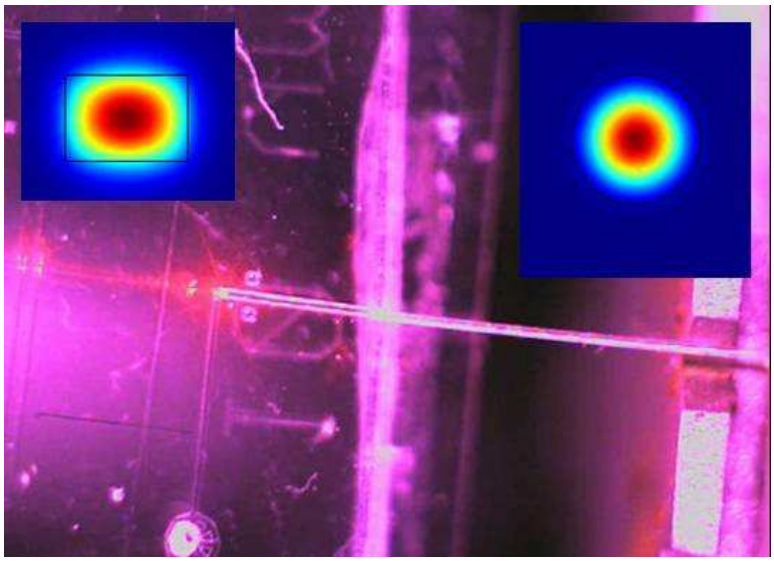

Figure 2.16: Input coupling of SMF-28 fiber to microchannel waveguide

onto a 3-d micropositioning stage with a v-groove tip-tilt fiber holder (Newport Co.). Insertion and alignment are performed by adjustment of the micropositioning stage, while observing from above through the stereoscope (See figure 2.16. The coupling of the fiber to the waveguide is maximized by observing the light transmitted through the waveguide structure. Figure 2.17 shows the experimental setup. The output of the waveguide is collected by a 10 X microscope objective. The output intensity is measured by using a field stop to reject light that does not originate from the wave guide region.

Figure 2.18 shows the output of the fluid waveguide. Linearly polarized light from 785 nm laser diode was coupled into the on chip waveguide using a SMF-28 fiber. However, under applied voltages up to 10 volts at 10-1000 Hz, no change in the polarization state or intensity of the guided light was observed. We tested electrode operation by injecting liquid crystal material (E7 nematic liquid crystal) into the waveguide. Observing the device in a microscope under crossed polarizers multiple LC domains are apparent. These domains change their alignment in response to the applied fields, verifying the presence of a strong electric field across the waveguide.

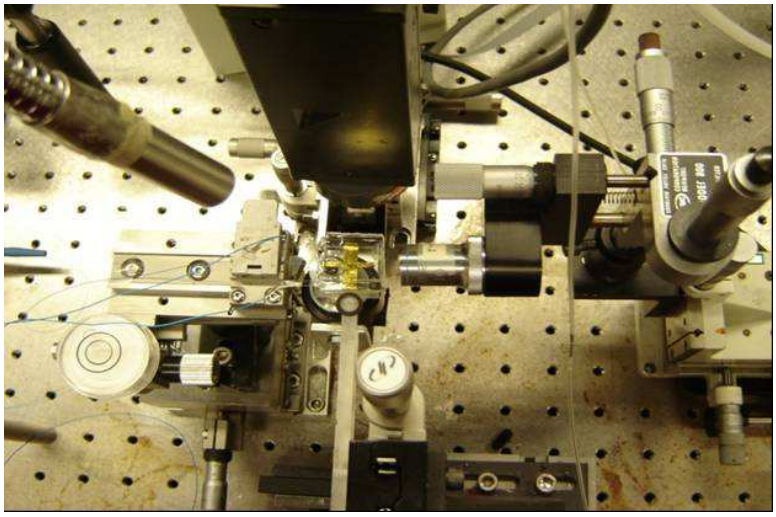

Figure 2.17: Experimental setup for measuring guided wave output.

We hypothesize that alignment of the nanorods is not observed due to the action of ions in the glycerol-water suspension medium. Free ions in solution, which are not present in the pure liquid crystal material, can act to screen the electric field, reducing its strength within the channel.

2.5 Future Work

We have successfully fabricated aligned microchannels that guide laser light from end to end with integrated electrodes for electro-optic experiments on liquid suspensions. However, our goal of inducing birefringent and dichroic behavior in these wave guides using suspensions of nanoparticles has not yet been achieved. Work is ongoing to try to characterize the electric field within the microchannel. The effect of ionic screening can be mitigated by transfer of the gold nanorods into a non-polar solvent. In addition, we would like to move to waveguides with smaller lateral dimension. The 15 micron wide waveguide we have fabricated supports multiple modes at both 633 nm and 785 nm. In order to properly quantify the effect of particle orientation, single mode operation is desirable. Attempt to fabricate waveguides with widths less than

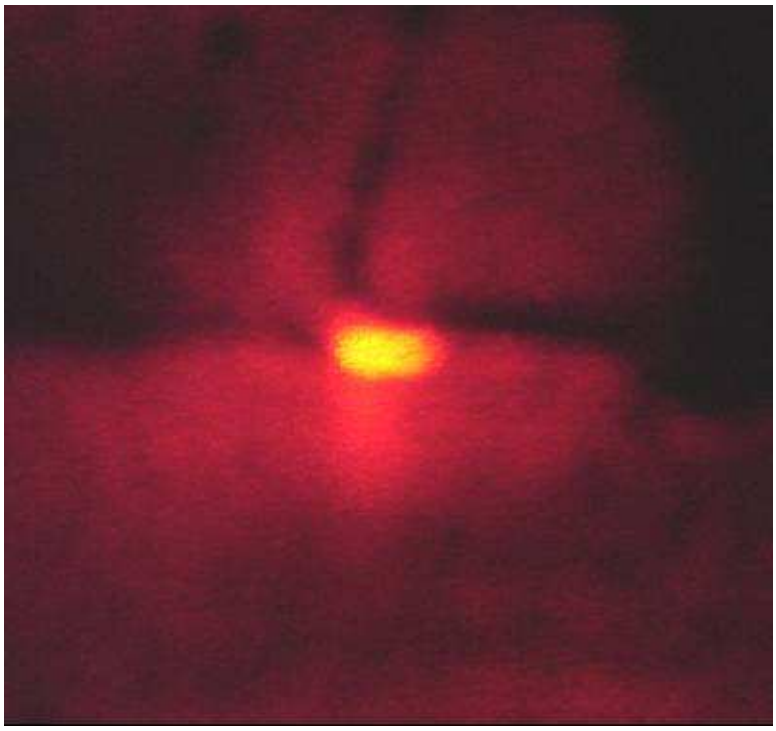

Figure 2.18: Image of output from liquid core waveguide, $\lambda = 633$ nm

10 microns have so far been unsuccessful due to the problem of SU-8 adhesion to a silicon wafer that has already undergone significant processing to define the electrode pattern. The stress on a thin SU-8 film with such an extreme aspect ratio (1O microns wide with length over 1 cm) causes adhesion failure of these patterns. Modification of the process flow to remove surface contamination before the definition of small SU-8 features needs to be investigated. Implementation of smaller waveguides would also increase electric field strength within the channel allowing for the alignment of nanosized particles.

References

[1] N. W. Ashcroft and N. D. Mermin. *Solid State Physics*. Saunders College, Philadelphia, 1976.

[2] J. B. Pendry. Negative refraction makes a perfect lens. *Phys. Rev. Lett.*, 85(18):3966–3969, 2000.

[3] D. R. Smith, J. B. Pendry, and M. C. K. Wiltshire. Metamaterials and negative refractive index. *Science*, 305(5685):788–792, 2004.

[4] R. W. Boyd. *Nonlinear Optics, Second Edition*. Academic Press, New York, 2002.

[5] G Mie. Articles on the optical characteristics of turbid media, especially colloidal metal solutions. *Annalen der Physik*, 25(3):377–445, MAR 1908.

[6] H. C. van de Hulst. *Light Scattering by Small Particles*. Dover Publications, NEW YORK, 1981.

[7] R. G. Newton. Optical theorem and beyond. *Am. J. Phys.*, 44(7):639–642, 1976.

[8] C.P. Collier. *Design and characterization of a reversible metal-insulator transition in silver quantum dot monolayers*. PhD thesis, University of California, Berkeley, Fall 1998., 1998.

[9] U. K. Kreibig and M. Vollmer. *Optical Properties of Metal Clusters*. Springer-Verlag., New York, 1995.

[10] C. L. Nehl, N. K. Grady, G. P. Goodrich, F. Tam, N. J. Halas, and J. H. Hafner. Scattering spectra of single gold nanoshells. *Nano Lett.*, 4(12):2355–2359, 2004.

[11] J. J. Mock, M. Barbic, D.R. Smith, D. A. Schultz, and S. Schultz. Shape effects in plasmon resonance of individual colloidal silver nanoparticles. *J. of Chem. Phys.*, 116(15):6755–6759, 2002.

[12] S. Link, C. Burda, B. Nikoobakht, and M. A. El-Sayed. How long does it take to melt a gold nanorod? A femtosecond pump-probe absorption spectroscopic study. *Chem. Phys. Lett.*, 315(1-2):12–18, 1999.

[13] S. Link and M. A. El-Sayed. Spectroscopic determination of the melting energy of a gold nanorod. *J. Chem. Phys.*, 114(5):2362–2368, 2001.

[14] R. Jin, Y.W. Cao, C.A. Mirkin, KL Kelly, G.C. Schatz, and JG Zheng. Photoinduced Conversion of Silver Nanospheres to Nanoprisms, 2001.

[15] C. F. Bohren and D. R. Huffma. *Absorption and scatttering of light by small particles*. Wiley, New York, 1983.

[16] E. Prodan, C. Radloff, N. J. Halas, and P. Nordlander. A hybridization model for the plasmon response of complex nanostructures. *Science*, 302(5644):419–422, 2003.

[17] SJ Oldenburg, RD Averitt, SL Westcott, and NJ Halas. Nanoengineering of optical resonances. *Chemical Physics Letters*, 288(2-4):243–247, 1998.

[18] Christian Hafner. *The Generalized Multipole Technique for Computational Electromagnetics*. Artech, Boston, 1990.

[19] M. Futamata, Y. Maruyama, and M. Ishikawa. Local Electric Field and Scattering Cross Section of Ag Nanoparticles under Surface Plasmon Resonance by Finite Difference Time Domain Method. *Journal of Physical Chemistry B*, 107(31):7607–7617, 2003.

[20] J.T.K. II, E.J. Sánchez, and X.S. Xie. Design of near-field optical probes with optimal field enhancement by finite difference time domain electromagnetic simulation. *The Journal of Chemical Physics*, 116:10895, 2002.

[21] B.T. Draine and P.J. Flatau. Discrete-dipole approximation for scattering calculations. *JOURNAL-OPTICAL SOCIETY OF AMERICA A*, 11:1491–1491, 1994.

[22] B.T. Draine and P.J. Flatau. User Guide for the Discrete Dipole Approximation Code DDSCAT 6.1. `http://arxiv.org/abs/astro-ph/0409262v2`, 2004.

[23] J.C. Love, B.D. Gates, D.B. Wolfe, K.E. Paul, and G.M. Whitesides. Fabrication and wetting properties of metallic half-shells with submicron diameters. *Nano Lett*, 2(8):891–894, 2002.

[24] Y. Lu, G.L. Liu, J. Kim, Y.X. Mejia, and L.P. Lee. Nanophotonic crescent moon structures with sharp edge for ultrasensitive biomolecular detection by local electromagnetic field enhancement effect. *Nano Lett*, 5(1):119–124, 2005.

[25] O. Cayre, V.N. Paunov, and O.D. Velev. Fabrication of asymmetrically coated colloid particles by microcontact printing techniques. *Journal of Materials Chemistry*, 13(10):2445–2450, 2003.

[26] O. Levy and D. Stroud. Maxwell Garnett theory for mixtures of anisotropic inclusions: Application to conducting polymers. *Physical Review B*, 56(13):8035–8046, 1997.

[27] S. P. Stoylov. *Colloid Electro-optics: Theory, Techniques, Applications*. Academic Press, New York, 1991.

[28] C.T. O'Konski, K. Yoshioka, and W.H. Orttung. Electric Properties of Macromolecules. IV. Determination of Electric and Optical Parameters from Saturation of Electric Birefringence in Solutions. *The Journal of Physical Chemistry*, 63(10):1558–1565, 1959.

[29] T. K. Sau and C. J. Murphy. Seeded high yield synthesis of short Au nanorods in aqueous solution. *Langmuir*, 20(15):6414–6420, 2004.

[30] A. Mata, A.J. Fleischman, and S. Roy. Fabrication of multi-layer SU-8 microstructures. *Journal of Micromechanics and Microengineering*, 16(2):276–284, 2006.

[31] Wen Dai, Kun Lian, and Wanjun Wang. A quantitative study on the adhesion property of cured su-8 on various metallic surfaces. *Microsyst. Technol.*, 11(7):526–534, 2005.

[32] K.J. Lee, K.A. Fosser, and R.G. Nuzzo. Fabrication of Stable Metallic Patterns Embedded in Poly (dimethylsiloxane) and Model Applications in Non-Planar Electronic and Lab-on-a-Chip Device Patterning. *Advanced Functional Materials*, 15(4):557–566, 2005.

[33] B.-H. Jo, L.M. Van Lerberghe, K.M. Motsegood, and D.J. Beebe. Three-dimensional micro-channel fabrication in polydimethylsiloxane (pdms) elastomer. *Journal of Microelectromechanical Systems*, 9(1):76–81, Mar 2000.

[34] M Morra, E Occhiello, R Marola, F Garbassi, P Humphrey, and D Johnson. On the aging of oxygen plasma-treated polydimethylsiloxane surfaces. *Journal Of Colloid And Interface Science*, 137(1):11–24, JUN 1990.

Chapter 3

Holographic measurement of thermal properties of suspensions

The high third-order nonlinear response of nanoparticles for wavelengths close to the surface plasmon resonance has been subject of intense studies [1, 2, 3]. Composite materials, such a metal doped glasses and polymer suspensions of metal nanoparticles have been studied as possible optical switches [4]. However, the losses inherent in the plasmonic resonance create thermal effects, which make such materials unsuitable for high frequency operation desired in optical computation and communications.

These limitations do not apply to techniques which use photothermal energy to measure and manipulate the physical properties of their surroundings, where the timescales of interest are in the picosecond to nanosecond range. Since the absorption due to the nanoparticles also causes heating of the surrounding solvent, a temperature pattern can be created by means of structured illumination. This leads to a thermal change of the refractive index, as well as to a particle redistribution caused by the so-called Soret-effect [5]. These thermal forces or the use of optical tweezers can allow on demand configuration of, e.g., microfluidic devices or holographic Bragg filters [6]. An advantage of colloidal suspensions compared to fabrication of structures in doped glasses is that the nanoparticles in suspension are easily reconfigurable [7]. By choosing the right illumination conditions it is not only possible to transport and structure the nanoparticle distribution, but also to get a patterned nonlinear optical

response.

In this work, we study the optical and thermal response as well as the transport properties of colloidal suspensions of silver nanoparticles. In these materials, the light-matter interaction is still not completely understood, especially on the nanosecond timescale [8]. We probe the material response by means of a simple holographic experiment.

3.1 Holographic Thermal Conductivity Measurement

Elementary holographic gratings are recorded with nanosecond pulses in samples of different volume fractions of nanoparticles. The diffraction efficiency of these gratings is monitored with continuous-wave light. Maximum diffraction efficiencies of around 3 percent were measured, corresponding to phase gratings with refractive index contrast of approximately 1×10^{-5}.

Experiments are performed with chemically synthesized silver spheres with a mean diameter of $\approx 3.8\,\mathrm{nm}$ suspended in toluene. Synthesis was carried out using a modified version of the Brust protocol[9], as developed by the Heath group [10].

The absorption properties of the solutions were studied using a spectrophotometer. Absorption was measured from 350–850 nm. The surface plasmon resonance has its maximum around 435 nm. Different concentrations between $3.5 \times 10^{14}\ \mathrm{cm}^{-3}$ and $0.7 \times 10^{14}\,\mathrm{cm}^{-3}$ (Optical density (OD) at 532 nm of 1.1–0.22) were produced by dilution. The particle size is determined from the measured spectra using Mie theory calculations with a semiclassical correction, following Collier.[10] For details of the synthesis and characterization of the nanoparticles see chapter 2.

To record a holographic grating we interfere two plane waves. Frequency-doubled pulses from a Nd:YAG laser (wavelength $\lambda = 532\,\mathrm{nm}$, intensity $I = 10\,\mathrm{GW\,m^{-2}}$, pulse

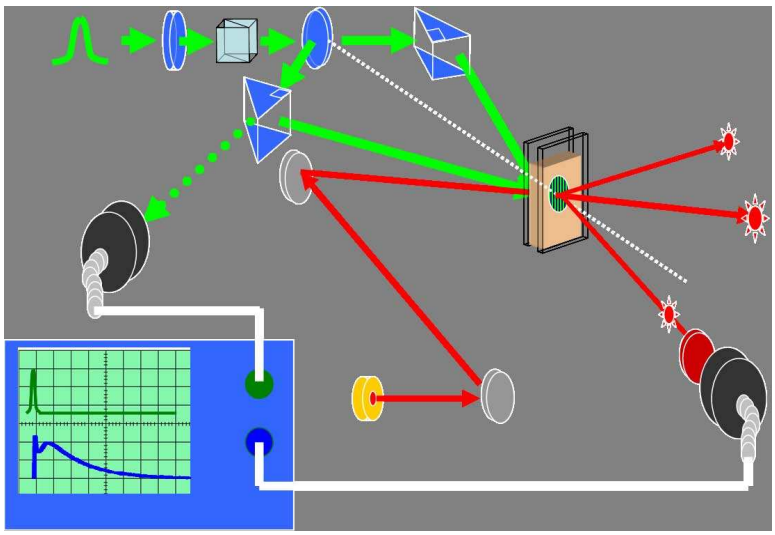

Figure 3.1: Experimental setup for ns thermal hologram recording

duration $\tau = 6\,\text{ns}$ FWHM, beam diameter 6 mum) are split into two parts of equal intensity that overlap and interfere inside a 4 mm thick and 10 mm wide cuvette filled with the nanoparticle suspension. The angle between the pulses can be adjusted such that grating periods Λ between 1 μm and 2.5 mum are possible. The induced grating is observed by diffracting a Bragg-matched, continuous-wave beam of a laser diode at $\lambda = 785\,\text{nm}$ with a beam diameter of 2 mm. All three beams are s-polarized. A fast photodiode with a risetime of 1 ns and a digital oscilloscope (bandwidth 1 GHz) are used to capture the time evolution of the diffracted signal. A band pass filter (800 nm, 40 nm FWHM) at the read-out wavelength blocks the pump light at the detector. A schematic drawing of the experimental setup is shown in 3.1. Between each recording experiment the sample is allowed to cool down for at least one minute to avoid excessive heating of the solvent. This time is also sufficient to flatten out a possible concentration distribution of the nanoparticles [5]. The absorption spectra of all samples were measured before and after each experiment, and no change was observed. This indicates that the pulsed illumination does not lead to agglomeration or shape changes of the nanoparticles.

The diffraction efficiency of the grating depends strongly on the concentration of the nanoparticles and on the light intensity. At lower intensities, the diffracted signal shows an abrupt rise time of around 6 ns nanoseconds, and then a monoexponential decay with a time constant of $\tau = 220\,\text{ns}$. This decay time constant does not vary with concentration (Fig. 3.1(a,b,c)). At the highest intensities measured, the time evolution of the diffracted signal is qualitatively different for different concentrations (Fig. 3.1(d,e,f)). At the two lower concentrations (OD 0.32, 0.22) the initial rise still occurs in 6 ns, followed by a dip and a slower second rise that peaks at around 150 ns. This is followed by the decay of the grating, with the same time constant as before (Fig. 3.1(f)). At the intermediate concentration (OD 0.55) the first minimum is not present. However there is still a slow rise and decay of the signal. (Fig. 3.1(e)). Finally, at the highest concentrations and intensities, an initial peak is again present in the diffracted efficiency curve. The magnitude of the first maximum is now smaller than the second. The rise and fall times of the first peak are faster, at around 3 ns (Fig. 3.1(d)). Comparing measurements at different intensities in single samples, we see a smooth evolution in the behavior of the diffracted signal. At low intensities, a monoexponential decay is seen, and as intensity increases, the faster transient effects grow in magnitude. The position of the second maximum shifts to later times with increasing intensity (Fig. 3.3). Variation of the grating period length Λ between $1\,\mu$m and $2.4\,\mu$m has no influence on the first peak and on the build-up of the second one. However, the amplitude of the grating decays slower with increasing grating spacings, clearly pointing to thermal effects (Fig. 3.4). Thus the final time evolution of the diffraction efficiency can be explained by the presence of a thermal grating in the solvent: Energy absorbed by the nanoparticles heats the solvent. Since each nanoparticle heats a spherical volume of solution with diameter equal to the mean interparticle spacing 150 to 250 nm), there can be some delay in building up a smooth sinusoidal temperature distribution. In our experiments, a strong thermal grating has

been established by 200 ns after the recording pulses. The decay afterward is governed solely by thermal conductivity and can be used to determine the thermal diffusivity of the sample [11, 12]. The temperature amplitude ΔT of the thermal grating decays exponentially

$$\Delta T = T_0 \exp(-t/\tau_{\text{th}}), \tag{3.1}$$

with the time constant

$$\tau_{\text{th}} = \frac{\Lambda^2}{4\pi^2\kappa}. \tag{3.2}$$

Here, κ is the thermal diffusivity of the solvent. The refractive-index change of the solvent is proportional to ΔT and hence according to the coupled-wave theory,[13] the diffraction efficiency is proportional to the square of the temperature change for small diffraction efficiencies.

From the fit in figure 3.4 and taking into account the factor of two between the time constants for the diffraction efficiency and the refractive-index change for small diffraction efficiencies, we can then calculate the thermal diffusivity of the solvent to $7.27 \times 10^{-8}\,\text{m}^2/s$. This is in good agreement with a literature value of $8.85 \times 10^{-8}\,\text{m}^2/\text{s}$.

The temporal evolution for times less than 200 ns is more complex. At low concentrations and intensities the diffraction efficiencies are consistent with a simple thermal grating. However, as the intensity increases, another transient signal appears. Also, the maximum diffraction efficiency scales linearly with intensity, instead of quadratically. The disappearance of the dip between the first and second maximum for intermediate concentrations, as well as the change in position and magnitude of the second maximum relative to the first, suggest that there is more than one physical effect operating on the short time scale (Fig. 3.1).

Different mechanisms for optical nonlinear effects in solutions of metal nanoparticles are known [14]. Changes of the polarizability of the particles due to hot electrons

and electron-dipole transitions are instantaneous in the nanosecond regime. Also the field enhancement in the vicinity of the particles due to the surface plasmon resonance may lead to a high instantaneous Kerr nonlinearity in the solvent. Measurements with femtosecond and picosecond pulses show positive nonlinear refractive index changes of either the nanoparticles or the solvent. Heating of the solvent leads to thermal and thus negative changes of the refractive index.

Despite the fast thermalization of absorbed energy by the metal nanoparticles, it has been shown that the heat transfer from nanoparticles excited by nanosecond pulses to the solvent can last for several tens of nanoseconds. This behavior is strongly influenced by both particle size and concentration [8]. This diffusion of thermal energy into the solvent could be the mechanism responsible for the discrepancies in the temporal evolution of the first peak and valley. A thermally induced modification of the optical properties of the particles can perhaps lead to a change of the fast nonlinear response. But another explanation may be possible: The absorbed energy is maybe sufficient to boil a small shell of the solvent around each nanoparticle, thus leading to strong refractive-index changes, resulting in a change of the surface plasmon resonance and in light scattering at the phase boundary in the solvent [15].

In either case, the refractive index grating shortly after the pump pulse could be described as the sum of an instantaneous Kerr effect, a fast forming simple thermal grating accounting for the monoexponential trend, and a shorter lived delayed grating due to the thermal changes in the particles and the solvent. The Kerr grating would cause a real positive refractive index change, the thermal grating a negative index change and the delayed grating a possibly complex refractive index change. Further investigation is required to determine the exact parameters of these gratings.

3.2 Spatial Resolution of Thermal Gratings

As these experiments show, the fitting of the slow thermal decay of a thermooptic grating is an effective probe of the thermal conductivity. It is possible to extend this technique as a scanning method to perform measurements of the thermal properties of liquid systems with microscopic spatial resolution.

Detailed knowledge of thermal properties plays a major role in several areas of science and technology. The thermal diffusivity as a function of space is an important parameter for the production of active semiconductor devices, and also for characterization of structured material systems and biological organisms [16]. Several methods to measure the thermal diffusivity in solids with spatial resolution exist, but liquids pose a greater challenge challenging [16]. The thermal behavior of liquid two-component systems is very important in a biological context. For instance, Oil/water systems can be considered as simple models of cell membranes [17, 18]. Knowledge of the local thermal diffusivity in cells gives information about cytochemical processes and allows new methods of cellular imaging [19].

We extend our holographic method described above to measure the thermal diffusivity, $D_{th} = \kappa/\rho c_p$, with a resolution of $150\mu m$ in a sample containing two imiscible liquids. Here κ is the thermal conductivity of the liquid, ρ is the liquid density, and c_p is its heat capacity at constant pressure. The measurement is again preformed by superimposing two laser pulses to form a sinusoidal light intensity pattern with wavelength Λ in an absorbing liquid sample. Light from a continuous wave probe laser is diffracted from thermal phase grating produced by absorption. By measuring the diffraction of the probe beam as a function of time, we monitor the decay of the grating. The temperature grating decays with an exponential time constant due to heat conduction between the fringes [20]. The diffraction efficiency of the thermal phase grating, $\eta(t) = I_{diff}(t)/I_0$, is proportional to the square of the refractive index

change,[13] hence it also decays exponentially. Here, $I_{diff}(t)$ is the intensity of the diffracted light, and I_0 is the intensity of the incident probe beam. It should be noted that these considerations are valid for volume gratings in one component systems, which means the grating region should be uniform throughout the probe region of interest [20, 11]. It follows that

$$\eta(t) = \eta_0 \exp(-t/\tau_{obs}), \tag{3.3}$$

where τ_{obs} is the decay time constant, and η_0 is the initial diffraction efficiency. By fitting the measured I_{diff} by an exponential, it is simple to determine τ_{obs}. Using τ_{obs} the thermal diffusivity can be calculated according to

$$D_{th} = \frac{\Lambda^2}{8\pi^2 \tau_{obs}} \quad \text{s.t.} \quad \tau_{obs} \propto \frac{1}{D_{th}}. \tag{3.4}$$

Experiments were performed by Judith Schwesyg and Helge Eggert at University of Bonn, Germany. A frequency-doubled Nd:Yag Laser (wavelength $\lambda = 532$nm, average pulse energy 100 mJ, FWHM pulse duration 16 ns , FWHM beam diameter $d_{pulse} = 8$mm). The pulse is split into two equal parts which interfere symmetrically throughout the sample. The angle between the two pulses is adjusted such that the period of the grating is 1.5 μm The probe is a continuous wave HeNe laser ($\lambda = 632.8$ nm) focused upon the sample cuvette in the center of the interference region. A long focal length lens ($f = 500mm$) is used to focus the probe beam, to ensure that the Bragg condition can be met. The measured probe beam diameter at the sample is 50 μm. The diffracted probe light is recorded with a fast photodiode and a digital oscilloscope. Four interference filters in front of the photodiode are used to block the pump light. The cuvette containing the sample is mounted onto a $x - y$-translation stage to scan the entire surface of the cuvette through the pobe. The sample cuvette has a width b =10 mm, and a thickness d =1 mm.

In order to absorb energy from the writing pulse and transmit the probe beam, the liquids were stained with red dye. Methyl red was added to toluene, and a polar red dye (Laco SF30) is added to the water. The concentration of each dye is chosen so that each solution will give simmilar diffraction efficiency when tested as a homogenous sample. Diffraction efficiency for all samples was in the range of 1 to 5 percent. Absorption measurements taken using the a Varain Cary 500 spectrometer give absorptivities of $\alpha_{532,Tol} \approx 1 - 2cm^{-1}$ for the toluene solutions and $\alpha_{532,H_2O} \approx 2.5 - 3.5cm^{-1}$ for the water solutions. For all samples the absortion at 632.8 nm is negligible. The absorption and thickness of the sample allow for the application of the volume hologram equations (equations 1 and 2) to be applied, i.e. $\Lambda \ll \alpha^{-}1$, $\Lambda \ll d$, and $\Lambda \ll d_{pulse}$ [11].

Figure 3.2 shows the diffraction efficiency $\eta(t)$ of dyed Toluene and dyed water versus time. Exponenetial fits describe the data very well, giving $\tau_{tol} = 343 \pm 4ns$ and $\tau_{H_2O} = 197 \pm 1ns$. With Eq. (2) this leads to $D_{th,tol} = (8.3 \pm 0.4) \times 10^{-}8m^2/s$ and $D_{th,H_2O} = (14.5 \pm 0.7) \times 10^{-}8m^2/s$. These values agree well with the literature data at $25 \deg C$, $D_{th,lit,tol} = 8.6 \times 10^{-}8m^2/s$ and $D_{th,H_2O} = 14.6 \times 10^{-}8m^2/s$.[21]

Moderate powers must be used to prevent the formation of acoustic nonlinearities in $\eta(t)$ such as those reported by Auth [22]. Such nonlinearites are generated by acoustic shock waves created at interfaces such as the surfaces of the cuvette and the interfaces between immiscible liquids. Since these waves are also spatially modulated with period Λ, they will noticeably disturb the diffracted light from the probe. By using appropriate absorption filters and working at lower light intensities, we avoid the appearance of accoustic effects such that $\eta(t)$ can be well fit with a single exponential. This allows accurate recovery of the thermal diffusivity for all points in the sample. A scan in a single dimension across a sample of water and toluene is shown in figure 3.2. The beam is scanned in the vertical (y) direction, across the liquid interface between toluene and water which is located at $y = 1.9mm$. For probe positions more

than $150\mu m$ from the interface in either direction, the measured $D_t h$ agrees well with the measured values for the single component samples. Near the interface, deviations of $D_t h$ up to 20% from the single component values are measured. In addition, the uncertainty of the measurement increases as the interface is approached.

These errors are likely due to the strong scattering and refraction of the curved interface between the two liquids, which prevent the Bragg matching of the probe to the thermal grating, and reduce the measured $\eta(t)$. However, due to their appreciable difference in thermal diffusivity, the two materials are clearly differentiated in the scan, and the position of the interface is marked by an obvious discontinuity. The spatial resolution of the scan is 150 μm, and is limited by the error introduced by the curved fluid interface. In principle, a resolution the size of the spot size could be obtained.

We also demonstrate thermal diffusivity imaging in two dimensions. In this experiment, a small water droplet is placed into a cuvette filled with toluene (the liquids have previously been stained as before). Due to the surface tension of the water drop, it clings to the front surface of the cuvette. The drop is surrounded by toluene, without contacting the rear or sides of the cuvette. The diameter of the water droplet is measured to be $400\mu m$.

Figure 3.2 shows the spatially resolved measurement of D_{th} for a two dimensional scan of the sample. The value of the thermal diffusivity at each pixel is recovered from an exponential fit to the measured $\eta(t)$. The imaging technique tends to slightly underestimate the size of the water droplet, due to the errors incurred at interface bending. The apparent size of the reconstructed image is slightly larger than 300 μm.

At first glance, it seems suprising that the measurements taken at the center of the water drop agree well with the thermal diffusivity of water reported in the literature. The light used to probe the droplet encounters both toluene and water, so one might expect that the measured value would be an weighted average of the

thermal diffusivities of both water and toluene. However, the light that passes through the water and into the toluene behind is refracted by the curved surface of the bubble, so that the recording beams and the probe beam no longer exactly satisfy the Bragg condition. For this reason, the toluene portion contributes little to the measured thermal diffusivity. This artifact is in the fact that we have used a two dimensional planar scan to sample a three dimensional spherical object. In conclusion, we have shown that photothermal recording of transient holograms can be used as an acurate probe of the thermal conductivity of liquids. A scanning approach was developed to visualize the local thermal diffusivity of a two liquid system. The main advantages of this method are that it works for small light powers so that the samples are not heated signifcantly in contrast to other methods[16] and that it works for any material, solid or liquid liquids or solids, which absorb the writing light and transmit the probe light. The method can be employed to study the mechanism of heat transfer acriss liquid-liquid-interfaces or liquid solid interfaces. Hence this technique is promising for detailed study in the field of microscopy of thermal diffusivity especially in liquids and biological samples [19, 23]. Remaining artifacts can be diminished by using smaller period lengths and smaller probe beam sizes as long as refraction due to curved interfaces is not too strong. Tomographic techniques could be adopted to allow full 3-d visualization of mixed material systems. Additionally, an expanded probe beam could be used to simulataneously read out the diffracted signal at every point in a 2-d sample with an ultrafast camera. The series of images formed would contain the temporal and spatial variation of the diffracted signal for every image point, allowing full recovery of the thermal conductivy map with a single shot.

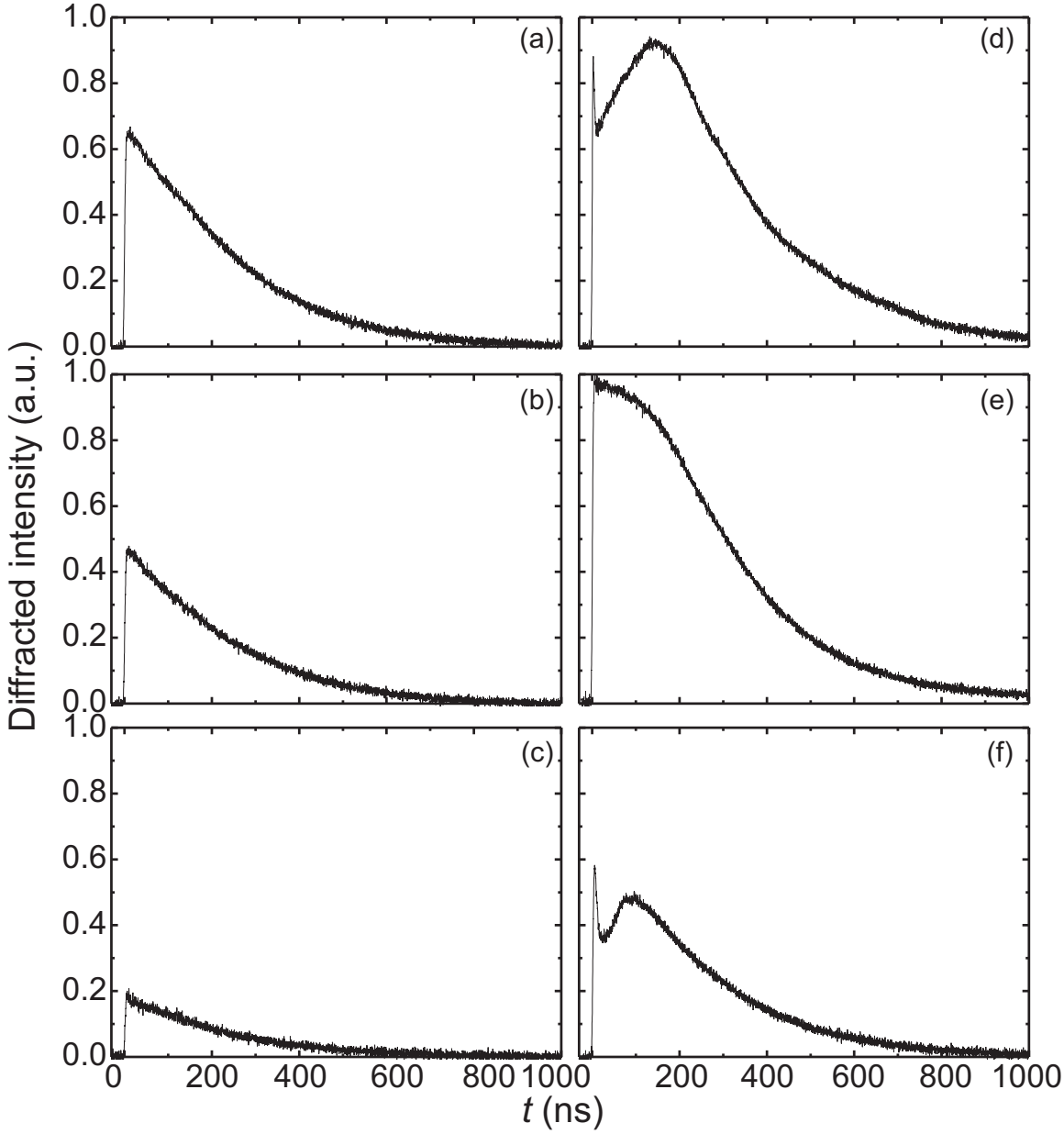

Figure 3.2: Intensity of the diffracted beam versus time t for different particle concentrations. The pump intensity is $I = 4.6$ GW/m^2 for (a,b,c) and $I = 10$ GW/m^2 for (d,e,f). (a, d) Particle concentration of 3.47×10^{14} cm^3 (OD = 1.1) (b, e) Particle concentration of 1.74×10^{14} cm^3(OD = 0.55) (c, f) Particle concentration of 0.7×10^{14} cm^3 (OD = 0.22).

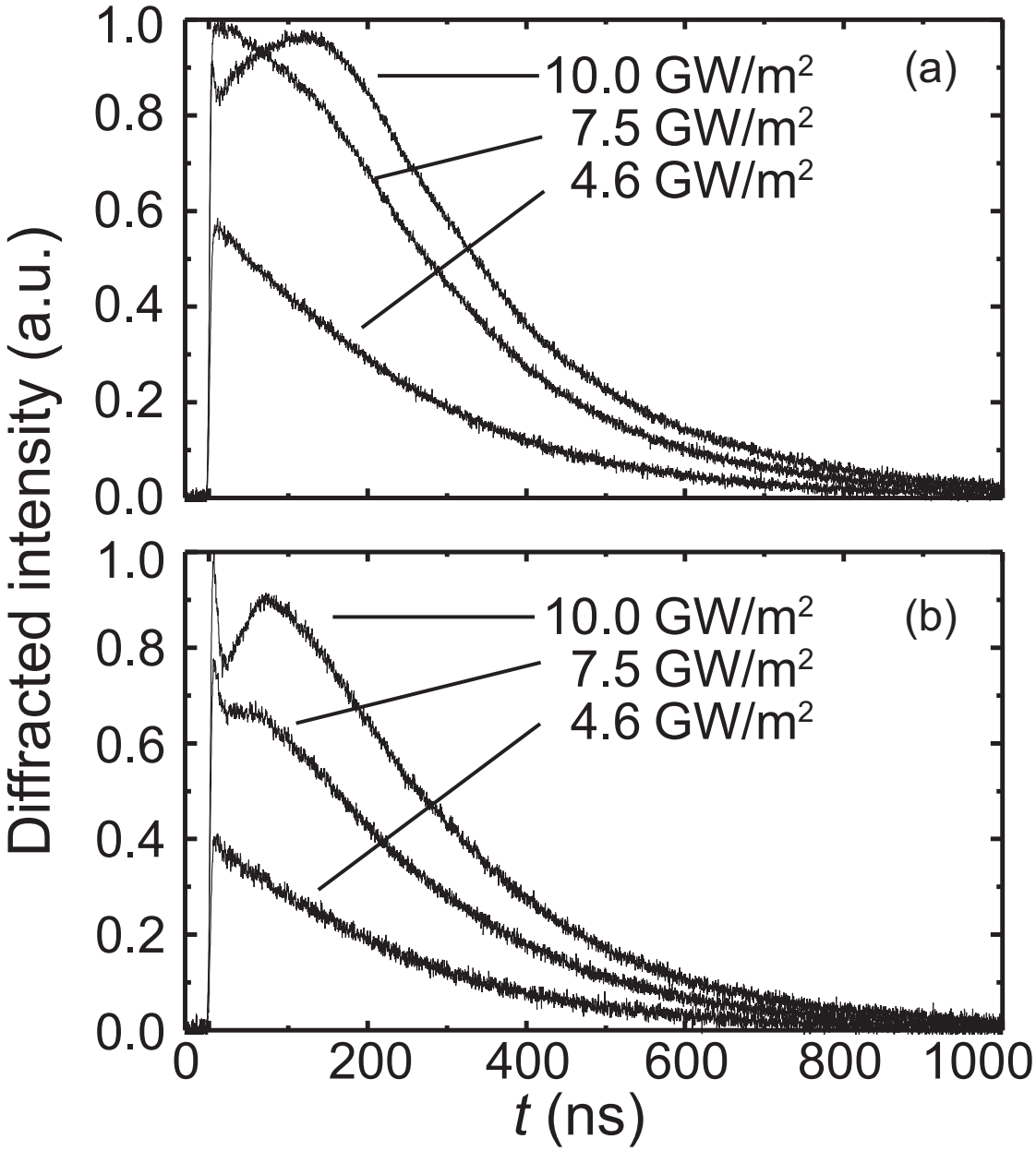

Figure 3.3: Diffracted intensity versus time t for three different pump intensities in (a) a sample with a particle concentration of 2.4×10^{14} cm^3(OD = 0.76) and (b) a particle concentration of 1.07×10^{14} cm^3 (OD = 0.34).

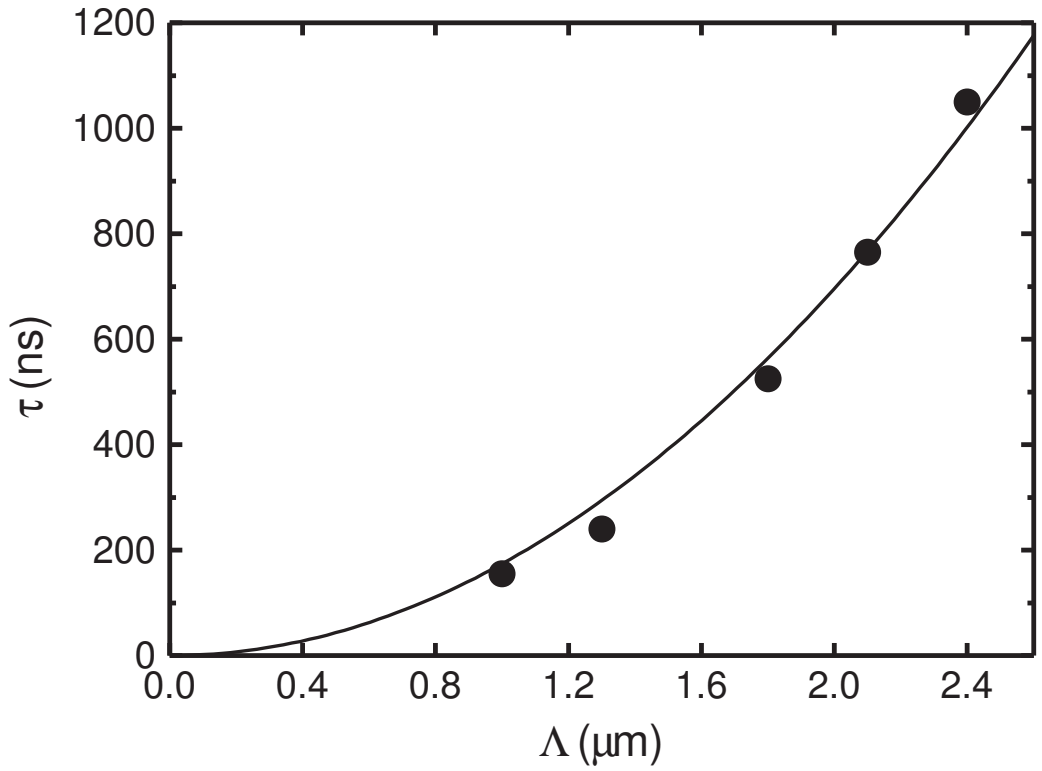

Figure 3.4: Time constant τ of the decay of the diffraction efficiency versus grating period Λ of the thermal grating. The solid line is a quadratic fit according to the equation $\tau = a \times \Lambda^2$.

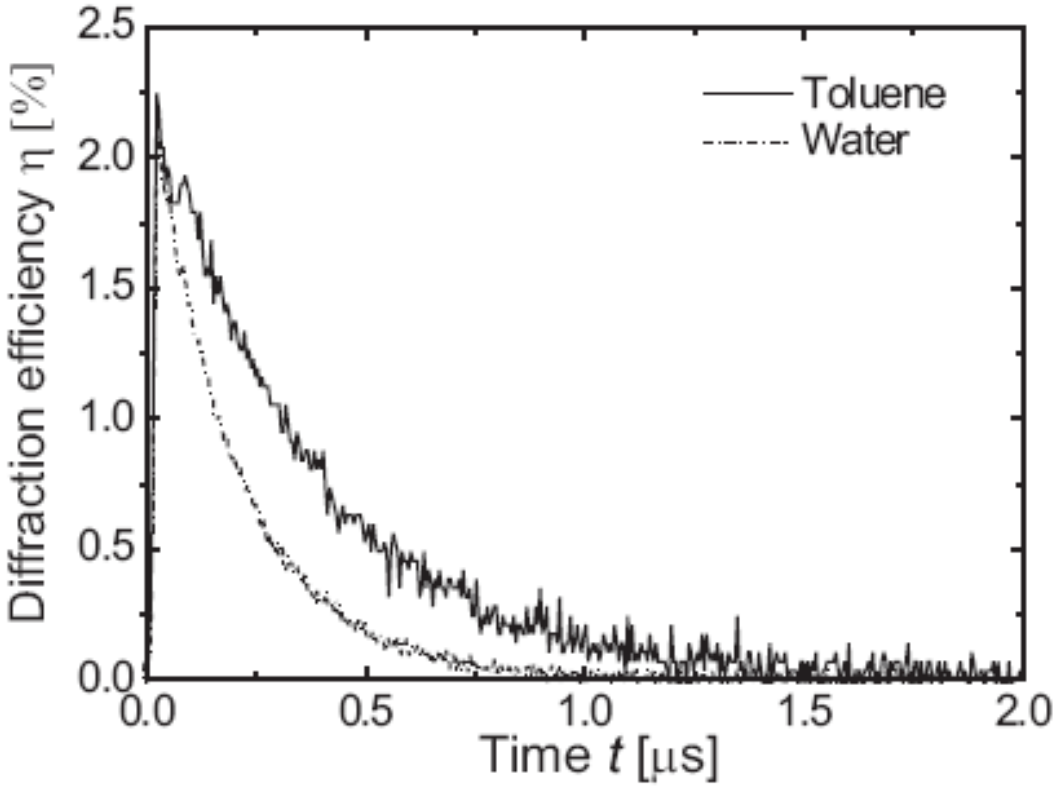

Figure 3.5: Diffraction efficiency $\eta(t)$ of both dyed water and toluene versus time.

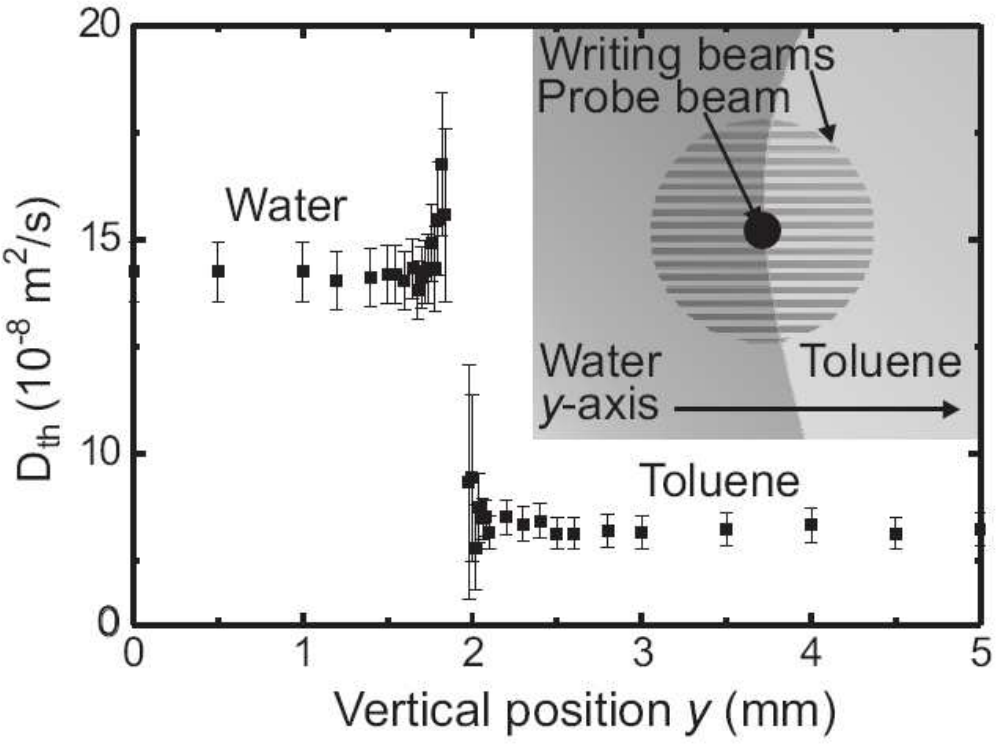

Figure 3.6: Thermal diffusivity measured in a 1D (y-axis) scan across a toluene water interface. Inset shows a schematic of the sample geometry

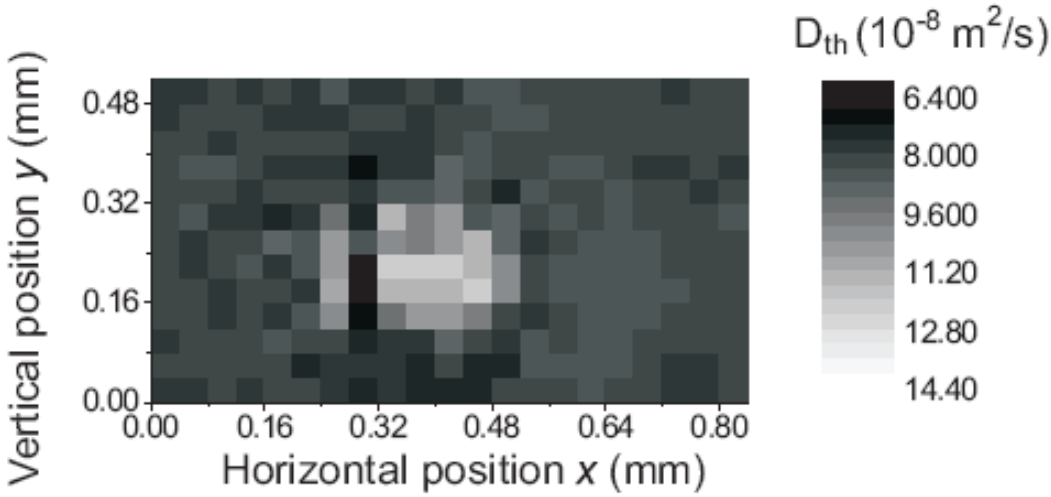

Figure 3.7: Two dimensional Thermal diffusivity scan of a $400\mu m$ diameter water drop in toluene.

References

[1] S. Link and M.A. El-Sayed. Optical properties and ultrafast dynamics of metallic nanocrystals. *Annual Review of Physical Chemistry*, 54:331–366, 2003.

[2] C. Voisin, N. Del Fatti, D. Christofilos, and F. Vallee. Ultrafast electron dynamics and optical nonlinearities in metal nanoparticles. *J. Phys. Chem. B*, 105(12):2264–2280, 2001.

[3] C. Flytzanis. Nonlinear optics in mesoscopic composite materials. *J. Phys. B*, 38:661–679, 2005.

[4] P. Chakraborty. Metal nanoclusters in glasses as non-linear photonic materials. *Journal of Materials Science*, 33(9):2235–2249, 1998.

[5] J. Lenglet, A. Bourdon, JC Bacri, and G. Demouchy. Thermodiffusion in magnetic colloids evidenced and studied by forced Rayleigh scattering experiments. *Physical Review E*, 65(3):31408, 2002.

[6] A. Terray, J. Oakley, and D. W. M. Marra. Fabrication of linear colloidal structures for microfluidic applications. *Applied Physics Letters*, 81:1555–1557, 2002.

[7] M. Rosenbluh, I. Antonov, D. Ianetz, Y. Kaganovskii, and AA Lipovskii. Microfabrication of structures by laser light in metal-doped glasses. *Optical Materials*, 24(1-2):401–410, 2003.

[8] M. Rashidi-Huyeh and B. Palpant. Thermal response of nanocomposite materials under pulsed laser excitation. *Journal of Applied Physics*, 96:4475, 2004.

[9] M. Brust, M. Walker, D. Bethell, D.J. Schiffrin, and Whyman R. synthesis of thiol-derivatized gold nanoparticles in a 2-phase liquid-liquid system. *journal Chem. Society-chemical Comm.*, 7(7):801– 802, 1994.

[10] C.P. Collier. *Design and characterization of a reversible metal-insulator transition in silver quantum dot monolayers.* PhD thesis, University of California, Berkeley, Fall 1998., 1998.

[11] H. Eichler, G. Salje, and H. Stahl. Thermal diffusion measurements using spatially periodic temperature distributions induced by laser light. *Journal of Applied Physics*, 44:5383, 1973.

[12] Y. Nagasaka, T. Hatakeyama, M. Okuda, and A. Nagashima. Measurement of the thermal diffusivity of liquids by the forced Rayleigh scattering method: Theory and experiment. *Review of Scientific Instruments*, 59:1156, 1988.

[13] H. Kogelnik. Coupled wave theory for thick hologram gratings. *The Bell System Technical Journal,*, 48(9):2909–2947, 1969.

[14] HB Liao, RF Xiao, JS Fu, H. Wang, KS Wong, and GKL Wong. Origin of third-order optical nonlinearity in Au: SiO_2 composite films on femtosecond and picosecond time scales. *Optics Letters*, 23(5):388–390, 1998.

[15] F. Lang, P. Leiderer, and S. Georgiou. Phase transition dynamics measurements in superheated liquids by monitoring the ejection of nanometer-thick films. *Applied Physics Letters*, 85:2759, 2004.

[16] A. Majumdar. Scanning thermal microscopy. *Annual Review of Materials Science*, 29(1):505–585, 1999.

[17] LE Morrison and G. Weber. Biological membrane modeling with a liquid/liquid interface. Probing mobility and environment with total internal reflection excited fluorescence. *Biophysical Journal*, 52(3):367–379, 1987.

[18] K. Arai, M. Ohsawa, F. Kusu, and K. Takamura. Drug ion transfer across on oil-water interface and pharmacological activity. *Bioelectrochemistry and bioenergetics*, 31(1):65–76, 1993.

[19] W. Haeberle, M. Pantea, and JKH Hoerber. Nanometer-scale heat-conductivity measurements on biological samples. *Ultramicroscopy*, 106(8-9):678–686, 2006.

[20] HJ Eichler, P. Gunter, and DW Pohl. Laser-Induced Dynamical Gratings, 1986.

[21] D.R. Lide et al. *CRC handbook of chemistry and physics*. CRC Press, 2003.

[22] DC Auth. New high-power source of coherent microwave phonons. *Applied Physics Letters*, 16:521–523, 1970.

[23] M. Hartung and W. Köhler. The role of heat-conducting walls in the measurement of heat and mass transport in transient grating experiments. *European Physical Journal E*, 17:165–179, jun 2005.

Chapter 4

Photothermal Bubble Assisted Vapor Transport in Microchannels

In this chapter we will discuss the actuation of microfluidic systems driven by photothermal energy. The emergence of optofluidics as a design philosophy has promoted interest in systems that manipulate light by fluidic means and conversely, utilize light to manipulate the geometry or optical properties of fluids. Controlling liquids via illumination has several advantages over more common electrically or mechanically driven pumping schemes. First, optical actuation is 'non-contact' in that it requires no electrical or pneumatic connections to the outside lab. Second, due to the high frequency of the radiation used, optical methods are agnostic about the electrical conductivity, pH, and ionic character of the fluids under study. Third, since it is possible to focus a beam of light in a small spot, optical actuation can be applied locally without the high resolution patterning and multi step fabrication required by many other methods.

Much of the research to date has surrounded optical tweezing: the manipulation of material with a refractive index different than its fluid surroundings by illuminating it with a tightly focused laser beam. First described for a single particle by Ashkin et al. [1], tweezing techniques have become quite mature, with the demonstration of multiple independent optical traps created via interference or real time computer generated holograms [2, 3, 4], manipulation via guided waves [], and optical rotation and

pumping driven by beams with angular momentum [5]. However, all of these methods are dependent on having suspensions or mixtures of materials whose refractive indices differ.

Other researchers have focused on using the thermal energy of absorbed light to drive mechanical motion. Kotz et al. have demonstrated the actuation of an oil droplet in liquid surroundings via thermocapillary forces driven by a laser beam [6]. This same effect has been used to manipulate droplets on a surface [7, 8]. Liu et al. have demonstrated fluidic actuation in a microchannel via the photothermal heating of suspended plasmonic particles [9]. In this method, focused laser illumination of the suspension near the free liquid-air surface causes heating and evaporation, and the subsequent condensation near the contact line causes forward wetting. By scanning the laser beam, the liquid can be drawn through the channel.

The method developed in our experiments uses a similar laser powered, photothermal heating of metallic particles to actuate fluids in microchannels. Unlike Liu's method, in our scheme the absorbers are fixed to the substrate ; consequently the energy absorption of our method is constant, rather than varying with the concentration of suspended particles. This allows us to maintain a well controlled, near-ambient temperature in the fluid during the process, and allows for the creation of stable air bubbles in the microchannel. We will demonstrate how these bubbles are utilized to act as a pump that is driven by energy absorbed from a stationary laser spot. The system described achieves interphase mass transfer at near-ambient temperature and pressure and has negligible loss of the transported material, making it attractive for sensitive applications such as biochemical analysis.

4.1 Interphase Mass Transfer

A bubble is an example of a phase boundary, a delineation between the strongly interacting molecules of the liquid phase and a gas or vapor. This sort of phase boundary is dynamic, with energetic molecules constantly leaving the liquid state and others spontaneously condensing back to the liquid surface [10]. In a bubble at equilibrium, the mass lost to the volitalization of the liquid phase is balanced by the mass of condensation. Interphase mass transport within a liquid enclosure can occur as fluid from a warmer portion of the interface is vaporized and then condensed on a cooler portion [11]. This type of mass flow in nucleated vapor bubbles has been used to describe the enhanced heat transfer from the heated solid surface to the liquid during boiling [12]. Clearly, the high temperatures required to form and maintain a bubble of vapor are prohibitive for temperature sensitive systems. However, in principle the mass transfer is not limited to a *vapor* bubble but can be applied to an ambient temperature gas bubble as well.

A static air bubble in a microchannel is a more convenient venue in which to study thermally driven vapor transport, since this sort of bubble can support interphase-mass transfer with only a slight temperature imbalance between its surfaces. Unlike a vapor bubble, a gas bubble bounded by the walls of a microfluidic channel provides stable liquid-vapor interfaces without the need for heat input to form and maintain the phase separation. At equilibrium there is no net mass-transfer between the liquid and vapor phases. However, by adding a small heat flux near a liquid-vapor interface, mass-transport can occur in the same manner as with a vapor bubble. Maintaining a small distance between the opposite liquid-vapor interfaces allows the vapor to be completely recondensed at the opposite interface. We refer to this process as bubble assisted interphase mass-transfer (BAIM).

It is sufficient to apply heat only near the liquid-vapor interface of the bubble to

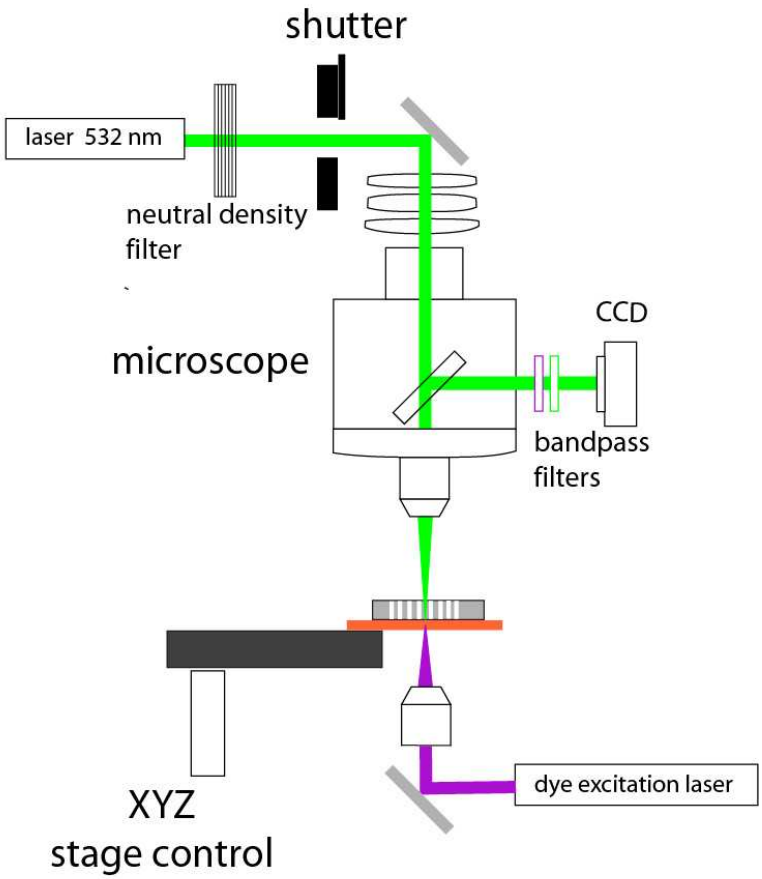

Figure 4.1: Experimental setup for photothermal activation.

drive the BAIM process. Unlike boiling, evaporation is a surface phenomena, and microfluidics is naturally suited for accessing the liquid in the immediate vicinity of a free surface of a bubble. Heating near the liquid-vapor interface causes a portion of the thermal energy to go directly into the latent heat of vaporization. In our experiments, a low power, stationary, focused laser beam provides the energy that powers the BAIM process.

4.2 Experiment

The experimental setup is shown in figure 4.1. It consists of a microscope operated in reflection mode, with laser light coupled down the camera column. The illuminating laser was a diode pumped solid state module operating at a wavelength of 532 nm. Observations of the channel were made with a color CCD (Sony F-3103) through the eyepiece. Both white light for general illumination and the 532 nm laser beam (maximum power $\sim$ 14 mW) were focused onto the substrate using the same 10X microscope objective. The reflected laser power was also measured from the other eyepiece port using a Newport 1835C power meter. The sample was mounted on a computer controlled XYZ stage (Newport ESP300 3-axis motion controller). The sample was mounted inverted, so that the laser light passed through the glass substrate rather than the PDMS microfluidic chip. This served to minimize the aberration of the focused laser spot, as well as to keep the fluid supply tubes clear of the microscope objective lens. The dye excitation source was only used for the fluorescence monitoring experiments described below, and was either a 405 nm laser diode, or a 632.8 nm He-Ne laser tube, depending on the dye being used.

A side view schematic of the microchannel system is illustrated in Figure 4.2. The device consists of a microfluidic channel which has a quasi-ordered array of gold nanoparticles that are incorporated into the base, and a captive air bubble. A laser near the plasmon resonant frequency of the nanoparticle array is focused near the edge of the gas bubble, either through the microchannel or the substrate, on the particles which causes them to be heated. The heat from the nanoparticles is transferred to the surrounding fluid, causing evaporation from the surface nearest the laser spot and subsequent condensation on the far surface of the bubble. In all figures, the fluid resevoir is on the left side of the air bubble.

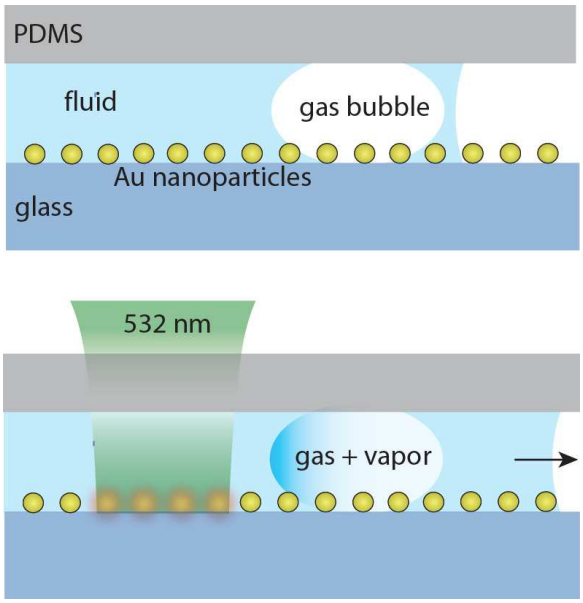

Figure 4.2: Schematic of the microchannel assembly (side view).

4.2.1 Device Fabrication

The gold nanoparticle coated substrates were created using block-copolymer (BCP) lithography. A mixture of 25.4 mg of the diblock copolymer [polystyrene$_{81,000}$-*block*-poly(2-vinylpyridine)$_{14,200}$ (Polymer Source, Inc.) and 5 ml of toluene was stirred in a nitrogen purged and dark environment and stirred overnight, 8 mg of $HAuCl_4 \cdot H_2O$ were added, and this solution was stirred for 90 hours. The resulting solution was bright yellow and transparent, and was kept out of direct light to avoid photo-oxidation. The BCP lithography method is a simple and flexible method to coat various types of substrates. The solution can be applied by either dip or spin coating. We have used spin coating to created arrays of gold nanoparticles with good uniformity on glass, quartz, silicon, sapphire, and polyacrylic. We coated plates of up to 2500 cm^2 in area, with excellent uniformity of the optical absorption across the entire surface.

To create the nanoparticle arrays used in most of the experiments, the BCP solution was spun onto a 25 mm square microscope slide at 3 krpm for 45 s. The substrates

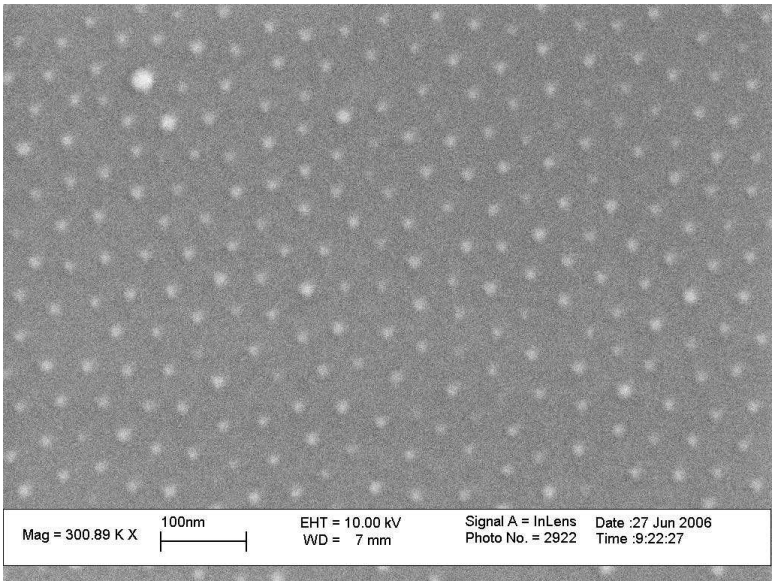

Figure 4.3: SEM image of BCPL array

were placed in an oxygen plasma for 10 minutes at 75 W (March Plasmod, 150 W maximum power). The oxygen pressure was 250 mT. Upon removal from the plasma, the glass substrates appear faintly rose to purple in color due to the absorption of the gold nanoparticles.

We have observed that when the plasma etching process is conducted at lower powers, the characteristic rose color is not appear immediately after etching. Baking the sample for a 30 minutes at 100 °C is sufficient to bring out the color. We hypothesize that a small amount of heat is needed to complete the reduction of gold from metastable gold oxide which is produced by ashing the polymer host material. An SEM image of a typical nanoparticle array is shown in figure 4.3. The average particle diameter was 14.5 nm with an average spacing of 46 nm (see figure 4.5). The optical transmission (figure 4.4) shows the characteristic plasmon resonance shape of gold spheres, with a peak due to the resonance near 540 nm.

The substrates were paced in a sealed container with a small amount of hydrodimethyl siloxane primer(HDMS 100%) to create a hydrophobic surface and promote bonding with the microchannels. Fluidic channels were formed using soft lithography

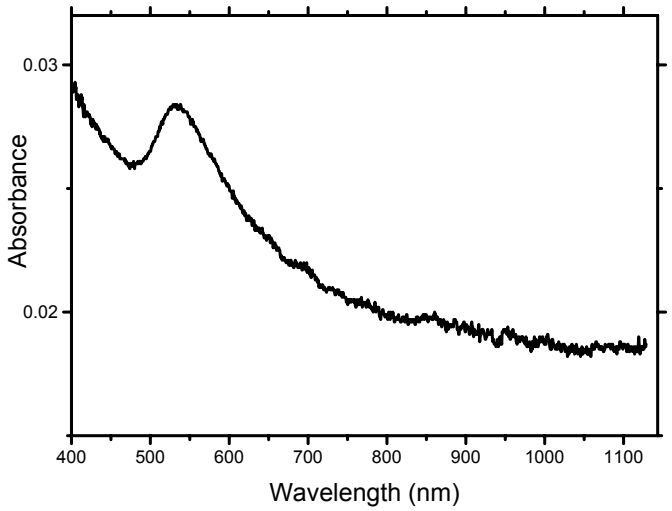

Figure 4.4: Optical transmission of BCPL gold layer on glass microscope slide

techniques by casting of PDMS (10:1 GE-RTV 615 A:B) [13]. Replica molds were created through contact lithography of a positive photoresist (SPR 220-7, Michrochem). The fabricated channels had width of 30 μm. and measured height of 5 μm as measured by profilometer. A length scale was included next to the channel to aid in the measurement of liquid displacement. The scale consists of hash marks 20 μm wide, separated by a center to center distance of 40 μm. A further revision to the chip design incorporates a simple binary label to unambiguously identify each decade of the scale. The PDMS channels were peeled away from the molds after curing for 30 minutes at 80 °C. The PDMS chips were washed in ethanol and their surfaces were cleaned using cellophane tape (Scotch brand). Chips were placed in contact with the prepared substrates and examined for blockages, air bubbles, or other imperfections under 100X magnification. Chips with clean, unblocked channels were baked for at least 4 hours at 80 °C to form a strong reversible bond between the PDMS and the substrate.

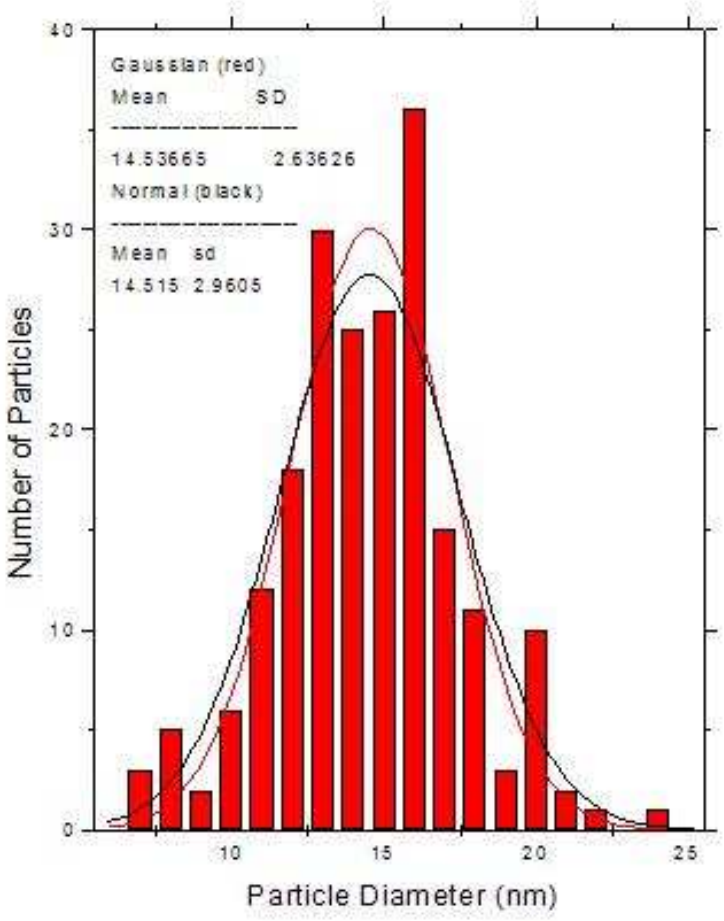

Figure 4.5: Typical size distribution of BCPL arrays used for BAIM

4.2.2 Air Bubble Formation

Fluid was injected into the microchannels using a syringe and a length of Tygon tubing (Cole-Palmer ID 0.092 inches). Channels were partially filled so the air-liquid interface was near the center of the device, around 5 mm away from the supply reservoir. Unless otherwise noted, de-ionized water was used exclusively as the working fluid. A 532 nm laser, which is close to plasmon resonance peak of the gold nanoparticle array, was focused through the glass substrate onto the nanoparticle layer. The power at the sample was 14 mW and the diameter of the beam spot was ¿ 10 μm. The position of the sample with respect to the beam spot was controlled manually, using the joystick connected to the XYZ stage.

Air bubbles were formed in the liquid by trapping air in the partially filled channel. To do this, we placed the laser spot near the free surface of the liquid, causing evaporation and recondensation on the channel walls 10–30 μm away. The droplets grew together to form a continuous liquid plug, trapping an air bubble with a width of 10–20 μm between the original free surface and the plug. This process is illustrated in Figure 4.6(a)–4.6(f). In these photos, a liquid plug is introduced by evaporation and condensation into the air gap between the column of liquid connected to the reservoir on the left hand side (with food dye added for easy identification), and a previously created plug on the right hand side. This configuration was chosen to aid in the identification of the liquid and air regions in these figures, but the air bubble could proceed in the same manner without the presence of the second liquid region at the extreme right. It should be noted that the mass transfer process we have described does not require bubbles be captured in this manner; in principle, gas bubbles could be injected into the channel, or produced electrochemically [14].

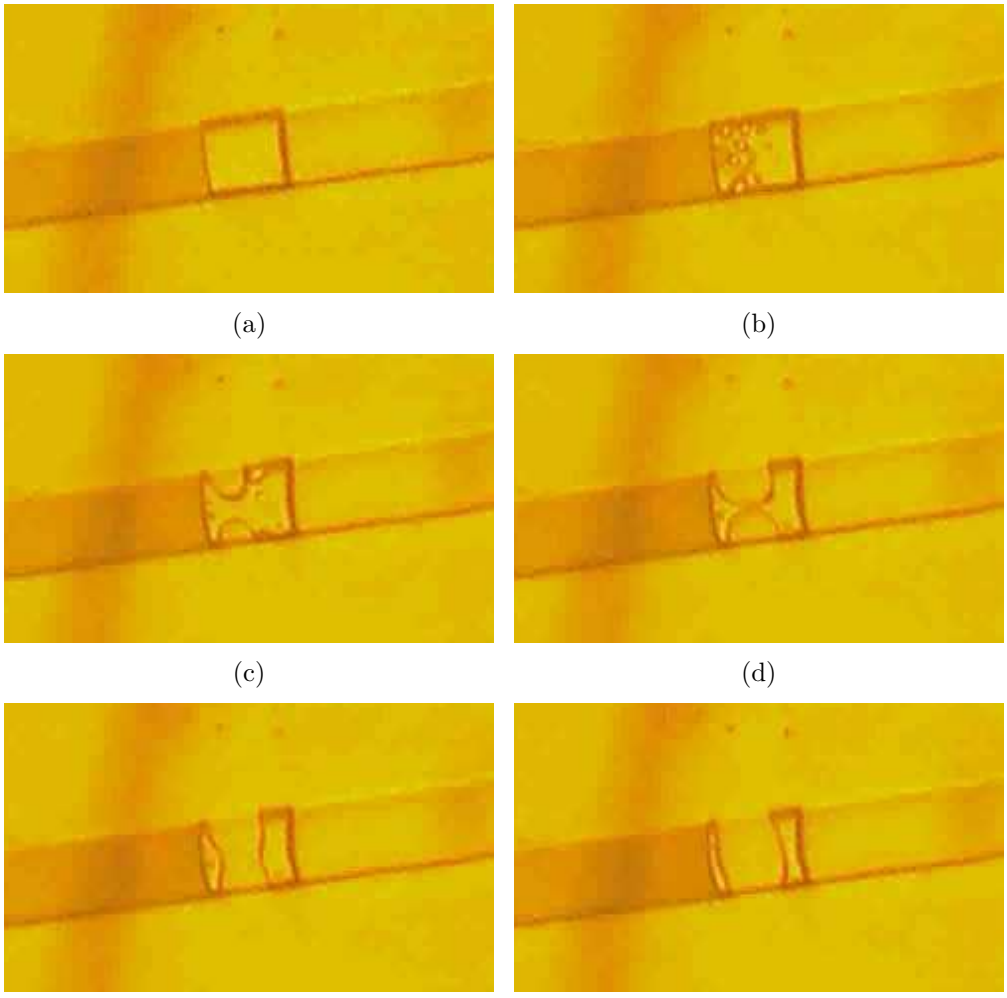

(a) (b)

(c) (d)

(e) (f)

Figure 4.6: Formation of a bubble in a microchannel

4.3 Results and Discussion

4.3.1 Optically Driven Pumping

Placing the laser several microns behind the captive air bubble allowed steady mass-transfer across the bubble, increasing the volume of fluid on the opposite side. The process is illustrated in Figure 4.7. This 'pumping' action can be continued indefinitely, as liquid from the supply reservoir will replace the vapor that passes through the bubble. We did not observe the pumping action stall even when the column of pumped fluid was several millimeters in length. It should be noted that the bubble center position remains approximately stationary throughout this process. However, the shape and curvature of the bubble evolves as the pumping progresses. As the column of pumped fluid becomes longer, the bubble pressurizes to overcome the increasing friction of the moving liquid in the channel. Since PDMS is a gas permeable material, pressurizing the bubble causes some uptake of gas into the microchannel wall. In our experiments, we observe that the initial shrinkage of the bubble can be significant, but after a period of around 10-15 s, the bubble size will be reduced to a stable state that remains nearly constant for the entire duration of pumping.

The BAIM process as realized in this configuration can only effectively provide one-way fluid transported. The mass that flows across the bubble must be replaced by liquid from the resevoir in order for the boundaries of the air bubble to remain fixed. If we heat an isolated liquid plug with the laser beam, evaporation occurs but is accompanied by a shrinking of the plug, since there is not a flow from the resevior that can replace the lost mass. In this case, both free surfaces of the liquid plug retract toward its center. The evaporated liquid recondenses as smaller droplets or plugs several microns from the original, which to not rejoin the isolated plug. However, there is no reason that liquid can not be steadily recirculated in either direction by creating a microchannel that is a closed liquid filled loop, containing a pinned air

Channel width $\bar{v}$ (μm)	$\sigma(\bar{v})$ (μm s^{-1})	v_{max} (μm s^{-1})	J (μm s^{-1})	J (x10^{-13}kg/s)
20	3.32	1.46	5.11	3.3
30	1.97	0.53	2.73	3.0
40	2.76	2.14	3.45	5.5

Table 4.1: A summary of the values of the mean free-surface velocity $\bar{v}$, the standard deviation of the mean free-surface velocity $\sigma(\bar{v})$, the maximum velocity v_{max}, and the average mass flow rate $\bar{J}$, for 20, 30, and 40 μm channels, as measured during BAIM pumping.

bubble. Indeed, this type of system is conceptually similar to the sealed heat pipes that have been used as cooling systems for decades [15][16].

We examined the mass-transfer rate of the liquid by digitizing images of the channel using a the video camera. In particular, the position of the 'free-surface', i.e. the leading interface of the fluid column, which is to the far right of the bubble in Figure 4.2, was determined using an edge detection algorithm implemented in Matlab. Plots of the measured free-surface position against time were fit using linear regression to determine the pumping speed as in figure 4.8. In this case, the first 3 data points are removed from the regression to account for the initial evolution of the bubble size. For a given channel dimension, the rate of mass-transfer J can be calculated from the fit of the pumping speed. Once the bubble has reached a steady state, the pumping rate remains constant, which is evident from agreement of the linear fit applied to the data in figure 4.8.

Pumping was tested in channels with widths of 20,30, and 40 microns, to compare the effect of channel size on the mass transfer rate. Table 4.1 summarizes the results. The high degree of variance in the data is due to the fact that the rate of flow is dependent on the precise position of the laser spot with respect to the fluid-air interface.

To control for the effects of the variable position of the beam spot between trials in the pumping studies, we examined the change in flow rate due to changes in input

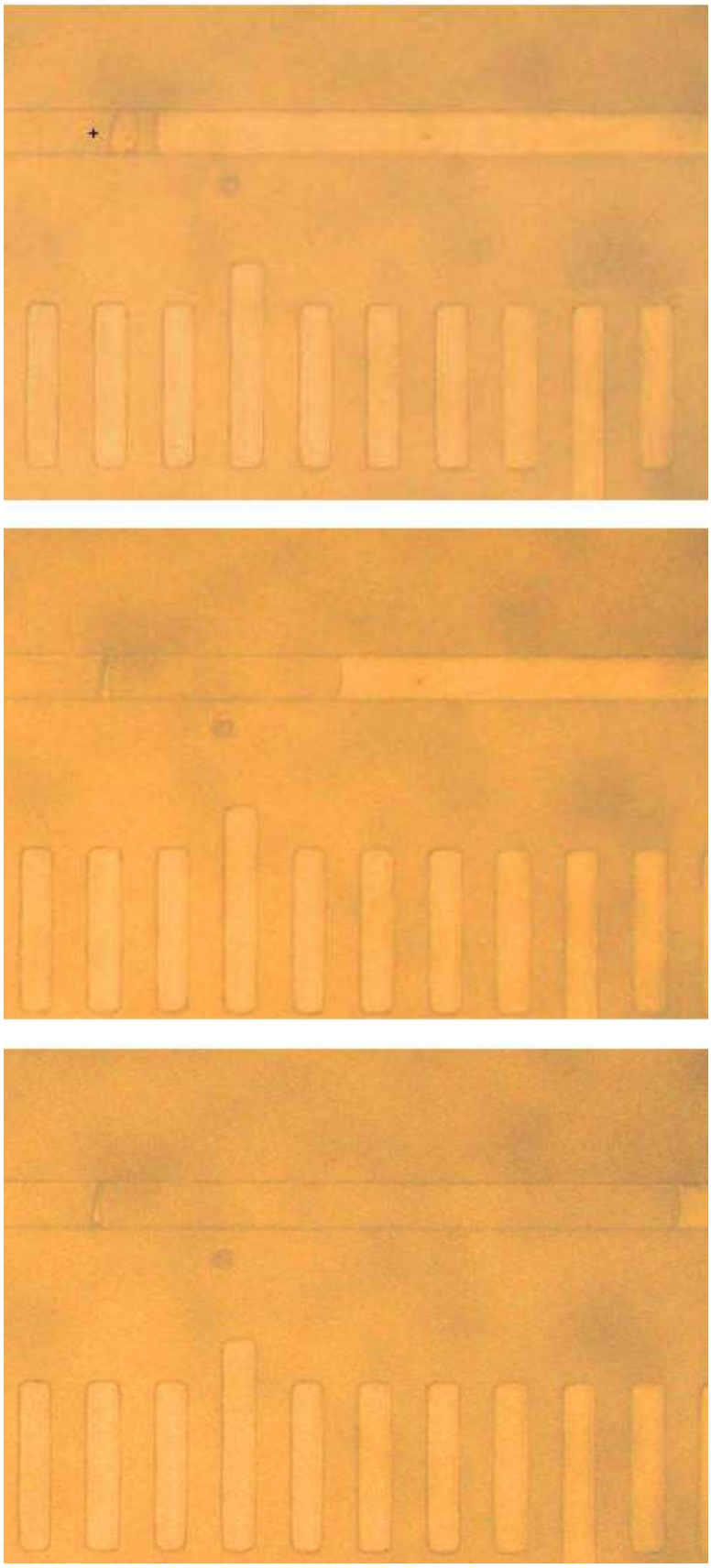

Figure 4.7: Pumping action driven by the BAIM process. The + indicates the position of the laser spot. The hash marks are seperated by 40 μm center to center.

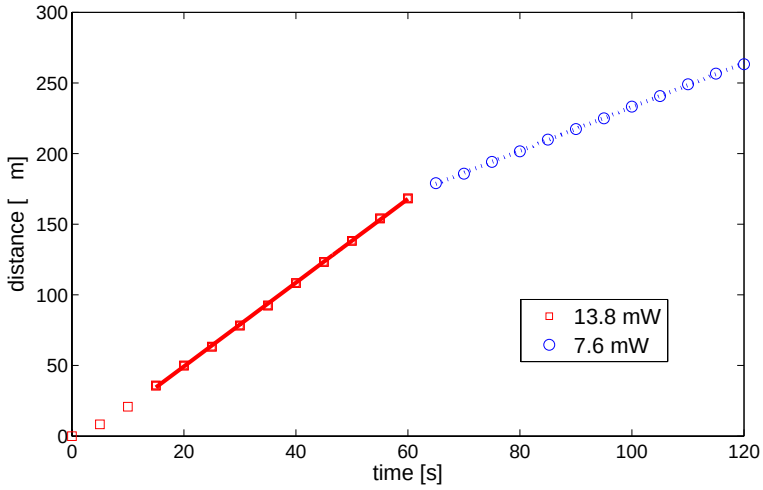

Figure 4.8: Position of liquid-air interface during BAIM pumping. The two linear regions correspond to operation at 13.8 and 7.6 mW respectively, showing that pumping occurs at a constant rate proprtional to applied laser power

power for a constant beam location. After forming a stable bubble, the laser was switched off, and the beam position was adjusted to be approximately 10 μm behind the air bubble, on the fluid filled channel. We applied the laser at full power for 1 minute and then introduced a neutral density filter without stopping the laser. We allowed the flow to proceed for another minute at the reduced power. This allows the direct comparison of pumping rate at two different power levels. The results of these experiments are summarized in table 4.2.

The measured value of J for a 30 x 5 μm channel is 4x10^{-4} g/(cm^{2}s). Following Plesset [17], the mass transfer between two, enclosed flat surfaces of water at different temperatures can be expressed as

$$J = \alpha {\rho_0}^e \sqrt{\frac{RT_0}{2\pi M}} \frac{1 - (\rho_1^e/\rho_0^e)(T_1/T_0)}{1 + \sqrt{(T_1/T_0)}}, \tag{4.1}$$

where J (g/cm^2 s) is the mass flow rate, α is the evaporation coefficient,[18] M (Kg/mol) is the molecular weight of the vapor, ${\rho_0}^e$ (Pa) is the saturation vapor density at T_0 (K), the warmer interface, ρ_1^e is the saturation vapor density at T_1, the cooler

OD	I_x/I_0	v_x/v_0	95% interval
0.1	0.727	0.664	(0.625,0.703)
0.1	0.727	0.612	(0.589,0.635)
0.1	0.727	0.639	(0.560,0.722)
0.2	0.546	0.375	(0.228,0.530)
0.2	0.546	0.524	(0.510,0.538)
0.3	0.407	0.360	(0.350,0.368)
0.3	0.407	0.394	(0.375,0.412)

Table 4.2: A summary of the parameters and measured pumping values for a 30 μm channel. The first column is the absorbance of the optical density (OD) filter. The second column is the calculated relative change in laser intensity I_x/I_0. The third column is the measured change in the relative velocity of the free surface v_x/v_0. The fourth column is the 95% confidence interval for the measured velocities.

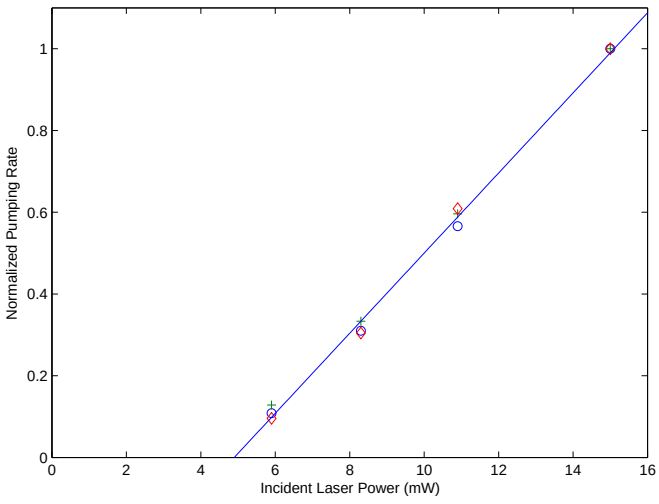

Figure 4.9: Linear relationship between normalized pumping rate and applied laser power

interface, and R (J/K/mol) is the universal gas constant. From this equation we see that the experimentally measured value of J is comparable to having the two surfaces of water at T_0 and $T_1 = 25.0$ and $25.5\,^{\circ}\mathrm{C}$, respectively, which assumes corresponding values of ${\rho_0}^e$ and ${\rho_1}^e$ at these temperatures.

The exact rate of mass flow is dependent not only on the optical power applied to the channel, but also on the distance of the focused spot from the contact line. We measured the pumping rate as a function of the distance between the position of the laser spot and the edge of the bubble. During pumping, the laser was held stationary for 10 s, was translated away from the bubble by a $2\,\mu$m increment, and then this sequence was repeated. We note that the absolute position of the initial spot with respect to the edge of the bubble is not necessarily the same for each trial, and the flow rate for each trial has been normalized to the corresponding initial laser position. Beyond a distance of $10\,\mu$m from the initial position, the pumping rates were too slow to be accurately measured by our software. The initial laser spot was kept far enough behind the liquid-air interface to avoid disturbing it. This minimal distance varied slightly for each trial, but we found that a distance of at least $5\,\mu$m was sufficient to avoid condensation of vapor inside the air bubble, which could divide the bubble into two parts.

Shown in Figure 4.10 is a plot of the normalized BAIM pumping rates against the relative laser position for three separate trials in a $30\,\mu$m channel. The measurements show a rapid drop-off in the pumping rates as the beam is moved beyond a few microns from the initial spot. This result demonstrates that it is most efficient to apply heat only near the interface, which achieves interphase mass-transport without excessive heating the of entire fluid volume.

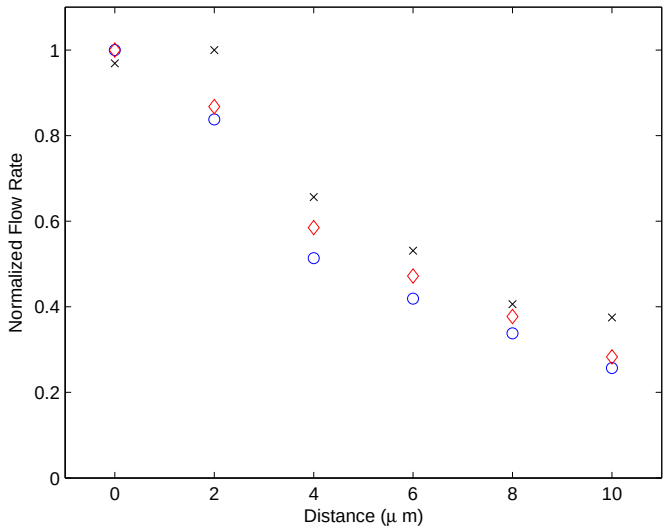

Figure 4.10: Normalized pumping rate as a function of displacement of the laser spot from its initial position

4.3.2 Temperature Measurement

We would like to optimize the energy delivery so that the mass flow as high as possible without significantly impacting the temperature of the fluid or the channel. To charcterize the heating we need a way to visualize the channel tempreature. We examined the impact of plasmonic heating of the fluid using temperature sensitive fluorescence intensity measurements [19]. The test solution was composed of 0.1 M Coumarin 4 Dye (peak emission 420 nm, Exciton Co.) in ethanol mixed with a buffer of concentrated HCL and tris (hydroxymethyl)aminomethane (Tris buffer). the Tris-HCl buffer exhibits a well known pH decrease with increasing temperature [20], The falling pH causes quenching of the fluorescence of the dye so that the measured intensity is a effective probe of the temperature of the solution.

We calibrated the effect by measuring the fluorescence intensity of the solution in a cuvette with 1 cm path length. A violet laser (405 nm Nichia diode, 5 mW maximum power) was used as a the excitation source, and a 420 nm narrow bandpass filter (Semrock Co.) was placed before the power detector to isolate the fluorescent

signal. The cuvette was mounted atop a Peltier cooler which could be run either as a heating or cooling stage, and the solution temperature was monitored with a K-type thermocouple.

First we held the cuvette at room temperature and added concentrated Tris buffer dropwise to determine the maximum intensity change with changing pH. We then heated the solution to 55 °C and cooled it back down to 22 °C while monitoring its fluorescence. The fluorescence intensity was very linear across this range. Photobleaching over the time of the experiment (> 10 minutes) was not observed.

The test solution was introduced into the microchannel to study laser heating of the liquid surrounding the gold nanoparticles. The dye was excited from below using 405 nm laser focused by system of lenses to an area with a diameter of 100 microns. In order to measure the spatial distribution of the temperature field, we imaged the channel with the CCD as in the earlier pumping experiments, with the addition of the band pass filter which effectively blocked the both the 405 and 532 nm lasers. We first examined the heating inside the fluid column away from the free surface. Images were captured with an integration time of 15 s. An initial image was captured without heating, then subsequent frames were captured with the laser turned on. The intensity change from the initial frame was determined by image subtraction. No significant intensity change was observed throughout the fluid volume. When the experiment was repeated with the laser spot focused at the free surface, the surface itself wet forward in the manner described by Liu et al. [9], but no change in the temperature of the liquid was detected.

Based on the calibrated response of the dye solution, we should expect an intensity change of around 0.5% for a temperature rise of 1 degree. Given the signal to noise ratio of the digitized fluorescence image, we estimate the detectable limit for ΔT to be 2 °C. However, this value reflects the average temperature across the depth of the microchannel rather than the local surface temperature of the absorber. It

is also important to have a sense of the temperature at the nanometer scale near the substrate surface. A high temperature, even just at the surface of an absorbing nanoparticle, may cause problems for sensitive applications: denaturing protein, melting paired DNA strands, or decomposing delicate organic chemicals. The steady state temperature of a nanoparticle is impacted by its absorption, the incident power applied, and the mechanics of the heat transfer to it surroundings. Following the approach of Pustovalov, [21] the temperature of a spherical particle due to a power density I_0 in steady-state conditions can be shown to be:

$$T_0 = T_\infty + \frac{I_0 K_{abs} r_0}{4k_\infty}, \tag{4.2}$$

where K_{abs} is the efficiency absorption factor, which can be calculated from Mie scattering theory, for a particle of radius r_0 and k_∞ is the coefficient of thermal conductivity of the surrounding medium at the macroscopic equilibrium temperature T_∞. Due to nanoscale effects that limit the heat transfer from a nanoparticle to a solid, [22, 23] we assume that most of the heat generated by the plasmon heating in the nanoparticles is transferred to the surrounding fluid. We set, I_0 = 2 x 10^8 W/m^2, r_0 = 7.5 nm, k_∞ to be 0.61 W/m/K, and we use a value K_{abs} = 1.5.[24] From Equation 4.2, the rise in the temperature of a nanoparticle T_0-T_∞ is $\sim$ 1 °C. We note that these numbers are all approximate and are presented to demonstrate that results of this order are quite possible.

The efficiency of the mass transfer can be increased by reducing the loss of the thermal energy to the substrate. The heat conduction of the device can be understood by applying an analogous electrical resistance model. Consider the absorption of laser energy by the nanoparticles as a thermal current source. This thermal current is divided into two branches, the thermal energy that powers the evaporative mass transport, and heat that is lost by conduction to the chip and surrounding environ-

ment. Lowering the thermal conductivity of the substrate causes more energy to flow across the bubble in the form of vapor, just as increasing the resistance of one of two parallel electrical resistors will cause more current to flow through the other branch of the circuit. We tested the impact of heat conductivity of the substrate by fabricating identical channels on glass, acrylic and sapphire substrates. When the glass support was replaced with acrylic, which has a lower value of thermal conductivity by approximately a factor of eight, that the flow rate increased from 4 to 7 μ/s in a 30 μm channel. On the sapphire substrate, which has a higher thermal conductivity than glass by an order of magnitude, we observed no measurable mass flow due to BAIM. The heat loss to the sapphire substrate was so great that whatever energy remained was not enough to increase the evaporation from the liquid-air interface significantly.

4.4 Chemical Separations

In addition to pumping, bubble assisted interphase mass transfer provides a means of chemical separation. Separations involving phase changes are widely used in a multitude of chemical, biological, and material syntheses. In distillation, for example, the vapor phase can be achieved by heating the liquid, or in the case of temperature sensitive systems, by placing the liquid under vacuum. However, either method of volatilization may not be acceptable in systems that are both temperature sensitive and require the presence of dissolved gases. Furthermore, efficient collection of the vapor requires active cooling to inhibit evaporation of volatile components from small droplets [25]. The mechanism of vapor transport across the trapped bubble allows the BAIM method to simply separate volatile from nonvolatile components. Since the two interfaces are not in contact, there is no seepage of dissolved or suspended material in the liquid phase across the bubble.

4.4.1 Concentration by Distillation

In situations where a low volatility analyte of interest is present in low concentration, controlled evaporation of the solvent can be used to increase the local concentration of the analyte and aid detection. Using the dye solution described above, we demonstrate that BAIM offers a means for this sort of simple distillation. By focusing the laser 10 microns behind the initial liquid air interface, solvent is transfered across the bubble and the the local concentration of dye is increased. Figure 4.11(a) is a white light image of the channel, and Figure 4.11(b) is a fluorescent image of the same region before distillation. As the laser drove the vapor transport across the bubble, an increase in the fluorescence intensity within the distilland was measured while no fluorescence was observed in the distillate, Figure 4.11(c). Shown in Figure 4.11(d) is a plot of the change in fluorescence intensity $\Delta I/I_0$ in the distilland with time during distillation, where I_0 is the intensity at t=0 s. An increase by 25% after 45 s of pumping is observed. Although the exact composition of the distillate has not been determined, it can be clearly seen that very little if any of the dye molecule is present. The increase in the fluorescent intensity is consistent with the removal of ethanol: as fluid leaves the interface it leaves behind the dissolved dye molecule, and is replaced by dye carrying solution from the reservoir, creating a local concentration gradient of dye. Due to the change in the composition of the distilland during the seperation, it is possible the intensity of the dye fluorescence might be impacted by the pH quenching effect. Since the HCl is volatile and the Tris is not, removal of HCl will be accompanied by the aggregation of Tris. However, the large change in fluorescence intensity (25%) is inconsistent with the small quenching effect we observed due to temperature driven pH changes in the earlier experiements. For the flourescence increase seen in this experiment to be attributable to the an increase in pH would require a much more efficient concentration of the Tris base than is feasible. The measured intensity signal is therefore likely to accurately represent or

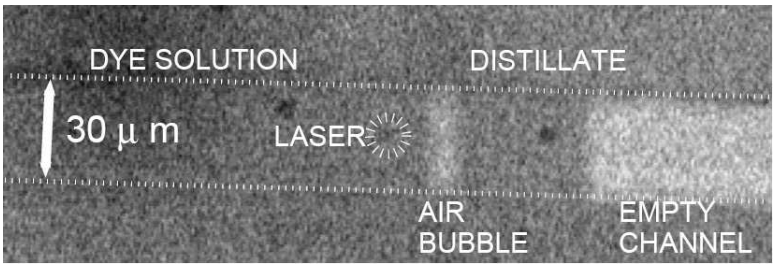

(a)

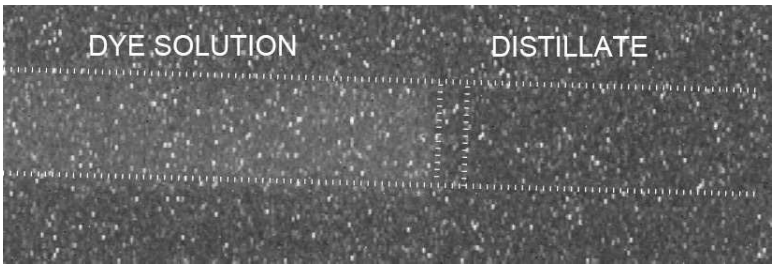

(b)

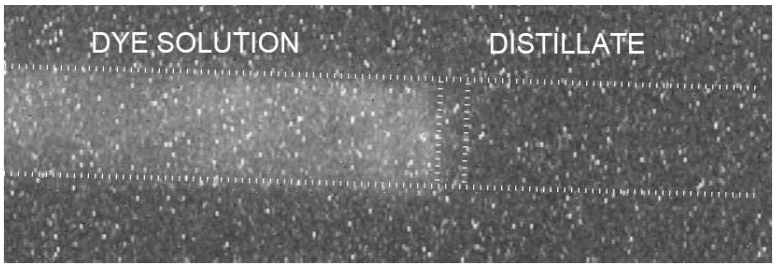

(c)

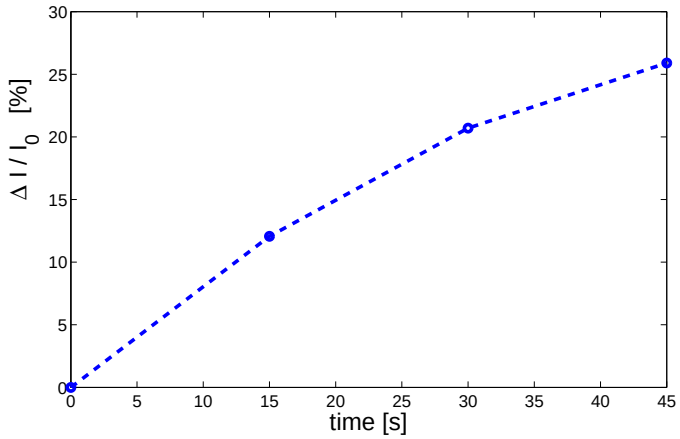

(d)

Figure 4.11: A BAIM distillation. (a) A white light image of the channel containing dye solution. (b) The initial dye fluorescence image of this same region. (c) Fluorescence after 45 s of laser induced evaporation. (d) The percentage increase in the mean fluorescent intensity $\Delta I/I_0$ of the distilland with time during distillation.

under represent the change in dye concentration.

We have applied the same technique to perform preconcentration of DNA oligos, which is an application of present research interest in biochemistry [26]. Solutions of oligomer were prepared from a lyophilized sample provided by Alpha DNA Inc. The supplied oligomers were 20 bases long, and were prepared with a 5' modification of APC Cy5.5 dye (Glen Research). A concentrated stock solution was prepared by suspending the lyophilized DNA in TE buffer (pH 8.0). A working solution was prepared from the stock solution by addition of an annealing buffer (pH 8.0) to a final concentration of 160 nM. The working solution was injected in to a 30 μm wide microchannel. The fluorescence excitation source was a multimode He-Ne laser passed through a 633 nm bandpass filter (Edmund Optics). The power of the laser after the filter was measured at 10.7 mW. The laser spot was brought from beneath the sample directly onto the microchannel. The excitation flux through the channel was approximately 1x10^6 W/m^2.

Fluorescence measurements were performed by imaging the channel through a microscope with a 10x objective, using a monochrome video camera (Sony XC-710). A long pass wavelength filter was inserted into the optical system before the camera to reduce the excitation light recorded (685 nm cutoff filter, Melles Griot). To avoid excessive photobleaching, fluorescence images were captured both prior to and immediately after the evaporation process only. An air bubble was formed using the 532 nm laser in the usual manner, and a small quantity of liquid was transported across the bubble (50 μm). An initial image was captured before further evaporative transport was performed, using an exposure time of 2 s. The shutter for the excitation light was opened during exposure, and then closed while evaporative transport was resumed to minimize bleaching. The evaporative transport was performed for 5 minutes, after which the 532 nm laser was shuttered and another fluorescence exposure was captured. The fluorescence images were again analyzed using image subtraction. There

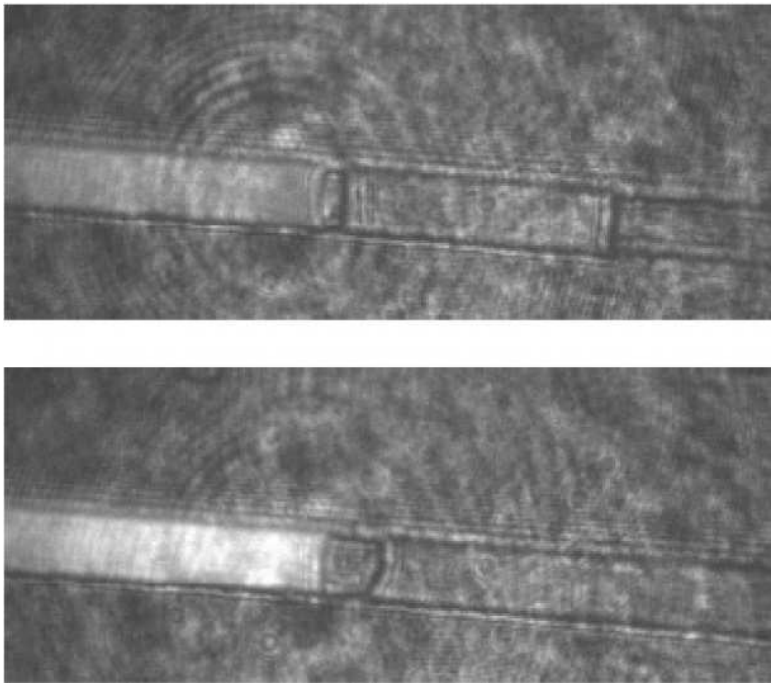

Figure 4.12: Cy5.5 fluorescence of oligonucleotides in a microchannel before and after concentration by BAIM

is a 4.3x increase in the dye observed dye fluorescence over a period of 5 minutes.

Concentration by BAIM is also applicable to suspended solid nano- or microparticles. Figures 4.13(a)–4.13(d) show the bubble aided concentration of 2 micron polystyrene beads (Molecular Probes Inc.). The suspension of polystyrene beads were diluted by a factor of 10000 from their concentration as supplied in distilled water and used as the working fluid for the BAIM process. The beads aggregate near the contact line due to the evaporation. This effect is a clear example of the so called "coffee cup" effect, where suspended material is concentrated near the pinned contact line of a fluid with a free surface [27].

4.4.2 Chemical Purification

We have also investigated using BAIM distillation to purify by separating and recovering a more volatile component from a liquid mixture. We examined a classic distillation problem, separation and concentration of highly purified ethanol from an

(a)

(b)

(c)

(d)

Figure 4.13: BAIM concentration of a suspension of 2 micron PS spheres by evaporation. t =(a) 0 s, (b)14 s, (c)23 s, (d)38 s

ethanol-water mixture. In order to characterize the liquid in the microchannel, we measured its conductivity in situ. The essence of the technique is to use a slug of liquid to bridge a gap between two electrodes. The liquid slug acts a shunt resistance that influences the transient current that is measured when a potential is applied to the electrodes. We can measure the resistance by observing the current through the device due to an applied voltage.

The measurements were conducted on chip using two electrodes fabricated from an indium-tin oxide(ITO) coating. The fabrication process began with an ITO coated microscope slide with a resistance of 70-100 $\Omega/\square$. The two pads are defined lithographically using a positive photoresist (Shipley 1813, Microchem co.). Exposed ITO was etched away using a mixture of de-ionized water, hydrochloric acid and nitric acid for 5 minutes at room temperature. The space between the electrodes is 20 μm wide, and the electrode has a length of 2 cm. These two electrodes form a planar capacitor. The photoresist was removed by stripping with warm acetone, after which the substrate was tested using a digital multimeter to ensure there were no bridging faults short circuiting the two electrodes.

The substrate was processed as before to deposit the plasmonic nanoparticle layer. A PDMS microchannel was bonded to the chip so that the fluidic channel was perpendicular to the electrodes, crossing the gap between them. Each electrode was contacted using 30 gauge wire wrap wire soldered to the ITO pad using 99.99% indium as a solder. The complex impedence of the sample was equivalent to a capacitance of 28.8 pf.

To perform the experiment, we connected the device to a Keithly 617 electrometer to measure the current for different substances that bridge the electrode gap. The electrometer has a built in voltage source for measuring I/V curves, and this was used to supply a DC voltage of 0.3 V. This voltage was chosen since it is low enough that there is no observed electrochemical reaction at the ITO electrodes. At voltages

about 0.7 V, we observed that the ITO was rapidly attacked at the cathode, creating a opaque white region in reflection mode. This phenomenon has been studied by other researchers, and attributed to the electrolytic production of hydrogen from water, which interacts chemically with the oxide [28]. The interaction with hydrogen causes undesirable surface roughening and degradation of the oxide conductivity.

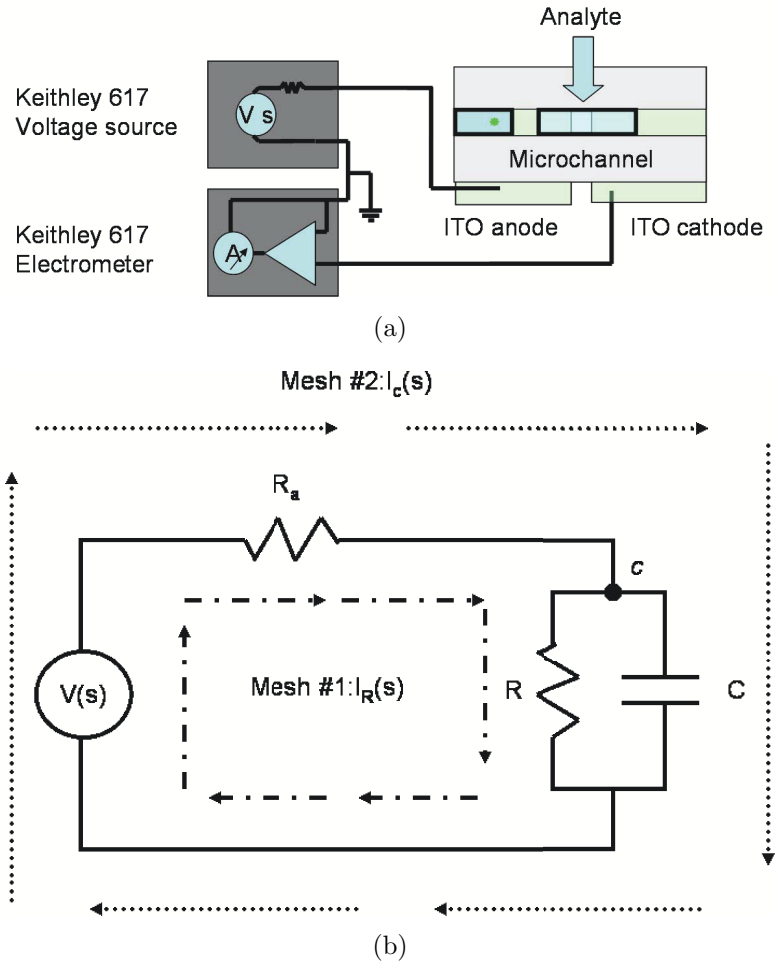

Figure 4.14: (a) Schematic of the electrical conductivity measurement setup and (b) equivalent circuit formed by the electrometer and microchannel device

The electrical measurement setup is shown in figure 4.14(a). Measurement is performed by introducing the fluid to be characterized across the electrode gap and activating the voltage source. Because the width of the microchannel is only 0.15% of the entire capacitance structure, we estimate that the change in capacitance due to

replacing the air with liquid (a low frequency dielectric constant of ≈ 80 for pure water, or ≈ 24 for pure ethanol [20]) will influence the total capacitance of the structure by less than 12 percent. Thus we make the assumption that the capacitance of the device is a constant C, regardless of the composition of the fluid analyzed. The resistance of the microchannel is proportional to the width of the gap between the electrodes, w, inversely proportional to the cross sectional area of the channel and the conductivity, g, of the fluid being analyzed, where $R = l/(w * h * g)$.

The expected behavior of the current can be determined from basic circuit analysis using the Laplace transform [29]. In the Laplace domain, the step function voltage source $V(s) = v_0/s$. By applying Ohm's law at the node c, we can derive the relation between the currents through the resistive and capacitive branches of the the circuit.

$$V_c(s) = \frac{1}{Cs} I_C(s) = R I_R(s) \tag{4.3}$$

Accounting for the voltage drops around mesh 1, we can write the following circuit equation

$$V(s) = I(s)R_a + I_R(s)R \tag{4.4}$$

where $I(s) = I_C(s) + I_R(s)$. Substitution of $I_C(s)$ for $I_R(s)$ and algebraic manipulation gives the current through the capacitor:

$$I_C(s) = \frac{v_0/R_a}{s + \Gamma}. \tag{4.5}$$

Here $\Gamma = [R_a + R]/[R_a RC]$ has units of frequency, and the inverse Laplace transform of the expression yields the time domain expression of the capacitor current

$$i_c(t) = \frac{v_0}{R_a} e^{-\Gamma t}. \tag{4.6}$$

The time domain expression of the current through the shunt resistor is simply de-

termined from the capacitor current by integration, which gives

$$i_r(t) = \frac{v_0}{R_a + R}(1 - e^{-\Gamma t}). \tag{4.7}$$

Combining the two terms gives us an expression for the ideal current through the device

$$i(t) = \frac{v_0}{R_a} e^{-\Gamma t} + \frac{v_0 R}{R_a + R}(1 - e^{-\Gamma t}). \tag{4.8}$$

Qualitatively, the shunt resistor acts as a leak across the capacitor. The resistance of the material that acts as the shunt resistance will determine the steady state. When the resistance $R >> R_a$ the exponential time constant is $\Gamma \approx 1/R_a C$ which is independent of the shunt resistance. With $R_a = 1\,\mathrm{M}\omega$, the charging time of the capacitance due to the electrodes is in the microsecond range. This is far too small for the transient nature of the current to be captured by the electrometer, which integrates with a 500 ms period. The peak current measurement observed on the electrometer is therefore is equal to $\Delta Q/\Delta V \Delta t$. ΔQ is the sum of the charge on the capacitor, CV_0, and the integral of the leakage current $i_r(t) * \Delta T$. By the same reasoning, the fast transient of the leakage current is negligible so that the contribution of the leakage current to the peak current measurement is approximately $i_r(\Delta t)$. Figure 4.15 shows the current measured from our device with an empty microchannel. In this case, the shunt resistance is an open circuit, and the measured current of 15 pA is equal to $CV_0/\Delta t$. This current corresponds to a capacitance between the electrodes of 43 pf For comparison, the current measured across the same device with a channel full of bi-distilled HPLC water is shown in figure 4.16. The current contribution due to charging of the capacitance in these two measurements is comparable, and the large signal of the water filled channel is primarily due to conduction through the shunt resistance of the water. The conductivity of the water slug is measured at 1.2 μS/cm, which is in good agreement with the nominal conductivity of 0.9 μS/cm. These two

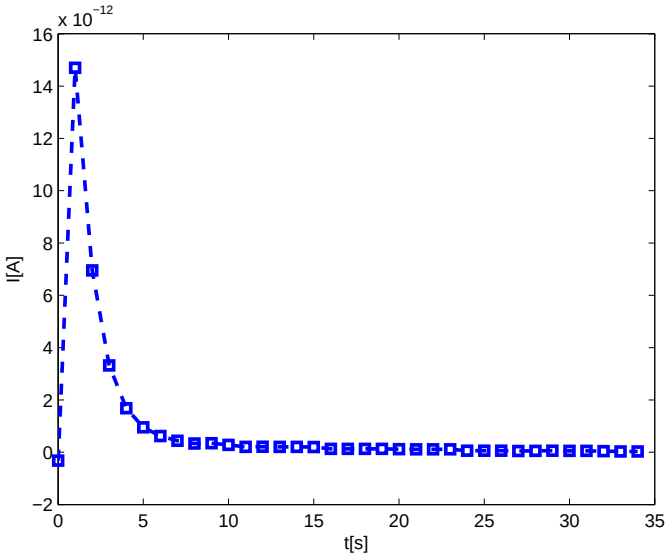

Figure 4.15: Measured current across air gap in an empty microchannel

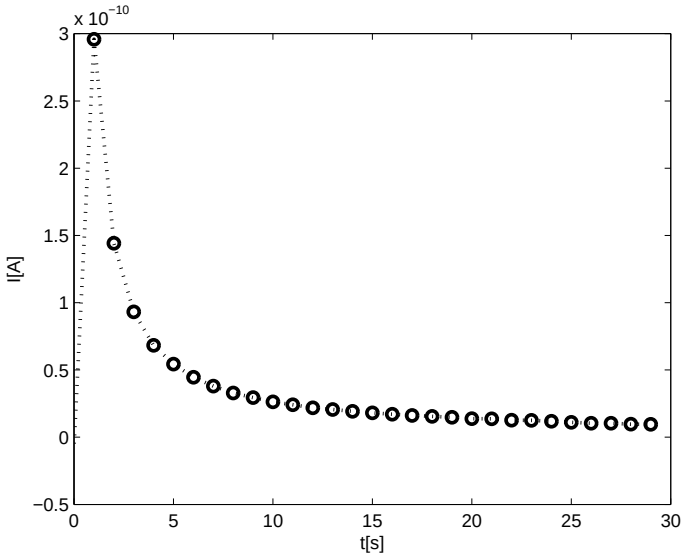

Figure 4.16: Measured current through water filled microchannel

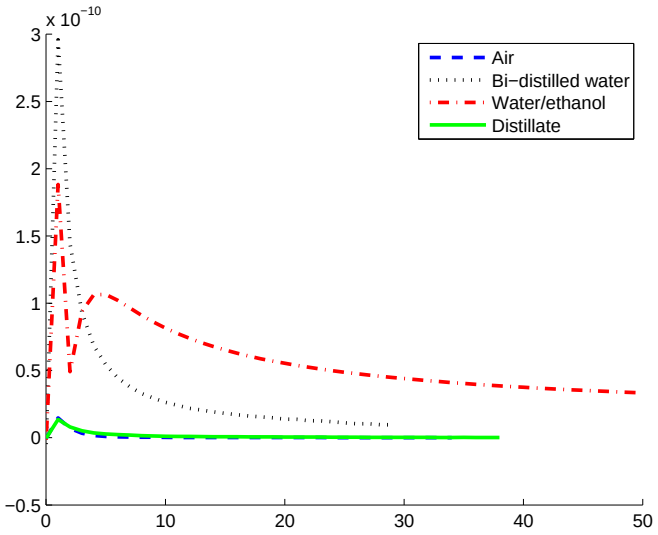

Figure 4.17: Measured currents of pure and distilled materials in microchannel

currents represent upper and lower limits of the measurements performed. A mixture of water with ethanol, which is by itself a very poor conductor of electricity, with a conductivity lower than even the purest water, should have a measured leakage current between that of the empty channel and the water filled channel.

We extracted the water from the channel and baked the device above 100 °C for an hour to vaporize any residual liquid before attempting the distillation. We performed the experiment by partially filling the channel with an ethanol water mixture (1:1 by volume) and introducing an air bubble with the laser beam approximately 100 microns from the electrode gap. The BAIM process was performed by placing the laser around 20 microns from the bubble interface, so that the liquid was condensed on the distillate slug very slowly. After approximately 1 minute, the condensed liquid slug was around 150 microns long. At this point the laser was shuttered and the voltage source activated. Figure 4.17 shows the measured current of the distillate product as compared to the both the initial ethanol-water mixture and a pure water sample. The intra-channel distillation performed by the BAIM process was able to produce a distillate with conductivity an order of magnitude smaller than either the

OD	I_x/I_0	v_x/v_0	95% interval
0.1	0.727	0.664	(0.625,0.703)
0.1	0.727	0.612	(0.589,0.635)
0.1	0.727	0.639	(0.560,0.722)
0.2	0.546	0.375	(0.228,0.530)
0.2	0.546	0.524	(0.510,0.538)
0.3	0.407	0.360	(0.350,0.368)
0.3	0.407	0.394	(0.375,0.412)

Table 4.3:

mixed sample or the pure HPLC grade water. The electrical behavior of of the distillate plug is similar to that of a very good insulator, with a measured leakage current approaching that of the air filled channel. The current measurement indicates that the product of the BAIM distillation is a mixture of water and ethanol with a higher ethanol concentration than solution it was produced from. It is well known that distillation techniques cannot be used to produce pure ethanol samples, since water and ethanol form a stable azeotrope with a concentration of around 95% ethanol by weight. However, due to the strong insulating behavior of the product, we are confident that water is present in a relatively low fraction. To determine the exact fraction of ethanol to water in the distillate would require a careful calibration of the on chip conductivity measurement with standard reference electrolyte solutions [30]. The ethanol concentration can also be determined in situ using techniques that identify chemicals by optical activity, such as observation of ethanol's characteristic Raman scattering peak at $\approx 880\,\mathrm{cm}^{-}1$ [31]. Our group is currently investigating Raman spectroscopy as an independent verification of ethanol concentration in the microchannel in order to to calibrate the on-chip conductivity measurements and provide an accurate measure of the efficiency of the BAIM distillation process.

4.5 Conclusions

In conclusion, we have demonstrated that the BAIM technique can be applied both as a fluid pump and to perform continuous flow chemical separations. BAIM assisted chemical separation allows for simple and compact purification and sample concentration that can be easily integrated with conventional soft lithographic microfluidic circuits for lab on chip applications. The three principal advantages of our technique over other separation schemes are (1) that it is applicable to systems that are sensitive to temperature and vacuum, (2) that it does not require active cooling for recovery of the vapor phase, and (3) that energy is added locally near the site of the evaporation, rather than heating the fluid in throughout the channel. Although as demonstrated here, the low mass-transfer rates may not be useful for applications that require high throughput, they are suitable for gentle product recovery from small-scale systems e.g. concentration and analysis of fragile bio-products from a single living cell. Additionally since the amount of energy required to drive the BAIM process is low, careful engineering of the materials used in fabrication may enable micro sized chemical separators that can be extremely energy efficient. There is much that remains to be done to understand and extent of heat loss to the fluid and the channel materials in order to optimize the speed and efficiency of vapor transport in these devices.

References

[1] A. Ashkin, J. M. Dziedzic, J. E. Bjorkholm, and S. Chu. Observation of a single-beam gradient force optical trap for dielectric particles. *Optics Lett.*, 11(5):288–290, 1986.

[2] R. Di Leonardo, J. Leach, H. Mushfique, J. M. Cooper, G. Ruocco, and M. J. Padgett. Multipoint holographic optical velocimetry in microfluidic systems. *Phys. Rev. Lett.*, 96(13), 2006.

[3] D. G. Grier and Y. Roichman. Holographic optical trapping. *Appl. Optics*, 45:880–887, 2006.

[4] M. Reicherter, S. Zwick, T. Haist, C. Kohler, H. Tiziani, and W. Osten. Fast digital hologram generation and adaptive force measurement in liquid-crystal-display-based holographic tweezers. *Appl. Optics*, 45(5):888–896, 2006.

[5] K. Ladavac and D. G. Grier. Microoptomechanical pumps assembled and driven by holographic optical vortex arrays. *Optics Express*, 12(6):1144–1149, 2004.

[6] K. T. Kotz, K.A. Noble, and G.W. Faris. Optical microfluidics. *App. Phys. Lett.*, 85(13):2658–2260, 2004.

[7] A. A. Darhuber and S.M. Troian. Principles of microfluidic actuation by modulation of surface stresses. *Annual Review of Fluid Mechanics*, 37:425–455, 2005.

[8] A. A. Darhuber, J.P. Valentino, S.M. Troian, and S.Wagner. Thermocapillary actuation of droplets on chemically patterned surfaces by programmable microheater arrays. *Journal oF Microelectromechanical Systems*, 12(6):873–879, 2003.

[9] G. L. Liu, J. Kim, Y. Lu, and L. P. Lee. Optofluidic control using photothermal nanoparticles. *Nat. Mat.*, 5:27–32, Jan 2006.

[10] W. J. Moore. *Physical Chemistry.* Prentice Hall, Inc., Englewood Cliffs, N.J., 1962.

[11] M. S. Plsesset and A. Prosperetti. Flow of vapour in a liquid enclosure. *J. Fluid Mech.*, 78(3):433–444, 1976.

[12] S. G. Bankoff. A note on latent heat transport in nucleate boiling. *AICHE J.*, 8(1):63–65, 1962.

[13] M. A. Unger, H. P. Chou, T. Thorsen, A. Scherer, and S. R. Quake. Monolithic microfabricated valves and pumps by multilayer soft lithography. *Science*, 288:113–116, 2000.

[14] H. Sizuki and R. Yoneyama. A reversible electrochemical nanosyringe pump and some considerations to realize low-power consumption. *Sensors and Actuators B:Chemical*, 86:242–250, September 2002.

[15] PD Dunn and DA Reay. Heat pipe. *Physics in Technology*, 4(3):187–201, 1973.

[16] YF Maydanik, SV Vershinin, MA Korukov, and JM Ochterbeck. Miniature loop heat pipes-a promising means for cooling electronics. *Components and Packaging Technologies, IEEE Transactions on [see also Components, Packaging and Manufacturing Technology, Part A: Packaging Technologies, IEEE Transactions on]*, 28(2):290–296, 2005.

[17] M. S. Plesset. Note on the flow of vapor between liquid surfaces. *J. Chem Phys*, 20(5):790–793, 1952.

[18] D. Jakubczyk, M. Zientara, K. Kolwas, and M. Kolwas. Temperature dependence of evaporation coefficient for water measured in droplets in nitrogen under atmospheric pressure. *J Atmos Sci*, 64:996–1004, 2007.

[19] D. Ross, M. Gaitan, and L. Locascio. Temperature measurement in microfluidic systems using a temperature-dependent fluorescent dye. *Anal. Chem*, 73(16):4117–4123, 2001.

[20] D.R. Lide et al. *CRC handbook of chemistry and physics*. CRC Press, 2003.

[21] V. K. Pustovalov. Theoretical study of heating of spherical nanoparticle in media by short laser pulses. *Chem Phys*, 308:103–108, 2005.

[22] G. Chen. Nonlocal and nonequilibrium heat conduction in the vicinity of nanoparticles. *J. Heat Transf.*, 118:539–545, 1996.

[23] D. A. Boyd, L. Greengard, M. Brongersma, M. Y. El-Naggar, and D. G. Goodwin. Plasmon assisted chemical vapor deposition. *Nano Lett.*, 6(11):2592–2597, 2006.

[24] V. K. Pustovalov and V. A. Babenko. Optical properties of gold nanoparticles at laser radiation wavelengths for laser applications in nanotechnology and medicine. *Laser Phys Lett*, 1(10):516–520, 2004.

[25] R. C. R. Wootton and A. J. deMello. Continuous laminar evaporation: micron-scale distillation. *Chem. Commun.*, pages 266–267, 2004.

[26] M. J. A. Shiddiky and Y. B. Shim. Trace analysis of DNA: Preconcentration, separation, and electrochemical detection in microchip electrophoresis using Au nanoparticles. *Analytical Chem.*, 79(10):3724–3733, 2007.

[27] R.D. Deegan, O. Bakajin, T.F. Dupont, G. Huber, S.R. Nagel, and T.A. Witten. Contact line deposits in an evaporating drop. *Physical Review E*, 62(1):756–765, 2000.

[28] Y. Wang, W.P. Chen, K.C. Cheng, H.L.W. Chan, and C.L. Choy. Effect of ac-powered water electrolysis on the structural and optical properties of indium tin oxide thin films. *J. Am. Ceram. Soc.*, 88(4):1007–1009, 2005.

[29] A.V. Oppenheim, A.S. Willsky, and S.H. Nawab. *Signals and Systems*. Prentice Hall, Upper Saddle River, N.J., second edition, 1997.

[30] Y. C. Wu and P. A. Berezansky. Low electrlytic conductivity standards. *Journal of Research of the National Institute of Standards and Technology*, 100:521–527, September 1995.

[31] P. D. I. Fletcher, S. J. Haswell, and X. Zhang. Monitoring of chemical reactions within microreactors using an inverted raman microscopic spectrometer. *Electrophoresis*, 24:3239–3245, 2003.

Chapter 5

Fluorescence Coding for Optofluidic Systems

5.1 Introduction

In the previous chapters of this thesis, we have discussed using colloidal suspensions to modify the bulk properties of liquids. In this chapter we will explore the possibility of manipulating individual particles in order to represent information and provide functionality at very small scales. Previously we have focused on plasmonic particles due to their strong interaction with the optical field. Here the applications we will explore will be based around the unique optical properties of photoluminescent quantum dots.

Semiconductor quantum dots (QDs) are particles with dimensions between 1–10 nm, small enough that the the density of states of carriers in the QD become discrete. Since there is not a continuous band of states for carriers to occupy, the QD behaves as an "artificial atom", with transitions between discrete energy levels that result in emission of photons in a very narrow spectral line[1]. Brus described the of mechanism of quantum confinement in a QD and the relationship between the particle diameter and the wavelength of emission in his 1984 paper[2].

For our purposes it is sufficient to consider a semi-classical picture of what happens when a QD is excited by a photon. In a bulk semiconductor, absorption of

a photon promotes an electron from the valence band to the conduction band, creating a free conduction electron and a corresponding hole in the valence band. In this picture, the electron has enough energy to escape from the Coulombic potential of the hole, and is "fully ionized". However, in a QD the electron is confined by the material boundary of the crystal, so that it is remains close enough to the hole that both are bound together by an appreciable Coulombic attraction. This bound hole-electron pair is known as an exciton, and is conceptually similar to the Bohr model of a hydrogen atom in its ground state. The smaller the diameter of the QD, the tighter the coupling of the exciton, and the more energy is needed to form it. When the electron-hole pair decays (i.e. the hole recaptures the electron) a photon is emitted with a wavelength corresponding to the energy of the exciton. The size and composition of the particle can be selected to obtain emission at the desired wavelength, making semiconductor QDs an attractive material for photoluminescent tags and probes[3]. Quantum dots are superior fluorescent markers to organic dyes in several ways. Traditional fluorescent dyes tend to exhibit broad FWHM emission spectra and require optical pumping at frequencies near to their peak fluorescence frequency. On the other hand, quantum dots can be pumped efficiently by a wavelength near to the absorption band of the semiconductor material, regardless of their peak luminescence frequency. Due to the relatively narrow bandwidth of the luminescence of a sample of nearly mono-disperse quantum dots, the can act easily distinguishable markers through out the visible band. Here we consider using the spectral properties of colloidal QDs to achieve subwavelength optical resolution in an imaging system, and as a means to store more information in a diffraction limited volume.

5.1.1 Imaging with Arrays of Nanoparticles

A naive attempt at photoluminescence near field imaging could be envisioned as a flat, transparent plane covered with M different species of quantum dots with luminescence

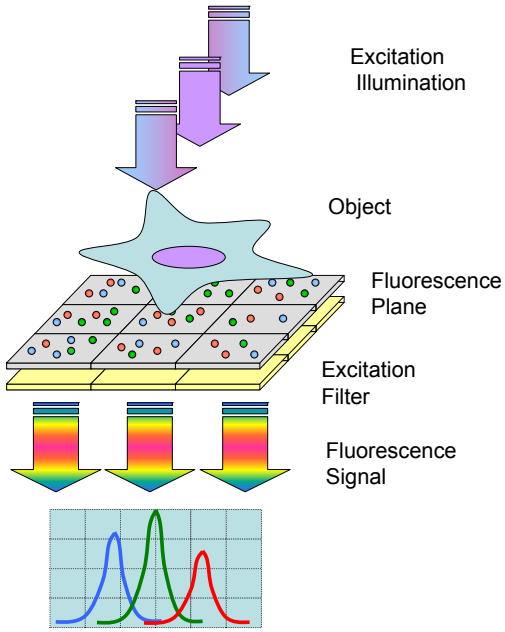

Figure 5.1: Schematic drawing of imaging using spatial patterned spectral coding

in M unique spectral bands. We will refer to this construct as the fluorescence plane. The target to be imaged is placed in contact with this plane and illuminated from above. Refractive index variation in the sample will create a near field intensity pattern on the fluorescence plane. The individual quantum dots are pumped by this excitation so that regions that are brightly illuminated contribute strongly to the total luminescence spectra. By collecting the the photoluminescence, filtering out the excitation wavelength, and examg the recorded spectra, we want to extract as much information as possible about the target.

Mathematically, the imaging system can be modeled as an $N \times M$ matrix, $T(\lambda, j)$ where N corresponds to the optically resolvable points in the input space. The excitation pattern is a vector length N, $\vec{x}(j)$, whose values are the intensity of the light projected through the object onto the plane at a point j. The recovered spectrum, $\vec{S}(\lambda)$ is ideally given by the product:

$$T(\lambda, j)\vec{X}(j) = \vec{S}(\lambda) \tag{5.1}$$

In order to recover the image of an unknown object from the recorded spectrum, we need to know the values of$T(\lambda, j)$. It can be constructed by scanning all the points j with an scanning near field microscope (NSOM), as depicted in Figure. Figure 5.1.1 is an example of such a scan. The image is of the photoluminescence intensity of CdSe quantum dots with peak emission at 605 nm scanned with an NSOM tip that provides the excitation light of 488 nm wavelength from an Argon-Ion laser. Although the NSOM used in this experiment was not equiped with filters to distinguish separate species of QDs, the same technique can be used to characterize the luminescence signal of multiple QD species by repeating the same scan utilizing notch filters matched to the different QD frequencies.

Once the imaging system matrix is specified it is conceptually simple to reconstruct an unknown object intensity distribution from a measured spectrum. The measured spectrum vector should be multiplied on the left by the inverse of the imaging system matrix to recover the object intensity. It is immediately apparent that this simple approach will fail spectacularly in the case of a random distribution of quantum dots when $M > N$. The matrix inverse is only strictly defined for matrices which have full rank (i.e. $M = N$). Our matrix T is therefore under determined and cannot be inverted. We can compute a pseudo-inverse, T^{+}, using the singular value decomposition and use it to perform the object reconstruction [4]. However, the number of resolvable points that we can achieve is limited to N by the number of species of QDs. Since there are only on the order of 10 distinguishable species of quantum dots which luminesce in the visible band, our reconstruction algorithm can not reproduce any reasonably interesting image with acceptable performance. More measurements must be taken to allow for better performance. Taking multiple measurements of the object as it is scanned across the fluorescence plane adds M rows to the matrix T and

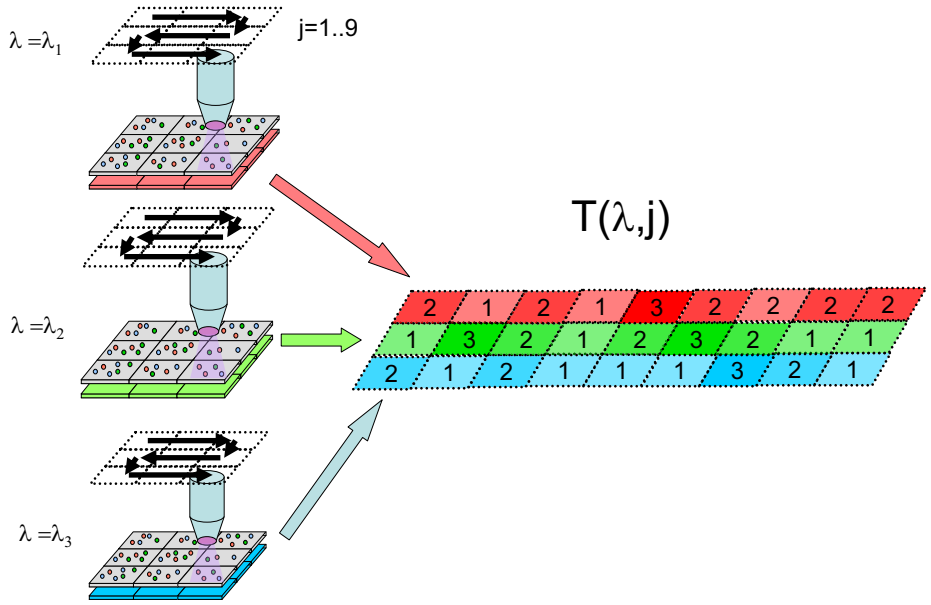

Figure 5.2: Construction of the imaging system matrix T by successive NSOM scans for each species of quantum dot

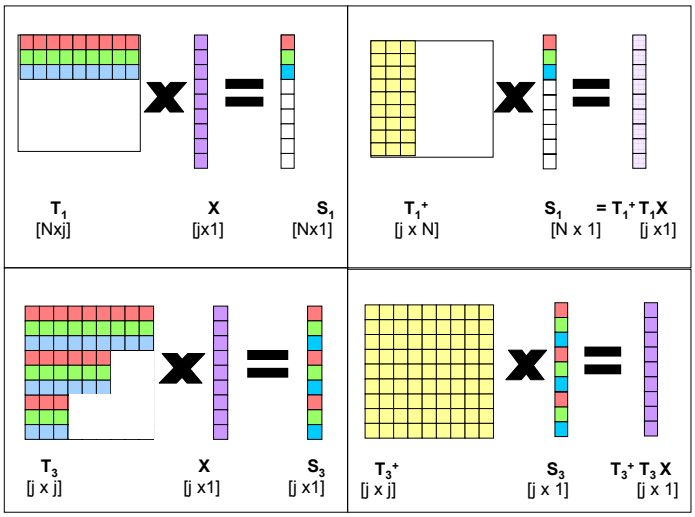

Figure 5.3: Graphical depiction of the imaging algorithm for stationary and scanned objects

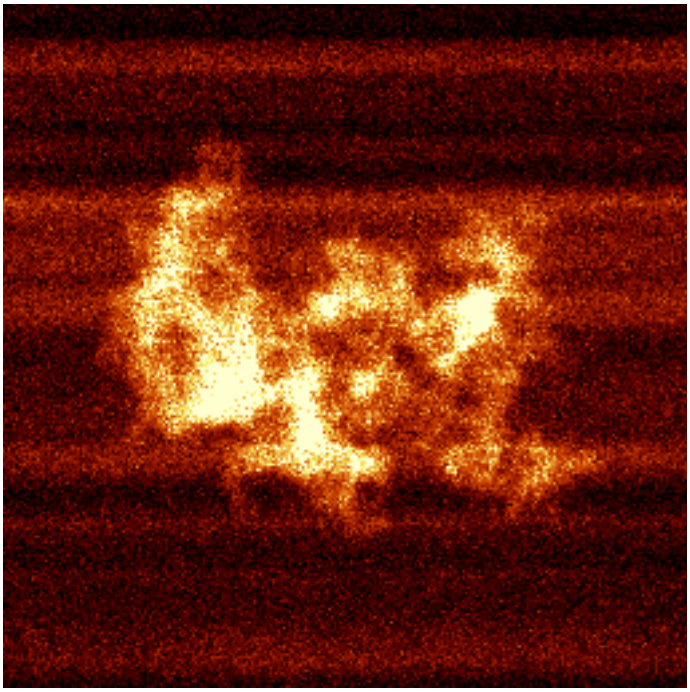

Figure 5.4: Scanning near field optical microscope image of CdSe nanoparticles. The field of view is $40\,\mu$m $\times$ $40\,\mu$m

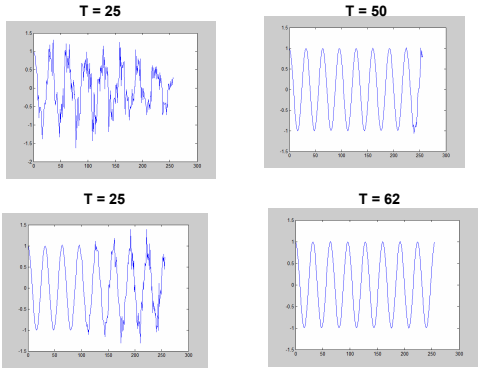

Figure 5.5: The effect of number of scan steps on image quality for a sinusoidal input

the vector X for each measurement.

With a sufficient number of samples obtained by scanning, the matrix T becomes nearly full rank, and the pseudo-inverse we can calculate gives a much better reconstruction of the object space. This process is graphically depicted in figure 5.1.1, where the matrix T_1 corresponds to imaging using only a single measurement, and the matrix T_3 corresponds to imaging using a 3 point scan. The reconstructions of the object vector are given by $T_1^+ S_1$ and $T_3^+ S_3$ respectively. However, in the first reconstruction, T_1^+ has a rank of only 3, and S_1 has only 3 nonzero entries. Although the reconstruction yields a vector of the same length as X, much of the structure of X has been lost in the process. The second reconstruction involves matrices of full rank, so all the information in X is preserved in its reconstruction. The amount of scanning steps is critical to the quality of the reconstructed image. As an example, figure ref1dreconstruction shows the reconstruction of a 1 dimensional sinusoid using a simulated 1-dimensional fluorescent "plane" with 250 pixel elements with random intensities in five separate wavelengths. The image recovered from T_{25}, which is composed of 25 measurements with a 10 pixel shift of the object vector after each measurement, is degraded, although the periodicity is i still apparent. In contrast,

the recovered signals from matrices T_{41},T_{50},T_{62} demonstrate increasing quality. The overdetermined matrix T_{62} allows for a distortion free reconstruction (n.b. the mathematical operation produces a perfect copy of the input object in the absence of noise; Any practical system would contribute noise to the detected spectrum $\vec{S}$ which would also be reproduced in the reconstructed image). The challenge in constructing a workable imaging system based on these principles is to combine controlled scanning of the object to be imaged with proper spatial patterning of the luminescent particles in order to minimize ambiguity and maxim we will consider the the optofluidic microscope (OFM), developed in collaboration between Dr. Psaltis' and Dr. Yang's labs at Caltech.

5.1.2 The Optofluidic Microscope

The OFM is a device which replicates the functionality of a high quality optical microscope by direct measurement of an small object as it flows through a microfluidic channel in close proximity to photodetectors[5]. The device is composed of a CCD or CMOS sensor, which is covered with an opaque metal layer. Holes on the order of the diffraction limit of visible light ($200\,\mu$m) are milled in the metal layer, which act as apertures over the pixels of the sensor. The organization of the holes is such that each aperture occupies its own pixel, allowing for unambiguous recovery of high resolution information in two dimensions. Illumination is directed from above so that as the object flows across the sensors, the transmission of each aperture is modified. The intensity at each pixel as a function of time forms a high resolution scan in the flow direction. The resolution of this scan is determined by the hole size. Resolution in the direction transverse to the flow is determined by the center to center distance between holes in the transverse direction.

The OFM is conceptually a distant cousin to the near field scanning optical microscope (NSOM). In the OFM system, the object is scanned via fluid flow, rather than

the scanning of the illumination and detection by mechanical motion of the NSOM tip. However, the resolution and sensitivity of the OFM are limited by several aspects of the implementation. The first of these is the relationship between the hole size and the device sensitivity. To achieve higher resolution, the hole size of the OFM must be scaled down, yet as the size of the hole becomes smaller than the diffraction limit the sensitivity degrades rapidly. The second limitation to the resolution of the OFM is the blurring caused by any motion of the object relative to the fluid stream, such as the deviations caused by Brownian motion.

The sensitivity of the signal detection degrades rapidly as a function of the hole size. The sensitivity dependency of the OFM method on the hole size is a complex problem. We will briefly address this issue in the limit where the metal layer in which the holes are etched is perfectly conductive. In the case of holes which are much larger than the wavelength of visible light, the effective transmission are of the hole is the same as its physical cross section. However, as we approach the limit of holes with diameter much smaller than the radiation, the effective transmission drops off much faster than the geometric size of the hole. In this size regime, Bethe showed the effective transmission of a hole in a infinitesimally thin perfect electrical conductor is proportional to the sixth power of its diameter [6]. De Abajo et al. have recently reported that the transmission is further attenuated if the finite thickness of the conductive layer is taken into account[7]. Their simulations demonstrate a drop off in transmission that is exponential with the layer thickness. Combining the theoretical model of Bethe with the results of De Abajo et al. we develop an expression for the effective transmission cross-section in the small hole regime as:

$$C_{hole} = \frac{16\pi^3 a_{hole}^6}{27\lambda^4} \exp\left(-4\pi d \sqrt{\frac{0.586^2}{a_{hole}^2} - \frac{1}{\lambda^2}}\right). \tag{5.2}$$

The sharp drop in transmission efficiency with decreasing hole size sets the effective

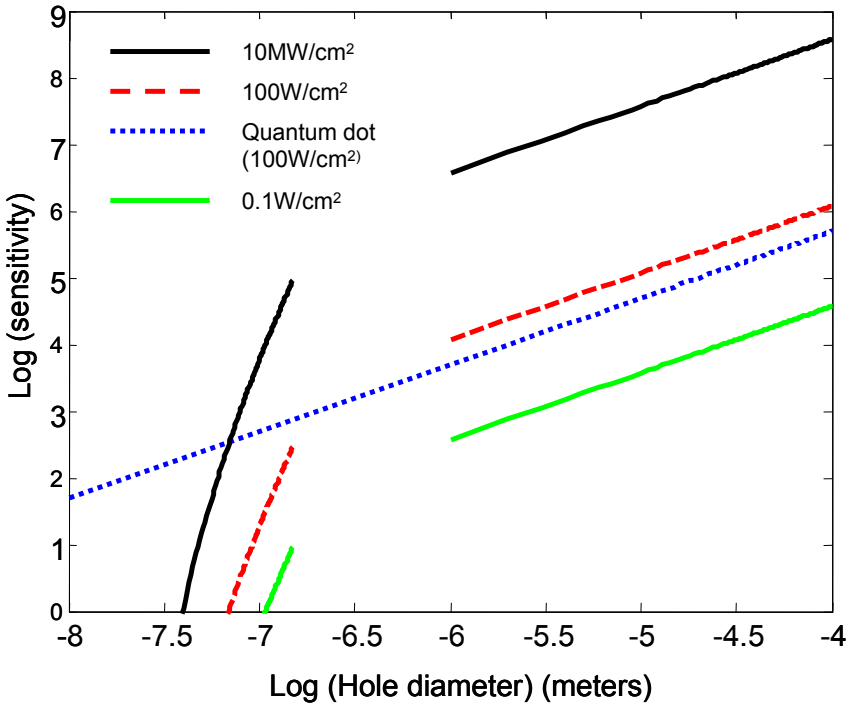

Figure 5.6: Logarithmic plot of the sensitivity of detection of a single aperture of the conventional OFM as a function of hole diameter, compared with the calculated sensitivity when using photoluminescent QDs occupying the same area.

lower limit of the resolution in a conventional OFM. The total number of photons captured by our sensor in a time increment τ is given by:

$$N = \frac{I\, C_{hole} \tau}{h\lambda/c} \tag{5.3}$$

We define p as the contrast of the target object, that is, the fraction of light that is occluded by the presence of the target above the hole, in order to define the sensitivity of the OFM device. We determine the sensitivity of the system by equating the measured change in the signal due to the occlusion, Np, to the noise of the system. The total noise term is equivalent to the Shot noise, plus any detector noise. The sensitivity of the system is given by the ratio:

$$1/p = N/\sqrt{N + (n_r \tau)}. \tag{5.4}$$

Here n_r is a term that encompasses thermal and other sources of receiver noise. We use equations 5.2 and 5.4 to determine the highest resolution achievable under realistic experimental conditions. Figure 5.6 shows the computed sensitivity as a function of hole size for several different intensities. The 0 dB point sensitivity (i.e. a SNR of 1) under natural illumination happens at hole diameter slightly above 30 nm. Increasing the intensity illumination light field has diminishing returns in terms of achieving higher resolution; an 8 order magnitude illumination intensity increase from natural light illumination (i.e. sunlight, used in this analysis as a convenient reference example) to high laser intensity illumination is only capable of improving resolution by less than an order of magnitude.

The second factor in the original OFM design that limits its resolution is the large distance between apertures. In order for each hole to occupy a separate pixel on the detector chip the distance between holes must be the same as the pixel pitch. Brownian motion over the the root mean square deviation along a single dimension,

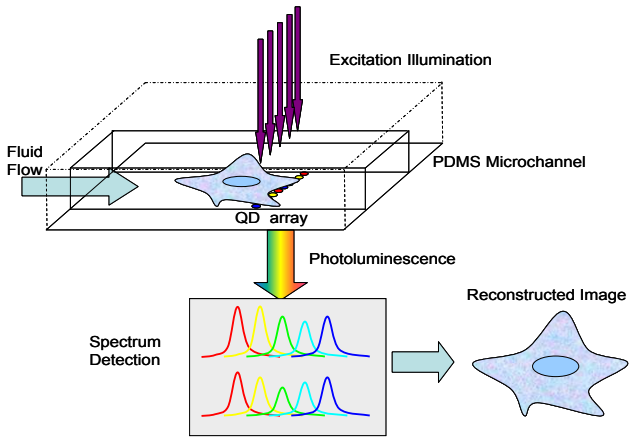

Figure 5.7: QD-OFM. An object to be imaged is microfluidically scanned across an array of small holes filled with different species of QDs. Excitation illumination is occluded by the target, causing modulation of the QD photoluminescence signal. The time varying intensity of each spectral band is monitored and digitally inverted to reconstruct the target image with sub-wavelength resolution.

of a spherical particle of diameter l in a fluid of viscosity η on a time scale of t is given by:

$$\sqrt{< x^2 >} = \sqrt{\frac{2k_bTt}{3\pi\eta l}} \tag{5.5}$$

where k_b is the Boltzmann constant and T is the system temperature [8]. An object of diameter 10 nm drifting in room temperature water will experience a mean deviation of 29 nm in 1 dimension for a time period of 10 ms. There is also a Brownian motion actuated rotation, however the relative extent of the rotation and its effect on resolution is small compared with the translational Brownian motion.

5.1.3 Spectral Coding for Optofluidic Microscopy

To overcome the resolution limitation of the conventional OFM we investigate the substitution of quantum dots in place of the holes. In this approach, the light trans-

mitted through the fluidic channel excites a quantum dot array as opposed to being transmitted through a hole array. Each quantum dot acts as a probe that relays information about the illumination at its location. Since the photoluminescence signal produced is at a different frequency than the excitation emission, the illumination source can be removed as in a conventional fluorescence microscope. The photoluminescence signal from a quantum dot can be much stronger than the transmission of a similarly sized hole. The cross section of a QD is proportional to its physical volume [9]; there is no additional exponential efficiency drop off in the collection area as in the case of a transmission hole.

To calculate the sensitivity of a quantum dot based OFM system, we replace the term C_{hole} in Eq. 5.3 with ηC_{qd}, where η is the quantum dot's photoluminescence emission efficiency and C_{qd} is the quantum dot's absorption cross-section. There is intrinsic excitation illumination intensity limit due to the finite photoluminescence decay lifetime ($\approx$25 ns) associated with the quantum dots [10]. Specifically, an excitation intensity beyond the saturation intensity ($\approx$100 W/cm^2) will not result in a stronger photoluminescence signal; Saturation of the excitation-emission process will actually degrade the quality of the images. For a quantum dot species with mean size of 10 nm, photoluminescence lifetime of 25ns, we calculate an achievable sensitivity of about 20dB and a resolution of 10 nm with a nominal illumination intensity of 100 W/cm^2. For a lower resolution and higher sensitivity OFM configuration, we can group more quantum dots within each collection domain. For an aperture of 100 nm filled with 10 nm QDs, the sensitivity is almost 28 times greater than transmission through a metal hole of the same diameter.

The use of QDs can also reduce the impact the of blurring due to Brownian motion. In the conventional OFM, holes that are adjacent in the x direction must be separated by at least the pixel pitch in the y direction so that each pixel detects the transmission of a single hole. If we replace each hole with quantum dot with a

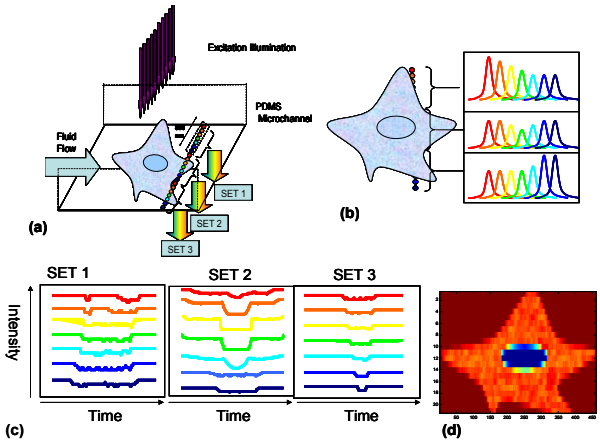

Figure 5.8: (a) Concept of a QD-OFM containing 3 sets of 7 holes each. Each set is separately resolved. (b) Spectral signature of photoluminescence from each of the QD filled nanowells sampling a line in the target. (c) Simulated time variation of each spectral band as target is scanned across array. (d) Reconstructed image with resolution of 100nm.

unique spectral signature, we no longer need to separate the signals from multiple QDs onto individual pixels in order to remove ambiguity. In principle, either filters or a diffractive elements can be used to read out the distinct photoluminescence bands of the QDs. This allows measurements of all y positions simultaneously, as shown in Figure 5.1.3.

5.1.4 Nanostructured Surfaces and Electrical Trapping

In order to create a patterned photoluminescence signal that can be used for an optofluidic microscope, we must have a method to selectively trap different species of particles in precise locations. Electrical fields can be used to trap small charged particles suspended in liquids. Quantum dots of different colors have been trapped on patterned ITO surface using so called layer by layer deposition [11]. By alternating the sign of the charge on an electrode, the surface can be made to either accept or repel the charged dots.

The specificity and flexibility of this approach may be extended by targeted delivery of quantum dots to electroactive nanowells. An electroactive well is simply a nanohole defined in an insulator that is sandwiched between two conducting layers; typically the substrate is ITO on glass and the top electrode is gold or aluminum deposited by evaporation. When a voltage is applied between the two conducting layers, strong electrical are present inside the well and extending into the space above it. As a suspension of nanoparticles (or dye molecules) flows over the activated nanowell, the suspended particles feel a trapping force due to the influence of the electric field distribution,

$$\vec{F_E} = q\vec{E} + 2\pi v \nabla \left(\vec{E}^2\right) \cdot \Re \left(\frac{\epsilon_p - \epsilon_m}{\epsilon_p + 2\epsilon_m}\right), \tag{5.6}$$

where q is the charge on the particle, $\vec{E}$ is the electric field v is the volume of the particle and ϵ_p and ϵ_m are the dielectric constants of the particle and medium re-

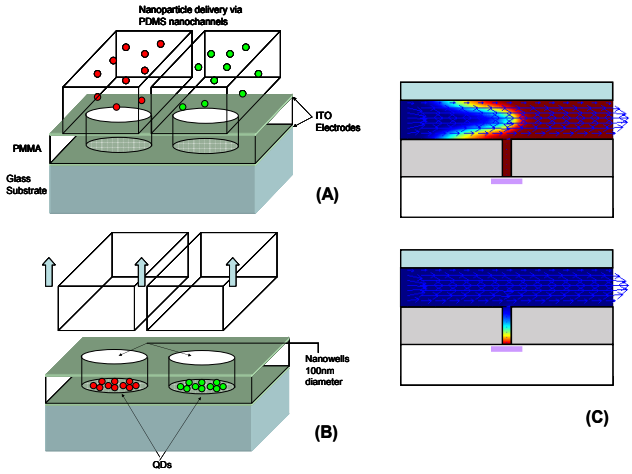

Figure 5.9: (a) Delivery of QD solutions to nanowells using PDMS nanochannels. (b) QDs are deposited on the substrate due to the electric field applied between the ITO electrodes. The nanochannels are removed, revealing a complete OFM substrate. (c)Finite element simulation of filling an electrostatically active nanowell with charged QDs

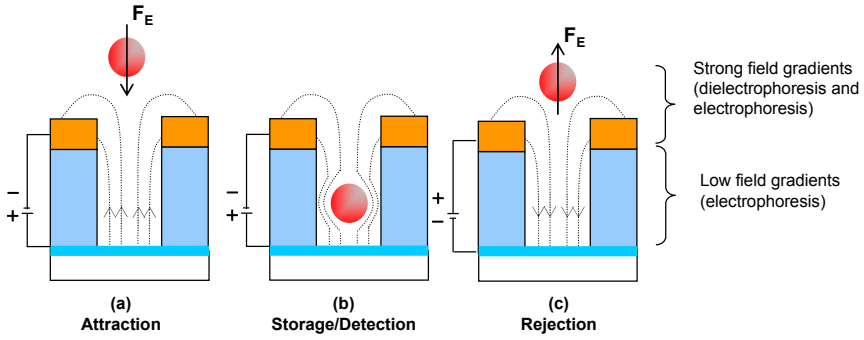

Figure 5.10: Electrokinetic forces for nanoparticle manipulation

spectively. Examination of equation 5.6 that the dielectrophoretic force is directed in the direction of strongest field gradients with a sign dependent on the dielectric constant of the particle relative to that of the medium; whereas the direction of the electrophoretic force is aligned with the direction of the applied field, with a sign dependent on the sign of the charged particle. Reversing the applied voltage will cause the electrophoretic force to change direction, which can be used to eject a charged particle. Figure 5.1.4 illustrates the electrokinetics of particle interaction with this type of well.

For electrostatic confinement to work in this structure, the applied potential must be sufficiently strong to overcome thermal diffusion of the nanoparticles. A fundamental limitation of any localized trapping scheme, such as that in Figure 5.1.4, is that as the applied potential between the upper and lower electrodes must be less than 1V to remain below the activation energy for electrolytic bubble generation and degradation of the ITO surface. We perform an order of magnitude analysis, comparing the amount of energy required to move a conjugated quantum dot out of the well against the applied potential field, with energy of the thermal diffusion, k_bT.

$$\frac{W_{trap}}{W_{therm}} = \frac{qV}{k_bT} \tag{5.7}$$

Estimating the total charge from the electrophoretic mobility of the conjugated system reported by Gao et al. [11] yields an W_{trap}/W_{therm} ratio of 455 for an applied voltage of 1V. This result shows that the trapping potential should dominate the thermal diffusion.

We constructed a prototype of an electroactive nanowell by e-beam lithography. The device was manufactured using a relatively simple process which begins by spin coating an initial layer of PMMA, which serves as an insulation layer between the optically transparent Indium Tin Oxide (ITO) layer and a 100nm thick gold layer

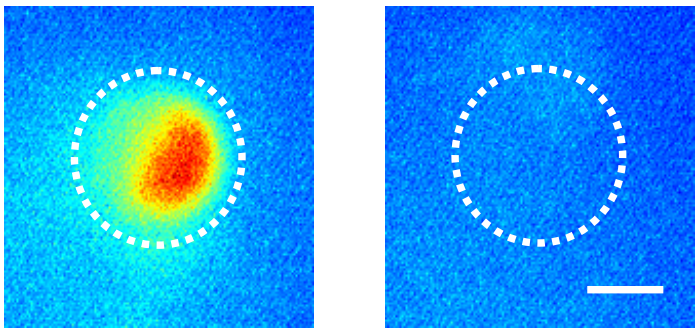

Figure 5.11: Fluorescence imaging of electrokinetic trapping and rejection of a dye solution in a 1 micron "nanowell". The dotted line illustrates the nanowell boundary, and the scale bar is 500 micron.

evaporated on top. A second PMMA layer is then spun on the top layer and the trapping wells defined by electron beam lithography. Following exposure the upper PMMA layer is developed and the hole pattern is etched in the gold layer. The upper PMMA layer is then washed off and the bottom layer is developed creating the wells. PDMS fluidics are then used to deliver the quantum dot cocktails to the general area of the targeted storage site and the electric field applied between the liquid in the channel and ITO layer is used to attract the quantum dots to the appropriate storage well (See figure fig:dye). Erasing is done by reversing the polarity and rejecting the cocktail in to the bulk. Readout is accomplished though an inverted epi-fluorescence scheme whereby both the excitation light is sent through the same high N.A. objective and the signal collected and sent through the fiber spectrometer. The gold layer serves to significantly reduce background noise.

The feasibility of trapping charged particles was tested by initial experiments using Rhodamine 110, a common fluorescent dye. Rhodamine 110 was chosen because it has an electrophoretic mobility comparable to that of thioglycolic acid stabilized CdTe quantum dot nanoparticles[11]. A dye–water solution was flowed over an electroactive nanowell structure with a diameter of 1 micron, while a trapping voltage of $\tilde{0}.5$V

was applied. The excitation illumination is a Argon Ion laser at 488 nm, which is suppressed by a holographic notch filter before detection. Figure 5.1.4 shows the clear visibility of the dye trapped within the nanowell when a positive potential is applied. Reversing this potential causes the trapped dye to rejected from the well, and the measured fluorescence is virtually indistinguishable from the background fluorescence.

5.1.5 Design of a Spectrtal OFM for enhanced resolution

We have already discussed how using a photoluminescent reporter could be used in the OFM architecture to increase the resolution of a single aperture. To maximize the resolution of the system, we want to arrange quantum dots of different species at their luminescence wavelengths encode position information smaller than the wavelength of the pump illumination. The QD based realization is shown in Figure5.1.3. We first etch a line of holes in a line perpendicular to the microfluidic channel. These wells are then filled with QD of different varieties. We arrange the type of QD deposited into each well such that their emission spectrum varies from one side of the channel to the other. Ideally, when the array of QDs is uniformly illuminated with the pump, the wavelength of the photoluminescence increases linearly across the array. It is important to note the possibility of Forster Resonant Energy Transfer (FRET) along the array[12, 13]. Exchange of energy from QDs with higher excitation frequencies to those with lower frequencies would cause quenching of the higher energy particles, destroying the local independence of the photoluminescence. However, research into FRET has shown the process is only active over distances less than about 5 nm. This distance represents the absolute lower bound for using the luminescence signal from spectrally distinct QDs to encode position. Since we have a limited number of usable wavelengths, it is not possible to image at high resolution across a distance greater than several microns. To solve this problem the full spectrum of dots can be repeated. Each full set of QDs can span a micron sized region, serving to encode the

subwavelength information in that region as photoluminescence. The multiple sets of QDs can be mapped to separate detectors optically, since each set itself is above the resolution limit created by diffraction.

In the spectral OFM, the object to be imaged is transported in the microfluidic channel and is maintained in close proximity to the QD array. The structure is illuminated from above with light which wavelength is suitable for inducing photoluminescence in the QDs. In the absence of any object to be imaged, the QDs at the floor of the channel should emit light uniformly. Light scattered or absorbed by the target object creates a shadow pattern on the floor of the channel, creating a photoluminescence signal that contains the information of the pump light distribution. Scatterers and absorbers that are further away from the Qds have reduced impact on the signal spectrum, do to the defocusing. This rejection of distant scattering creates an optical sectioning effect in a manner similar to a confocal microscope. Only the near surface of the object is scanned by the system. A slice of the image along the transverse direction is obtained by displaying the spectrum of the photoluminescence signal emitted by the QD array as shown in Figure 5.b.

A single "snapshot" of the photoluminescence spectrum contains information about the pump intensity pattern in the x direction. To recover a full 2-D high resolution scan, the object must be scanned slowly in the z direction (down the channel), and the full spectrum recovered for each z-position. In practice, the resolution in z will be determined by the integration time needed to capture each spectrum. This can be reduced down to the resolution limit of the QD apertured given sufficiently bright luminescence and a sensitive detector.

In order to estimate the overall resolution of the microscope, we imagine the object being scanned is a single test probe, a nanoparticle with diameter $d << \lambda$, that strongly scatters or absorbs at the pump wavelength. As the nanoparticle crosses over the array of QDs, it blocks the pump light from reaching the QD filled well that

is at the same position in x as our test probe. We will observe a transient dip in the corresponding spectral component in the detected signal. If the test probe is traveling very close to the floor of the microfluidic channel, then its "shadow" will be roughly equal to d+L where d is the diameter of the test probe and L is the distance of the test probe from the QDs.

If the spacing of the QD filled well is set to $dx = d + L\ L$, then only one QD filled well in the array is principally affected. If L is increased to a distance L1, the "shadow" spreads to multiple QD filled well and the intensity modulation at the receiving QD filled well drops off as (1/ L1)2. Therefore a scattering center far away from the floor of the microfluidic has little impact on the observed signal. The resolution in x is approximately equal dx=L and the depth of focus is approximately equal to L as well for a slice of the object that is situated a distance L away from the QD filled well. The resolution in the z direction is also dx. The separation between QD filled well is limited by the absorption cross section of individual QD filled well, which can be as low as 10nm and in general is well below 100nm. Therefore, in this realization, the limit on the resolution is set by the minimum distance L away from the at which we can flow an object. Experimental measurement of the rejection of scattered light far from the plane was recently reported by Dr. Yang's group[14].

Since the QD filled holes may be spaced closer than the optical resolution, imaging resolution is increased by packing as many spectrally distinct quantum dot types into a diffraction limited spot as possible. The greatest effective resolution achievable is determined by the optical resolution of our detector and the number of spectrally distinct quantum dot types that is commercially available. This can be understood from the fact that we can repeat the quantum dot sequence across the channel, but each sequence must be optically resolvable from each other (see Fig.5.1.3). Assuming an optical resolution of 800nm and a commercially available variety of quantum dot of 8 distinguishable types, the realistic resolution that we can achieve with such a

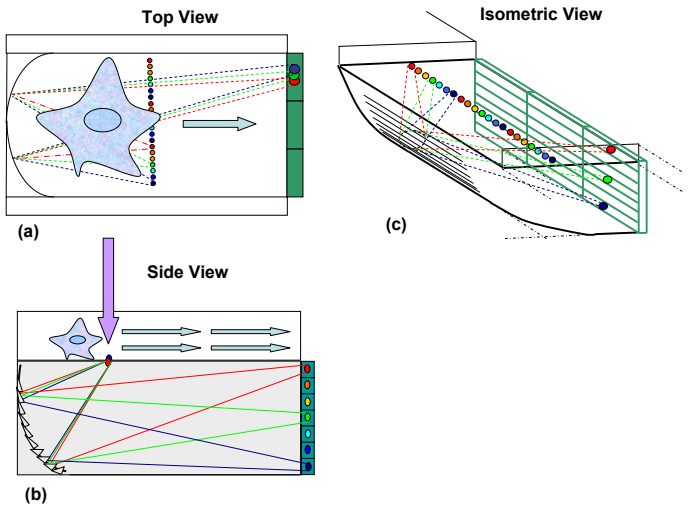

Figure 5.12: A scheme for 3 dimensional optical integration of a quantum dot spectral OFM

system is 100nm. An optical resolution of 800nm is chosen to account for the fact that our imaging system will most likely not have diffraction limited performance.

Until now we have not discussed the method used for detecting the photoluminescence spectra. In the conventional OFM, it is sufficient to place the aperture array directly on a sensor, since we only need to measure transmitted intensity. To perform a spectral measurement, we must be able to first separate the QD sets from each other, and then map the peak emission wavelength of each species in a set onto a separate detector. Diffractive optics can be used to accomplish both these tasks in a monolithic, integrated fashion that preserves the small form factor and convenience of the conventional OFM. Figure 5.1.5 shows a schematic design of a possible approach. The fluidic delivery and the the QD array are composed normally. A diffractive optical element, cast in PDMS or a similar material, separates wavelengths along the z direction. In our design, the diffractive element is incorporated into a curved surface, so that the luminescence from each set of QDs is focused onto a line of detectors.

Recent work using replica molding to create three dimensional optical elements and diffractive optics in soft lithography polymers provides techniques that can be used to assemble the 3-d imaging spectrometer from cast components[15, 16, 17].

5.2 Quantum Dot Optical Memory

The quantum dot OFM demonstrates that we can encode information in areas smaller than the diffraction limit, and use the subwavelength pattern of fluorescence to reconstruct a high resolution image. A similar approach of patterning of quantum dots on a surface can also be exploited to perform data storage with increased density. The development of scalable multilayer soft lithography for highly integrated microfluidic devices has led to renewed interest in fluidic memory devices, through either discrete binary sample storage (e.g. presence or absence of dye)[18] or low Reynolds number fluidic flip-flops which exploit the non-linear behavior of viscoelastic polymer solutions[19]. A drawback of existing devices is that information storage density (on the order of 50 Bs/cm2) tends to be low compared with exiting optical storage mechanisms, which for 4.6GBytes DVDs is roughly 50 MBs/cm2. The recently popularized BlueRay disc format uses a 405 nm wavelength laser with a diffraction limited spot size of 580 nm, and can store more than 22 Gb.s on a disc [20].

While simply downscaling the microfluidic feature size is an obvious technique to increase the density of optofluidic data storage, it does not provide a direct route by which such memories could exceed the performance of conventional optical discs such as blue-ray. The unique ability of microfluidics to deliver and mix discrete samples of different components in precise ratios does provide the opportunity to exploit spectral multiplexing optical encoding. Such optical multiplexing techniques have been recently used for massively parallel DNA or protein sequencing [21], and even proposed as an info-ink to replace exiting barcodes [22].

The principal of spectral encoding involves creating discrete information packets which contain different intensity levels of different photoluminescent nanoparticles. For example, 10 different intensity levels of an individual species provides 10 different codes which can then be increased exponentially by increasing the number of individual species. Under such a scheme the equivalent number of bits in a single information packet, N, is described by equation 5.8,

$$\log_2 N = I^M - 1 \tag{5.8}$$

where I is the number of intensity levels and M is the number of individual species (the -1 accounts for the fact that the all zero code cannot be distinguished from the background and therefore would be an ambiguous result). The use of 10 different intensity levels with 10 individual species would provide $1010 - 1$ individual codes, equivalent to slightly more than 33-bits in a single information packet. As such shrinking down fluidic storage units to the micron-scale could yield similar or even greater storage density than conventional DVDs or BlueRay discs.

5.2.1 Experimental Results

Initial experiments were performed on a stationary substrate (i.e an ITO coated microscope slide). The data storage locations are electroactive nanowells defined by e-beam, as previously outlined. We fabricated microfluidic channels capable of mixing quantum dot cocktails of with three different colors. The quantum dots themselves were commercially available, and obtained from the Qdot corporation. The three species used were CdSe dots with emission of 525 nm (green) 565 nm (yellow) and 605 nm (red) wavelengths. All microfluidic transport visualization was conducted on a florescence microscopy setup comprising of an inverted microscope, 100W mercury broadband illumination source, and a specially designed quantum dot filter (Chroma

Technology Corp., Rockingham, VT; excitation: bandpass 400nm/120nm emission: long pass 500nm) which allowed for broad illumination of the sample from the UV to the blue and good transmission for green and longer wavelengths. Images were captured on a color CCD camera and spectral measurements were taken using an optical fiber spectrometer (Ocean Optics, Inc.).

Our pressure driven transport system was controlled using a series of valves integrated onto the chip, using the multilayer soft lithography technique mentioned earlier [23]. These valves were actuated by pressurized air regulated by a set of computer controlled external solenoid valves. Opening the solenoid allows the control layer channel to fill with pressurized air, causing the thin elastomer membrane of the control channel to be squeezed shut, forming an effective gate valve for the fluid flow. The control layer and flow layer molds were both created with photolithography, and cast in PDMS. The control layer was formed from a 5:1 ratio of RTV 615A to RTV 615B (by weight) and poured several millimeters thick. The flow layer was formed by spin coating the flow mold with a 20:1 RTV615A to RTV 615B mixture to form the thin membrane. Chip assembly consists of bonding the upper control layer to the lower flow layer, punching fluidic access holes and then bonding the assembly to the glass substrate, thereby enclosing the lower flow layer.

Figure 5.2.1 shows a schematic diagram of the prototype pressure driven chip designed for writing discrete intensity levels of three species of QDs. The red lines in the figure are representative of the channels on the control layer and the black lines represent those on the flow layer. A single storage cell is located at the bottom. Each individual delivery channel contains a writing control element consisting of a series of parallel channels (not shown to scale in the diagram) in series with the main channel. The control element serves as an effective stepwise variable flow resistor in that opening each channel reduces the flow resistance and therefore increases the volume flow rate in a stepwise manner.

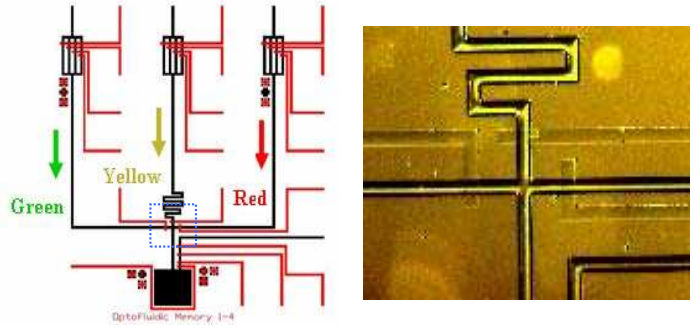

Figure 5.13: Schematic of pressure driven spectral code writer designed for use with 3 different quantum dot species. (b)Detail shows magnified view of both the flow and control layers at the intersection.

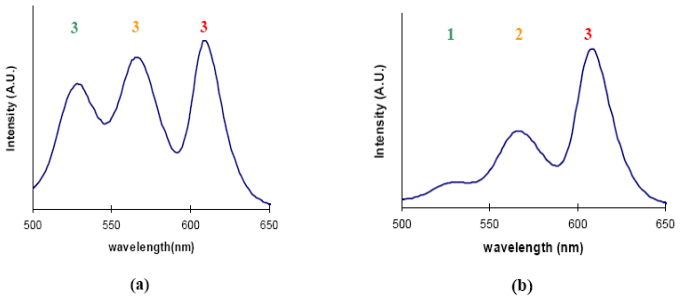

Figure 5.14: Recorded luminescence spectra from pressure driven QD cocktail mix and deliver circuit for (a) [G3,Y3,R3] and (b) [G1 Y2 R3]

Different codes were written to the storage chamber by setting the resistance of each of the three channels by closing a number of the gate valves. Since the intensity of each individual species is proportional to the volume flow rate into the storage unit the resistance element allows for the writing of discrete intensity levels. Figure 5.2.1 shows the spectral signature of several test codes written to the storage chamber. In general it was found that while the resistance control elements were successful at writing discrete codes, balancing the channels such that the same number of open elements resulted in the same volume flow rate was difficult. Each channel has a different inherent resistance, which means that although the code writer can easily create several discrete intensity levels for each color, corresponding levels do not have the same absolute intensity across the different colors. For a single storage element this does not cause a major problem, but inability to precisely control the absolute intensity of the quantum dot species at different locations would complicate the readout of a practical memory. For this reason, more accurate mixing a delivery circuits, which are less sensitive to variations in flow resistance, are desirable.

Although more precise pressure driven systems, such as those based on independent peristaltic pumps, can be devised, electrokinetics provides a more flexible solution. At a size scale above ten microns relatively high flow rates and excellent control can be obtained in microfluidic systems using the pressure driven technique described above. As the channel scale is downsized there is an inherent limitation in that the pressure required to maintain a constant flow velocity is inversely proportional to the channel width squared (for a low aspect ratio channel, for square channels the effect is more dramatic). As channels on the order of 100 nanometers or smaller will be required to increase memory density to that of existing data storage techniques, pressure driven flow may create a bottleneck the writing speed of the system. In contrast, electrokinetic fluid propulsion is caused by a body force applied at the liquid solid surface. The flow velocity is constant regardless of the channel size

as long as the channel is much larger than the ionic double layer length [24]. Additionally, since switching is controlled electrically, as opposed to mechanically, setting up and writing of codes can potentially be much quicker, in principal limited only by the viscous response of the fluid.

We fabricated continuous flow electrokinetic chip composed of three channels with widths of 50 microns each. The channels intersect to form a single output, also 50 microns wide. Each quantum dot solution was placed in one of the three reservoirs at the input end of the chip. The output reservoir of the fluidic system is grounded, and variable voltages were applied to each of the input reservoirs. The applied voltages were on the order of 1000 V DC to create enough current to drive fluid flow, given the large electrical resistance of the 3 cm long channels. Figure 5.2.1 is fluorescence image captured by The electrokinetic mechanism for cocktail mixing writes codes by adjusting the voltage at the inlet reservoir to predefined levels (i.e. lowering the voltage applied to the green reservoir relative to the red reduced its flow rate and thus its intensity level in the information packet). All of the spectra were measured at a distance downstream of the channel to ensure homogeneous mixing. Figure 5.2.1 shows two overlapping spectral codes written by the electrokinetic technique. The repeatability in intensity level demonstrated by this technique is superior to the previous pressure driven system.

5.2.2 Future Work

Controlled Nanometer scale patterning of semiconductor quantum dots has the potential to significantly improve both data storage and sub-wavelength imaging techniques. We have outlined several strategies that employ micro- and nanofluidic channels for precise delivery of a small number of luminescent particles. However, the drawbacks of these schemes lie in the relatively slow rate of particle handling and placement, and the inherent inaccuracy of trying to deliver a discrete number of col-

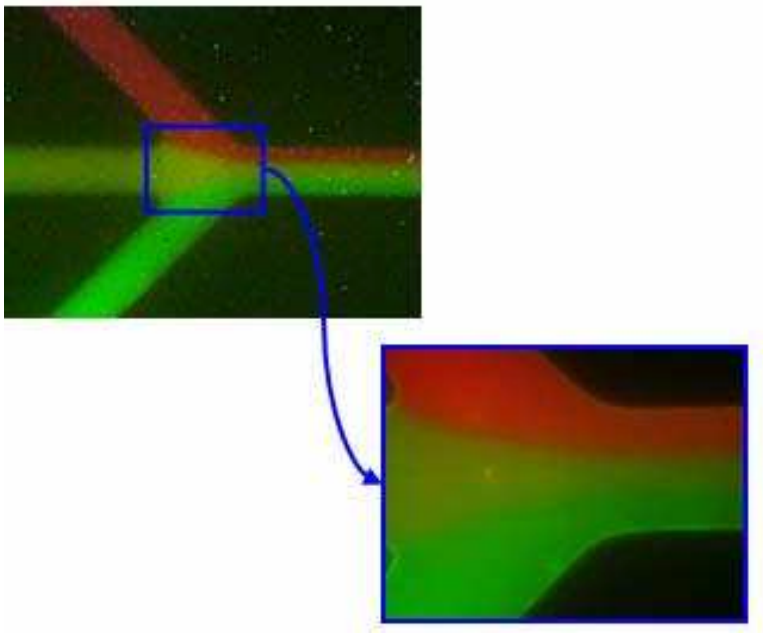

Figure 5.15: Fluorescence microscope image of electrokinetic mixing of 3 species QD cocktails, with 1000V applied to all inlets. Channel widths are 50 microns.

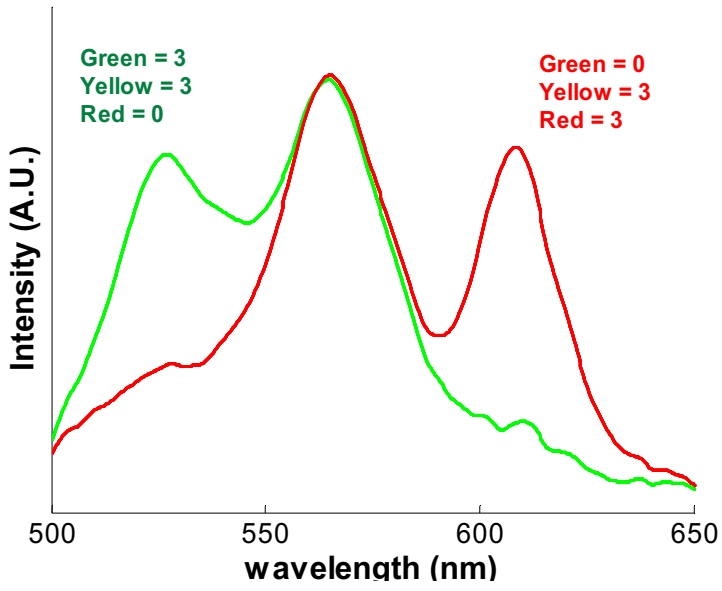

Figure 5.16: Recorded luminescence spectra from electrokinetic QD cocktail mix and deliver circuit

loids from a continous stream of a suspension. In order to realize the best performance with subwavelength placement of semiconductor quantum dots, more sophisticated methods for handling colloidal particles at the single particle level must be developed.

References

[1] D. Gammon, ES Snow, BV Shanabrook, DS Katzer, and D. Park. Homogeneous linewidths in the optical spectrum of a single gallium arsenide quantum dot. *Science*, 273(5271):87, 1996.

[2] LE Brus. Electron electron and electron-hole interactions in small semiconductor crystallites - the size dependence of the lowest excited electronic state. *Journal of Chemical Physics*, 80(9):4403–4409, 1984.

[3] M. Bruchez Jr, M. Moronne, P. Gin, S. Weiss, and A.P. Alivisatos. Semiconductor nanocrystals as fluorescent biological labels. *Science*, 281(5385):2013, 1998.

[4] Gilbert Strang. *Linear Algebra and its Applications*. Thomson Learning, Inc., 3rd edition, 1988.

[5] Xin Heng, David Erickson, L. Ryan Baugh, Zahid Yaqoob, Paul W. Sternberg, Demetri Psaltis, and Changhuei Yang. Optofluidic microscopy - a method for implementing a high resolution optical microscope on a chip. *Lab on a Chip*, 6(10):1274–1276, OCT 2006.

[6] H. A. Bethe. Theory of diffraction by small holes. *Phys. Rev.*, 66(7-8):163–182, Oct 1944.

[7] FJG de Abajo, JJ Saenz, I Campillo, and JS Dolado. Site and lattice resonances in metallic hole arrays. *Optics Express*, 14(1):7–18, JAN 9 2006.

[8] W. B. Russel, D. A. Saville, and W. R. Schowalter. *Colloidal Dispersions*. Cambridge Univeristy Press, Cambridge, 1989.

[9] CA Leatherdale, WK Woo, FV Mikulec, and MG Bawendi. On the absorption cross section of cdse nanocrystal quantum dots. *Journal Of Physical Chemistry B*, 106(31):7619–7622, AUG 8 2002.

[10] JN Farahani, DW Pohl, HJ Eisler, and B Hecht. Single quantum dot coupled to a scanning optical antenna: A tunable superemitter. *Physical Review Letters*, 95(1), JUL 1 2005.

[11] M. Gao, J. Sun, E. Dulkeith, N. Gaponik, U. Lemmer, and J. Feldmann. Lateral patterning of cdte nanocrystal films by the electric field directed layer-by-layer assembly method. *Langmuir*, 18(10):4098–4102, 2002.

[12] AR Clapp, IL Medintz, HT Uyeda, BR Fisher, ER Goldman, MG Bawendi, and H Mattoussi. Quantum dot-based multiplexed fluorescence resonance energy transfer. *Journal of the American Chemical Society*, 127(51):18212–18221, DEC 28 2005.

[13] SA Crooker, JA Hollingsworth, S Tretiak, and VI Klimov. Spectrally resolved dynamics of energy transfer in quantum-dot assemblies: Towards engineered energy flows in artificial materials. *Physical Review Letters*, 89(18), OCT 28 2002.

[14] Xiquan Cui, Xin Heng, Jigang Wu, Zahid Yaqoob, Axel Scherer, Demetri Psaltis, and Changhuei Yang. Slanted hole array beam profiler (sharp)- a high-resolution portable beam profiler based on a linear aperture array. *Optics Letters*, 31(21):3161–3163, NOV 1 2006.

[15] V. J. Cadarso, A. Llobera, G. Villanueva, C. Dominguez, and J. A. Plaza. 3-d modulable pdms-based microlens system. *Opt. Express*, 16(7):4918–4929, 2008.

[16] Y. Xia, E. Kim, X.M. Zhao, J.A. Rogers, M. Prentiss, and G.M. Whitesides. Complex Optical Surfaces Formed by Replica Molding Against Elastomeric Masters. *Science*, 273(5273):347, 1996.

[17] Madanagopal V. Kunnavakkam, F. M. Houlihan, M. Schlax, J. A. Liddle, P. Kolodner, O. Nalamasu, and J. A. Rogers. Low-cost, low-loss microlens arrays fabricated by soft-lithography replication process. *Applied Physics Letters*, 82(8):1152–1154, 2003.

[18] T Thorsen, SJ Maerkl, and SR Quake. Microfluidic large-scale integration. *Science*, 298(5593):580–584, OCT 18 2002.

[19] A Groisman, M Enzelberger, and SR Quake. Microfluidic memory and control devices. *Science*, 300(5621):955–958, MAY 9 2003.

[20] Blue Ray Disc Foundation. Blue ray disc format: General, August 2004. `http://www.blu-raydisc.com/Assets/Downloadablefile/general_bluraydiscformat-15263.pdf`.

[21] MY Han, XH Gao, JZ Su, and S Nie. Quantum-dot-tagged microbeads for multiplexed optical coding of biomolecules. *Nature Biotechnology*, 19(7):631–635, JUL 2001.

[22] S Chang, M Zhou, and CP Grover. Information coding and retrieving using fluorescent semiconductor nanocrystals for object identification. *Optics Express*, 12(1):143–148, JAN 12 2004.

[23] MA Unger, HP Chou, T Thorsen, A Scherer, and SR Quake. Monolithic microfabricated valves and pumps by multilayer soft lithography. *Science*, 288(5463):113–116, APR 7 2000.

[24] R. Karnik, R. Fan, M. Yue, D. Li, P. Yang, and A. Majumdar. Electrostatic control of ions and molecules in nanofluidic transistors. *Nano Lett*, 5(5):943–948, 2005.

Appendix A

Matlab routines

This appendix contains the matlab code used to produce Figure 2.4. The main script defines the inner and outer radii of the particle, and the optical properties of the core, shell, and surrounding medium. The wavelength dependent optical properties of the gold shell are taken from a published reference [1]. The top level script calls a subroutine to calculate the extinction efficiency. This subroutine and its suporting functions were adapted from the BHCOAT program presented in appendix B of Absorption and Scattering of Light by Small Particles [2].

```
%%%% Main Script %%%%%%%%%%%%%%%%%%%%%%%%%%%%%%%%%%%%%%%%%%%%%%%%%%%%%%%%%%%%
minE=0.66;  %minimum energy of radiation 0.66 eV
maxE=4.0;   %maximum energy of radiation 4.0 eV
step=0.01;  %calculate extinction for all energies between minE and max E
            %with resolution 0.01 eV
pi = 3.14159;
e=1.6*10^-19; %charge on the electron in Coulombs
c=3*10^8;     %speed of light m/s
hbar=1.054*10^-34; %Planck constant

%calculate the complex permittivity of gold across the energy range
[Energy,oep1,oep2]=bulkconstants('au',minE,maxE,step);

e1 =1.46;       %dielectric constant of core (Silica)
e2=oep1+i*oep2; %dielectric constant of shell (Gold)
e3=1;           %dielectric constant of medium (Vacuum)

w=Energy*e/hbar;  %w is radiation frequency at given energy
k=w/c;            %vacuum wavenumber for a given energy
n1=sqrt(e1);      % refractive index of core
```

```
n2=sqrt(e2);      % refractive index of shell
n=sqrt(e3);       % refractive index of medium
m1=n1/n;
m2=n2/n;

a=50e-9;          %core radius in meters
b=5e-9;           %shell thickness in  meters

x=a*k;            %dimensionless size parameter of core
y=(a+b)*k;        %dimensionless size parameter of shell

ext=qcoatext(m1,m2,x,y); %calculate extinction efficiency, following
                          %B&H appendix B
plot(ev2nm(Energy),ext); %plot extinction efficency vs. wavelength


%%%%Qcoat Efficiency functions %%%%%%%%%%%%%%%%%%%%%%%%%%%%%%%%%%%%%%%%%%%%

function [ret]=Qcoatext(m1,m2,x,y);
%Qcoatext computes the extinction efficiency of a coated sphere for a given
%m1, m2, x and y. m1 and m2 are the indices of refraction for the core
%and the coating divided by the index of refraction of the medium.  x and y
%are the size parameters of the core and the coating. []=Qcoatext(m1,m2,x,y).

%Acoatn and Bcoatn are both called.

nstop = floor(max(abs(max(m2) * max(y)), max(y) + 4 .* max(y).^(1/3)+2)) + 15
%As per Bohren & Huffman's program in Appendix A, I terminate the series
%after nstop terms, with nstop as above. The max functions are there so
%that nstop is a scalar and not a vector.

    for k = 1:nstop;
        A(k,:) = 2./ (y.^2) .* (2* k +1) .* ...
        (real(Acoatn(k,m1,m2,x,y)) + real(Bcoatn(k,m1,m2,x,y)));
    end;
%Above is just the formula for the kth term of the extinction efficiency.
%See Bohren & Huffman pg. 103.
%As it is now nstop terms are calculated and summed.

ret = sum(A);


function [ret]=Qcoatback(m1,m2,x,y);
%Qcoatback computes the backscattering efficiency of a coated sphere for a
%given m1, m2, x and y. m1 and m2 are the indices of refraction for the
%core and the coating divided by the index of refraction of the medium. x and y
%are the size parameters of the core and the coating. []=Qcoatback(m1,m2,x,y).
```

```
%Acoatn and Bcoatn are both called.

nstop = floor(max(abs(max(m2) * max(y)), max(y) + 4 .* max(y).^(1/3)+2)) + 15;
%As per Bohren & Huffman's program in Appendix A, I terminate the series
%after nstop terms, with nstop as above.  The max functions are there so
%that nstop is a scalar and not a vector.

    for k = 1:nstop;
        A(k,:) = (2* k +1) .* (-1)^k .* (Acoatn(k,m1,m2,x,y)
        ... - Bcoatn(k,m1,m2,x,y));
    end;
%Above is just the formula for the kth term in the sum for
%the backscatter efficiency. See Bohren &
%Huffman pg. 122.  As it is now nstop terms are calculated and summed.

ret = 1 ./ (y).^2 .* abs(sum(A)).^2;
%This is the formula for the backscatter efficiency.  It involves the sum
%of the terms calculated above.

function [ret]=Qcoatsca(m1,m2,x,y);
%Qcoatsca computes the scattering efficiency of a coated sphere for a given
%m1, m2, x and y. m1 and m2 are the indices of refraction for the core
%and the coating divided by the index of refraction of the medium.  x and y
%are the size parameters of the core and the coating. []=Qcoatext(m1,m2,x,y).

%Acoatn and Bcoatn are both called.

nstop = floor(max(abs(max(m2) * max(y)), max(y) + 4 .* max(y).^(1/3)+2)) + 15;
%As per Bohren & Huffman's program in Appendix A, I terminate the series
%after nstop terms, with nstop as above. The max functions are there so
%that nstop is a scalar and not a vector.

    for k = 1:nstop;
        A(k,:) = 2 ./ (y.^2) .* (2* k +1) .* ...
        (abs(Acoatn(k,m1,m2,x,y)).^2 + abs(Bcoatn(k,m1,m2,x,y)).^2);
    end;
%Above is just the formula for the kth term of the scattering efficiency.
%See Bohren & Huffman pg. 103.
%As it is now nstop terms are calculated and summed.

ret = sum(A);

%%%%%%%% Coefficient Functions %%%%%%%%%%%%%%%%%%%%%%%%%%

function [ret] = Acoatn(n,m1,m2,x,y);
%Acoatn gives the value of an seen on pg. 483 of Bohren & Huffman
```

```
%used in the calculation of the expansion coefficients for a
%given n, m1, m2, x, and y. []=Acoatn(n,m1,m2,x,y)

%Dtiln, Psi and Xi are all called.

ret = ((Dtiln(n,m1,m2,x,y) ./ m2 + n ./ y) .* Psi(n,y) - Psi(n - 1,y))...
    ./ ((Dtiln(n,m1,m2,x,y) ./ m2 + n ./ y) .* Xi(n,y) - Xi(n - 1,y));
%This is the formula seen on pg. 483 of Bohren & Huffman.


function [ret] = Bcoatn(n,m1,m2,x,y);
%Bcoatn gives the value of bn seen on pg. 483 of Bohren & Huffman
%used in the calculation of the expansion coefficients for a
%given n, m1, m2, x, and y. []=Bcoatn(n,m1,m2,x,y)

%Gtiln, Psi and Xi are all called.

ret = ((Gtiln(n,m1,m2,x,y) .* m2 + n ./ y) .* Psi(n,y) - Psi(n - 1,y))...
    ./ ((Gtiln(n,m1,m2,x,y) .* m2 + n ./ y) .* Xi(n,y) - Xi(n - 1,y));
%This is the formula seen on pg. 483 of Bohren & Huffman.

%%%%%%%%%%%%%%%%%%%% Dtlin and Gtlin %%%%%%%%%%%%%%%%%%%%%%%%%%%%%%%%%%

function [ret] = Dtiln(n,m1,m2,x,y);
%Dtiln gives the value of D~n seen on pg. 483 of Bohren & Huffman
%used in the calculation of the expansion coefficients for a
%given n, m1, m2, x, and y. []=Dtiln(n,m1,m2,x,y)

%Dpsi, Alphan, Psi and Chi are all called.

nstop = floor(max(abs(max(m2) * max(y)), max(y) + 4 .* max(y).^(1/3)+2)) + 15;
%Here I set the order for the start of the recurrence for the logarithmic
%derivative as done in the prgram in Appendix A of Bohren & Huffman. The
%max functions are there so that nstop is a scalar and not a vector.

m = m2 ./ m1;
    if nstop>n
        ret = (Dpsi(nstop,n,m2,y) + Alphan(n,m1,m2,x) .* (n * Chi(n,m2 .* y) ...
            ./ (m2 .* y) - Chi(n-1, m2 .* y)) ./ Psi (n, m2 .* y)) ./ ...
        (1 - Alphan(n,m1,m2,x) .* Chi(n,m2 .* y) ./ Psi(n,m2 .* y));
        %This is the formula seen on pg. 483 of Bohren & Huffman.

        else
            ret = 0;
            %For n above nstop Dpsi=0 and An=0 so Dtiln=0.

    end
```

```
function [ret] = Gtiln(n,m1,m2,x,y);
%Dtiln gives the value of G~n seen on pg. 483 of Bohren & Huffman
%used in the calculation of the expansion coefficients for a
%given n, m1, m2, x, and y. []=Gtiln(n,m1,m2,x,y)

%Dpsi, Betan, Psi and Chi are all called.

nstop = floor(max(abs(max(m2) * max(y)), max(y) + 4 .* max(y).^(1/3)+2)) + 15;
%Here I set the order for the start of the recurrence for the logarithmic
%derivative as done in the prgram in Appendix A of Bohren & Huffman. The
%max functions are there so that nstop is a scalar and not a vector.

m = m2 ./ m1;
    if nstop>n
        ret = (Dpsi(nstop,n,m2,y) + Betan(n,m1,m2,x) .* (n * Chi(n,m2 .* y) ...
            ./(m2 .* y) - Chi(n-1, m2 .* y)) ./ Psi (n, m2 .* y)) ./ ...
        (1 - Betan(n,m1,m2,x) .* Chi(n,m2 .* y) ./ Psi(n,m2 .* y));
        %This is the formula seen on pg. 483 of Bohren & Huffman.

        else
            ret = 0;
            %For n above nstop Dpsi=0 and Bn=0 so Gtiln=0.

    end

%%%%%%%%%%%%%Alphan and Betan %%%%%%%%%%%%%%%%%%%%%%%%%%%%%%%%%%%%%%%%%%%%%%%%%%%%%%
function [ret] = Alphan(n,m1,m2,x);
%Alphan gives the value of An seen on pg. 483 of Bohren & Huffman
%used in the calculation of the expansion coefficients for a
%given n, m1, m2, and x. []=Alphan(n,m1,m2,x)

%Dpsi, Psi and Chi are all called.

nstop = floor(max(abs(max(m1) * max(x)), max(x) + 4 .* max(x).^(1/3)+2)) + 15;
%Here I set the order for the start of the recurrence for the logarithmic
%derivative as done in the prgram in Appendix A of Bohren & Huffman. The
%max functions are there so that nstop is a scalar and not a vector.

m = m2 ./ m1;
    if nstop>n
        ret = Psi(n,m2 .* x) .* (m .* Dpsi(nstop,n,m1,x) - Dpsi(nstop,n,m2,x)) ...
            ./ (m .* Dpsi(nstop,n,m1,x) .* Chi(n,m2 .* x) + n * Chi(n, m2 .*x) ...
            ./ (m2 .* x) - Chi(n - 1, m2.* x));
        %This is the formula seen on pg. 483 of Bohren & Huffman.
```

```
        else
            ret = 0;
            %For n above nstop Dpsi is effectively 0 which makes An=0.

    end


function [ret] = Betan(n,m1,m2,x);
%Betan gives the value of Bn seen on pg. 483 of Bohren & Huffman
%used in the calculation of the expansion coefficients for a
%given n, m1, m2, and x. []=Betan(n,m1,m2,x)

%Dpsi, Psi and Chi are all called.

nstop = floor(max(abs(max(m1) * max(x)), max(x) + 4 .* max(x).^(1/3)+2)) + 15;
%Here I set the order for the start of the recurrence for the logarithmic
%derivative as done in the prgram in Appendix A of Bohren & Huffman. The
%max functions are there so that nstop is a scalar and not a vector.

m = m2 ./ m1;
    if nstop>n
        ret = Psi(n,m2 .* x) .* (m .* Dpsi(nstop,n,m2,x) - Dpsi(nstop,n,m1,x)) ...
            ./ (-Dpsi(nstop,n,m1,x) .* Chi(n,m2 .* x) - m .* n .* Chi(n, m2 .*x) ...
            ./ (m2 .* x) + m .* Chi(n - 1, m2 .* x));
        %This is the formula seen on pg. 483 of Bohren & Huffman.

        else
            ret = 0;
            %For n above nstop Dpsi is effectively 0 which makes Bn=0.

    end


%%%%%%%%%%%%% Psi, Chi,Xi, DPsi, %%%%%%%%%%%%%%%%%%%%%%%%%%%%%%%%%%%%%%%%%%%%%%%%%%%%%

function [ret] = Psi(n,x);
%Psi returns the Ricatti-Bessel of the first kind []=Psi(n,x)

%Only the built-in Matlab function besselj is called.

ret=(pi*x./2).^(1/2).*besselj(n+0.5,x);
%See http://mathworld.wolfram.com/Riccati-BesselFunctions.html for the
%above formula for the Riccati-Bessel function of the first kind.
%%%%%%%%%%%%%%%%%%%%%%%%%%%%%%%%%%%%%%%%%%%%%%%%%%%%%%%%%%%%%%%%%%%%%

function [ret] = Chi(n,x);
%Chi returns the Ricatti-Bessel of the second kind []=Chi(n,x)
```

```
%Only the built-in Matlab function bessely is called.

ret=-(pi*x./2).^(1/2).*bessely(n+0.5,x);
%See http://mathworld.wolfram.com/Riccati-BesselFunctions.html for the
%above formula for the Riccati-Bessel function of the second kind.
  %%%%%%%%%%%%%%%%%%%%%%%%%%%%%%%%%%%%%%%%%%%%%%%%%%%%%%%%%%%%%%%%%%%%%%%%%%%

function [ret] = Xi(n,x);
%Xi returns the Ricatti-Bessel of the second kind []=Xi(n,x)

%Only the built-in Matlab function bessely is called.

Chi=-(pi*x./2).^(1/2).*bessely(n+0.5,x);
%This calculates the Riccati-Bessel function of the second kind.
%See http://mathworld.wolfram.com/Riccati-BesselFunctions.html for the
%formula.

ret=Psi(n,x)-i*Chi;
%This is done to find the function used in calculated the expansion
%coefficients. See Bohren & Huffman pg. 478.

function [ret]=Dpsi(nstop,n,m,x);
%Dpsi returns the value of the logarithmic derivative of the Riccati-Bessel
%function of the first kind. nstop is the order where downward recurrence
%begins, n is the order desired, and m*x is the argument.
%[]=Dpsi(nstop,n,m,x)

%No other functions are called.

Dpsi_vector(nstop,:) = zeros(1,max(length(x),length(m))) ;
%This is the order of the logarithmic derivative where recurrence starts.
%I set it equal to a vector of 0's of the same length as the vector x so
%that dimension errors aren't encountered during the next step.

    for k = nstop:-1:n + 1;
        Dpsi_vector(k - 1,:) = k ./ (m .* x) ...
         - 1 ./ (Dpsi_vector(k,:) + k ./ (m .* x));
    end;
    % move down in order according to the recurrence relation given on
    %Bohren % Huffman pg. 127.

ret=Dpsi_vector(n,:);
%This gives the value of the nth order logarithmic derivative.
  %%%%%%%%%%%%%%%%%%%%%%%%%%%%%%%%%%%%%%%%%%%%%%%%%%%%%%%%%%%%%%%%%%%%%%%%%%%

%%%%%%%%%%%%%%%%%%%%%%%% bulkconstants %%%%%%%%%%%%%%%%%%%%%%%%
```

```
function [energy,ep1,ep2] = bulkconstants(material,minE,maxE,step)
    filename=lower(strcat(material,'constants.txt'));
    [dat_ev,dat_ep1,dat_ep2]=textread(filename,'%f %f %f','headerlines',2);
    Emax = max(dat_ev);
    Emin = min(dat_ev);

if (minE < Emin) || (maxE > Emax)  %check energy range
    sprintf('ERROR: Energy out of bounds')
    energy=0;                                    %return zero if failure
    ep1=0;
    ep2=0;
else
    energy=minE:step:maxE;
    ep1=spline(dat_ev,dat_ep1,energy); %interopolate data to match length of energy
    ep2=spline(dat_ev,dat_ep2,energy);
end

%%%%%%%%%%%%%%%%%%%%%%%%% Optical constants of Bulk Gold %%%%%%%%%%%%%%%%%%%%%%%%%
Landolt Bornstein Part III vol 15 B
eV    epsilon1  epsilon2
0.64    -189    25.4
0.77    -125    12.6
0.89    -90.4   8.19
1.020   -66.2   5.70
1.140   -51.0   3.86
1.260   -40.3   2.79
1.390   -32.0   1.92
1.510   -25.8   1.63
1.640   -20.6   1.27
1.760   -16.8   1.07
1.880   -13.6   1.03
2.010   -10.7   1.37
2.130   -8.11   1.66
2.260   -5.84   2.11
2.380   -3.95   2.58
2.500   -2.278  3.813
2.630   -1.703  4.844
2.750   -1.759  5.283
2.880   -1.692  5.649
3.000   -1.702  5.717
3.120   -1.649  5.739
3.250   -1.605  5.644
3.370   -1.401  5.609
3.500   -1.232  5.598
3.620   -1.310  5.538
3.740   -1.355  5.574
```

```
3.870   -1.231  5.846
3.990   -1.243  5.793
4.120   -1.227  5.780
4.240   -1.307  5.596
4.360   -1.332  5.495
4.490   -1.367  5.282
4.610   -1.346  4.976
4.740   -1.237  4.722
4.860   -1.080  4.490
4.980   -0.891  4.338
5.110   -0.745  4.163
5.230   -0.617  4.055
5.360   -0.551  3.892
5.480   -0.415  3.825
```

References

[1] K.H. Hellwege. *Landolt Börnstein: Numerical data and functional relationships in science and technology III.*, volume 15, pages 224–226. Springer-Verlag, Berlin, 1961.

[2] C. F. Bohren and D. R. Huffman. *Absorption and scatttering of light by small particles*, chapter Appendix B. Wiley, New York, 1983.